ESTIMATING VOLCANIC SULFUR DIOXIDE TO SULFATE AEROSOL CONVERSION RATES IN HAWAIʻI

A DISSERTATION SUBMITTED TO THE GRADUATE DIVISION OF THE UNIVERSITY OF HAWAIʻI AT MĀNOA IN PARTIAL FULFILLMENT OF THE REQUIREMENTS FOR THE DEGREE OF

DOCTOR OF PHILOSOPHY

IN

ATMOSPHERIC SCIENCES

MAY 2016

By

André Kristofer Pattantyús

Dissertation Committee:

Steven Businger, Chairperson
Duane Stevens
Michael Bell
Steven Howell
Lipyeow Lim

Keywords: Kīlauea Volcano, atmospheric chemistry, dispersion modeling, air quality, sulfur dioxide

ACKNOWLEDGEMENTS

I would like to thank my wife, Crystal, for support and encouragement while I completed my degree and my daughter, Synne, for making me smile at the beginning and end of each day. I would like to thank my parents, Christine and Gabor Pattantyus, my uncle, John Pattan, and my siblings, Monika Jansen and Nikolas Pattantyus, for their love and support through graduate school. I would like to send a big Mahalo nui loa to Duane Stevens for facilitating my transfer to University of Hawai'i at Mānoa. I would like to thank Steven Businger for providing an exciting and unique research opportunity and support. I would like to thank the remaining members of my committee past and present: Dr. Y. L. Chen, Dr. John Porter, Dr. Michael Bell, Dr. Steven Howell, and Dr. Lipyeow Lim who provided guidance, feedback, and generously donated their time over the past three years. I would like to thank Tiziana Cherubini, Ryan Lyman, Paulo Antonelli, Mike Gonzalves, and RCF staff for technical support. I would like to thank Tamar Elias and Jeff Sutton at Hawai'i Volcanoes Observatory, Keith Horton, Dr. David Brooks, Lisa Young at HDOH, Vanessa Almanza, and Brandon Bukunt for making the field experiment a success. I would like the thank Rhett Bulter and HIGP for funding the field campaign.

ABSTRACT

Volcanic smog, known as vog, has been a persistent issue on the island of Hawai‘i since the eruption of Kīlauea Volcano began in 1983. Vog, made up of sulfur dioxide (SO_2) and sulfate aerosols (collectively referred to as SO_4) poses a significant health risk to communities surrounding the volcano and on the leeward coast of Hawai‘i. The Vog Measurement and Prediction Project (VMAP) was launched by the University of Hawai‘i at Mānoa (UHM) and United States Geologic Survey in 2010 as a feasibility study to evaluate whether vog forecasts are achievable and usable. The UHM Vog Model has been operational since 2010 producing forecasts of SO_2 and SO_4 for the entire state of Hawai‘i. The UHM Vog Model's purpose is to warn the public, particularly sensitive groups including the elderly, children, and those with respiratory problems, to avoid high concentrations of vog.

More recently, the Hawai‘i Department of Health has expressed interest in using Vog Model forecasts to issue air quality alerts when projected concentrations exceed certain thresholds. An early evaluation of the model performance suggested that forecasts are poor for high-end concentrations of both SO_2 and SO_4, bringing the reliability of the model into question for issuing warnings. To address this shortcoming, a number of improvements to the model were considered. The most promising improvement was including a more comprehensive sulfur chemistry scheme to represent the conversion of SO_2 to SO_4.

A new sulfur chemistry scheme was constructed for inclusion into the UHM Vog Model. This scheme was based on theory and past research of sulfur chemistry. To provide a baseline for the new scheme a brief field experiment was conducted in

July 2015 to estimate the conversion rate of SO_2 to SO_4. The new sulfur chemistry scheme, along with other available schemes, were evaluated against observations of SO_2 and $PM_{2.5}$ around the island of Hawai‘i during November 2015. The results of this evaluation revealed the new sulfur chemistry scheme improved forecasts for SO_2 and SO_4. Also, as forecast windows extended from one hour to six hours the probability of detection for SO_2 increased from 10-30% to 50-70%.

TABLE OF CONTENTS

ACKNOWLEDGEMENTS i

ABSTRACT ii

LIST OF TABLES vii

LIST OF FIGURES viii

CHAPTER 1. INTRODUCTORY DISCUSSION 1

1.1 Introduction 1

1.2 Vog and Air Quality 4

1.3 Forecasting Vog 6

1.4 SO_2 to Sulfate Aerosol Conversion 8

1.4.1 Observations 9

1.4.2 Sulfur Dioxide Chemistry 11

1.5 Goals and Document Organization 13

CHAPTER 2. SULFUR DIOXIDE TO SULFATE AEROSOL CHEMISTRY 15

2.1 Introduction 15

2.2 Gas Phase 15

2.3 Aqueous Phase 21

2.4 Summary 29

CHAPTER 3. OBSERVATIONS 32

3.1 Introduction 32

3.2 Virtual Field Experiment 35

3.3 Field Experiment 42

3.3.1 Synoptic Conditions 43
3.3.2 Primary Instruments 45
3.3.2.1 FLYSPEC 45
3.3.2.2 GLOBE Sun Photometer 47
3.3.2.3 Ceilometers 49
3.3.3 Date Reduction Methodology 51
3.3.3.1 SO_2 Flux 51
3.3.3.2 SO_4 Flux 53
3.3.3.3 Plume Speed 54
3.3.4 Results 58
3.3.4.1 Method One 62
3.3.4.2 Method Two 63
3.3.4.3 Method Three 64
3.4 Conclusions 68
CHAPTER 4. A NEW SULFUR CHEMISTRY SCHEME FOR THE UNIVERISITY OF HAWAIʻI VOG MODEL 72
4.1 Introduction 72
4.2 Model Chemistry Background 74
4.3 Constructing a New Sulfur Dioxide Chemistry Scheme 75
4.4 Results 79
4.4.1 Comparison with Field Measurements 79
4.4.2 Qualitative Evaluation 83
4.4.3 Quantitative Evaluation 90

4.5 Summary 99

CHAPTER 5. CONCLUSIONS 102

5.1 New Chemistry Scheme 103

5.2 Future Work 106

5.2.1 Plume-rise Initialization 106

5.2.2 Data Assimilation 107

5.2.3 Extend Evaluation 108

5.3 Ensemble Model 108

5.4 Further Study of Sulfur Chemistry 110

APPENDIX 113

REFERENCES 129

LIST OF TABLES

Table 1: Technical specifications of ceilometers used during field experiment. 51

Table 2: SO_2 to SO_4 environmental conversion rates at Kīlauea Volcano estimated from measurements collected during 2015 field experiment. 71

Table 3: Mean OH concentrations (10^3 molecules cm^{-3}) derived from INTEX-B and PEM Tropics B measurements for each hour (HST). OH final, represents the values used in the new sulfur chemistry module. Hours with no data are filled with a dash. 77

Table 4: SO_2 (ppm) and particulate matter ($\mu g/m^3$) concentrations used to define the VMAP color codes. The SO_2 designations are consistent with those used by the Hawai'i State Department of Health for their short-term (1-hr) SO_2 index. Environmental Protection Agency (EPA) uses $PM_{2.5}$ concentration thresholds for their 24-hour AQI designations. AQI level 1 = Good, 2 = Moderate, 3 = Unhealthy for sensitive groups, 4 = Unhealthy, 5 = Very unhealthy, and 6 = Hazardous. 91

Table 5: The 2 x 2 contingency table. 91

LIST OF FIGURES

Figure 1: Map showing the Island of Hawai'i with the relative locations of the volcanic vents, Volcano village, the cities of Hilo and Kailua-Kona, and Hawai'i Department of Health SO_2, SO_4 observation sites. 2

Figure 2: Days per year when EPA 1-hr SO_2 concentration exceeded the National Ambient Air Quality Standard of 75 ppb. HOVE stands for Hawaiian Ocean View Estates and HAVO OB stands for Hawai'i Volcanoes Observatory. 5

Figure 3: Total number of observations for (a) SO_2 concentrations exceeding 0.1 ppm (grey) and number of forecasts that matched observations (black), and for (b) sulfate aerosols exceeding 15 μg m^{-3}. Note that there were zero SO_2 observations for Kailua-Kona at AQI levels ≥2. Visitor's center refers to the Hawai'I Volcanoes National Park Visitor's Center. Figure adapted from Businger et al. [2015]. 8

Figure 4: Concentrations of OH (blue dots) measured during flight 6 (a) and 7 (b) during the PEM-Tropics B study. Also shown for reference is an altitude profile (m) for each flight in red. Data are presented as one-minute average [OH]. Adapted from Mauldin et al. [2001]. 18

Figure 5: Variations for reaction rate constants for the oxidation of aqueous S(IV) by various oxidants as a function of the solution pH. Adapted from Eatough et al. [1994]. 22

Figure 6: Representation of Virtual Field Experiment at 18 UTC 3 February 2015. The plume is represented by the 1-hr mean SO_2 concentration in the 100-400 m layer AGL. Green areas represent concentrations greater than 0.1 ppm and yellow regions represent concentrations greater than 1.0 ppm. The 0.1 ppm threshold is assumed to be the minimum detectable signal by the FLYSPEC. Blue lines indicate locations where model data was used to simulate instrument measurements of the plume done by scans or traverses. 38

Figure 7: Map of study area. The typical plume trajectory from Halema'uma'u Crater is shown as the grey area parallel to Mamalahoa Highway (Highway 11). Measurements were collected at the proximal site which was collocated with FLYSPEC-0 of the stationary FLYSPEC array operated by HVO. The distant site was collocated in Pahala at the Hawai'i DOH air quality monitoring site on 9-10 July. The distant site was located along Hwy 11 on 14 July. 45

Figure 8: FLYSPEC-V3 layout and components. Used with permission from Keith Horton and FLYSPEC, Inc. 46

Figure 9: GLOBE sun photometer. A toggle switch on the right-hand side allows the user to switch between the red and green channels as well as the internal temperature sensor. 49

Figure 10: Vaisala CT25K (a) and CL31 (b). 50

Figure 11: a) Schematic diagram of FLYSPEC instrument configuration with 160-W solar panel. FLYSPEC sensor, electronics, and computer are in the black box under the aluminum housing that supports the solar panel. Grey box contains the deep cycle battery and charge controller. b) Aerial view of approximate FLYSPEC locations for the SO_2 monitoring array. F_0 represents FLYSPEC-0, F_1 - FLYSPEC-1, and so on. Sensor array is located approximately 2.7 km from source vent at Halemaʻumaʻu. 52

Figure 12: Wind data from the Sand Hill station just upwind from FLYSPEC-0 and plume speed and direction data calculated from the multiple-spectrometer method valid during obaservational periods on (a, b) 9 July 2015, (c, d) 10 July 2015, and (e, f) 14 July 2015. 55

Figure 13: High-resolution WRF wind vectors valid 0900 HST 9 July 2015. Wind vectors are mean boundary layer vectors defined as winds from 0 to 2000 m. The triangle represents Halema'uma'u Vent, the diamond next to it represents the proximal measurement site and the diamonds further downstream represent the distant measurement sites. On 9 and 10 July the distant site was at Pahala and on 14 July the distant site was along Highway 11, at a point between the proximal site and Pahala. The black trajectory based on visual observations, local wind observations, and model trajectories represents the plume path on 9 and 10 July. The red trajectory represents the plume path on 14 July. The reference vector is in m s^{-1}. Terrain contours (m) are shaded. 57

Figure 14: Timeseries of SO_2 and SO_4 fluxes calculated at the proximal site valid (a) 9 July, (c) 10 July, and (e) 14 July 2015. Fluxes calculated at the distant site are valid (b) 9 July, (d) 10 July, and (f) 14 July 2015. The distant site was located in Pahala on 9 and 10 July and along Hwy 11 on 14 July. 60

Figure 15: Fraction of sulfur observed as sulfate, f_s, derived from 10-minute averaged flux values. 61

Figure 16: 1-minute averaged SO_2 and SO_4 fluxes (kg s^{-1}) calculated at site 1 on 9 July 2015. 66

Figure 17: Sulfate fraction (f_s) calculated from SO_2 and SO_4 (c.f. Figure 10) at site 1 on 9 July 2015. 67

Figure 18: SO_2 to $S0_4$ conversion rates (% h^{-1}) estimated from observations on 9 July 2015. 68

Figure 19: 1-Minute averaged OH concentrations (molecules cm^{-3}) from INTEX-B (2006) and PEM Tropics B (1999) taken across the Pacific Ocean from the surface to 12 km altitude (a), from the surface to 3.0 km altitude (b), and the mean OH concentrations by hour (Local Time) for all observations (c). Data are plotted using a logarithmic scale on the y-axis. The black line represents the values used for the new sulfur module, which are similar to the mean values below 3.0 km but with some smoothing and interpolating of gaps in the data. 78

Figure 20: Comparison of estimated sulfate aerosol flux based on observations with a flux derived from sulfur dioxide fluxes at the same site and the new sulfur chemistry methodology. When SO_2 emissions increase around 1030 HST the numeric scheme estimates a much higher sulfate flux than what is estimated from observations. 81

Figure 21: Calculated OH concentrations for 9 July 2015 compared to mean OH concentrations prescribed for the model sulfur scheme. Red line represents hourly averaged OH concentrations calculated from flux data. 82

Figure 22: Estimated loss/production rate (s^{-1}) of OH calculated from INTEX-B CO, CH4, and OH data. 83

Figure 23: Comparison of model forecasts using the operational model chemistry (blue), the old chemistry routine in the model code (orange), and the new chemistry routine (green) with observations (black) of SO_2 (ppm) or $PM_{2.5}$ (μg m^{-3}) at site 1 (a and d), Pahala (b and e), and Ocean View (c and f) valid 1200 UTC 9 July 2015 to 0600 UTC 11 July 2015. Note site 1 has no $PM_{2.5}$ observations (d). 87

Figure 24: Comparison of model forecasts using the operational model chemistry (blue), the old chemistry routine in the model code (orange), and the new chemistry routine (green) with observations (black) of SO_2 (ppm) or $PM_{2.5}$ (μg m^{-3}) at site 1 (a and d), Pahala (b and e), and Ocean View (c and f) valid 1200 UTC 10 July 2015 to 0600 UTC 11 July 2015. Note site 1 has no $PM_{2.5}$ observations (d). 88

Figure 25: Comparison of model forecasts using the operational model chemistry (blue), the old chemistry routine in the model code (orange), and the new chemistry routine (green) with observations (black) of SO_2 (ppm) or $PM_{2.5}$ (μg m^{-3}) at site 1 (a and d), Pahala (b and e), and Ocean View (c and f) valid 1200 UTC 14 July 2015 to 0600 UTC 15 July 2015. Note site 1 has no $PM_{2.5}$ observations (d). 89

Figure 26: Estimated SO_2 emissions from Kīlauea volcano vents. Estimates are in metric tons per day (t d^{-1}). The shaded area represents the region that encompasses approximately 70% of estimated emissions each day. 93

Figure 27: SO_2 emissions (kg h^{-1}) used for model input. Each point represents the values used every hour for both model cycles (00 and 12 UTC) initialized that day. 94

Figure 28: Model skill at all sites evaluated for forecasted concentrations of SO_2 and SO_4 that exceed AQI level 2 over 1-hr forecast windows using Perfect Prognosis Forecasts (PPF) for (a) SO_2 and (b) SO_4, Probability of Detection (POD) for (c) SO_2 and (d) SO_4, and False Alarm Ratio (FAR) for (e) SO_2 and (f) SO_4. 96

Figure 29: Similar to Figure 25 but for 3-hr forecast window. 97

Figure 30: Similar to Figure 25 but for 6-hr forecast window. 97

Figure 31: SO_2 concentrations (ppm) during kona wind event from 20 November 2015 to 26 November 2015 observed at (a) HVO and (b) VC. Red line represents AQI level 2 threshold = 0.1 ppm. 99

Figure 32: Scatterplot of observed wind speed (m s-1) at Hawai‘i Volcano Observatory vs estimated plume height (m AGL) at Halema‘uma‘u Crater. Plume height estimates are done through visual observations using a clinometer. 107

CHAPTER 1. INTRODUCTORY DISCUSSION

1.1 Introduction

Kīlauea volcano has been continuously erupting from the Puʻu ʻŌʻo vent, or East Rift vent, since 1983, emitting large amounts of sulfur dioxide (SO_2). The rate of SO_2 emissions has ranged from less than 50 tons per day (t d^{-1}) to more than 10,000 t d^{-1} [Elias and Sutton, 2007]. In 2008, a second vent opened up in the Halemaʻumaʻu Crater, or summit vent, with a typical emission rate of ~1000 to 3000 t d^{-1} based on in-situ observations [Elias and Sutton, 2012]. This leads to annual SO_2 emissions between 0.3 and 1.1 million tons. In comparison, the 50 dirtiest power plants in the United States emit between 0.04 and 0.2 millions tons of SO_2 annually [Environmental Integrity Project, 2007].

Given the persistent northeast trade winds in tropical North Pacific, emissions from Kīlauea cause frequent episodes of poor air quality in the form of volcanic smog, or vog, for downwind and leeward communities on the island of Hawaiʻi (Figure 1). Vog is composed of sulfur dioxide gas, the primary pollutant emitted by the volcano, and sulfate aerosols, a secondary pollutant that forms from oxidation of sulfur dioxide. Between 2007 and 2010, it is estimated that Kīlauea volcano was responsible for 6% of global sulfate load [Elias and Sutton, 2012]. Due to their size, sulfate aerosols are considered a dominant component of fine particulate matter smaller than 2.5 micrometers ($PM_{2.5}$) and can impact human health and reduce visibility. Communities in close proximity to the volcano, such as the village of Volcano, are especially susceptible to episodes of poor air quality from

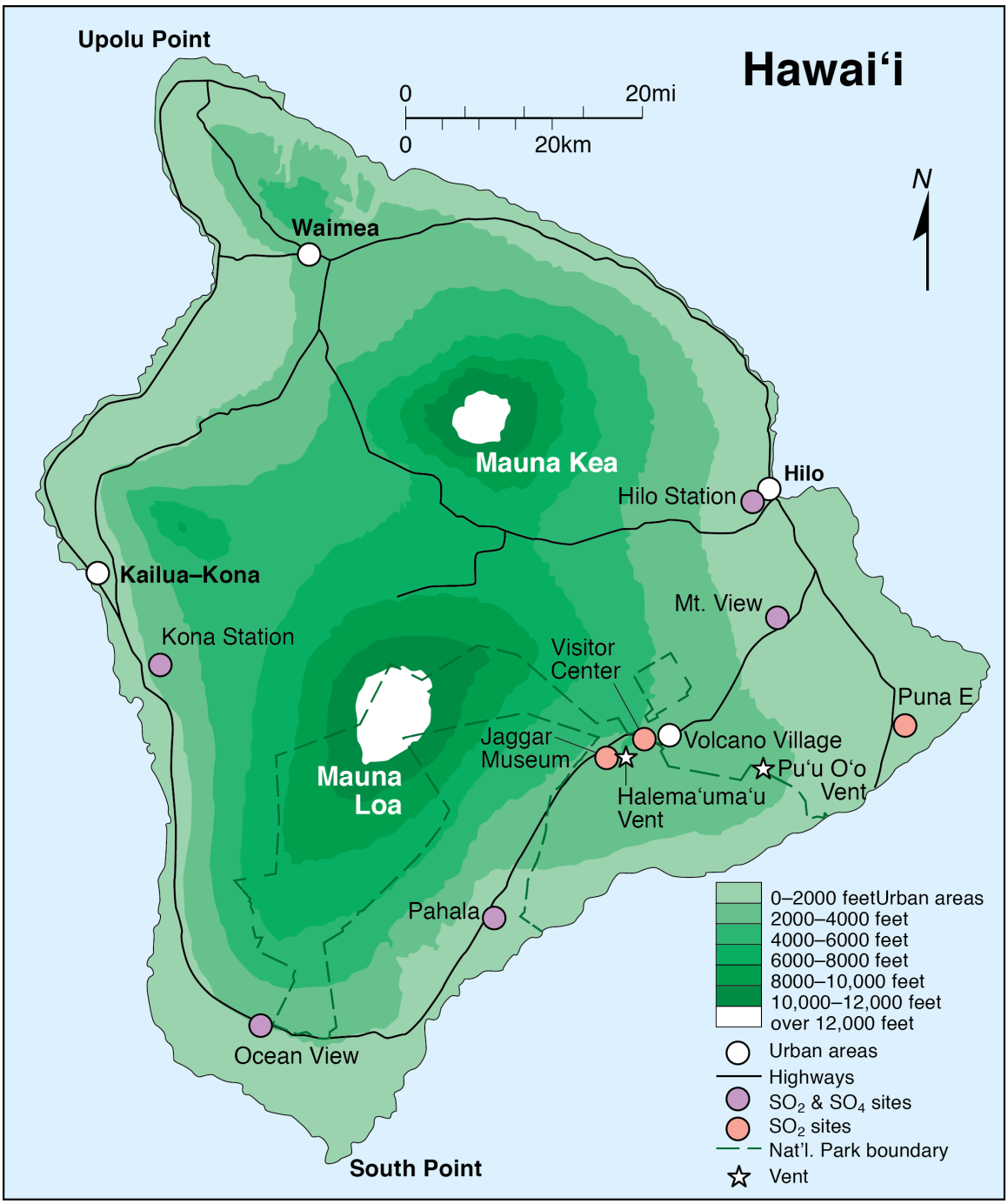

Figure 1: Map showing the Island of Hawai‘i with the relative locations of the volcanic vents, Volcano village, the cities of Hilo and Kailua-Kona, and Hawai‘i Department of Health SO_2, SO_4 observation sites.

SO_2 pollution, which have reached levels high enough that evacuations have been ordered.

While the lifetime of sulfur dioxide in the atmosphere is generally found to be on the order of a few days (~1-3), the lifetime of sulfates can be much longer. The lifetime of SO_2 is limited by ubiquitous photochemical sinks whereas the lifetime of sulfate is a result of a relatively slow rate of dry deposition and the erratic nature of wet deposition. Due to longer residence times, sulfate impacts can become pervasive. Hand et al. [2012] find that long range transport of sulfates from Asia impact air quality in the Pacific Northwest. It has also been demonstrated that Hawai‘i is affected by Asian dust from March to May that includes enhanced sulfate [Shaw, 1980; Perry et al., 1999; Holben et al. 2001].

High concentrations of sulfates reduce visibility, which can negatively impact aviation interests. If recent inflating of Mauna Loa leads to an eruption of SO_2, air traffic to and from Hawai‘i could experience significant interruptions from resulting sulfate formation. This sulfate can impact air quality as far away as the Phillipines if transported in the lower troposphere, or the Pacific Northwest if tranported in the upper troposphere.

Additionally, when sulfate is removed through wet deposition the result is acid rain. This is well documented by research in California and the northeast United States in the 1970’s and 1980’s [Eatough et al. 1994; and references within]. Sulfate contributes to acidification through wet deposition in the Ka‘ū region downwind of Kīlauea and has resulted in the area receiving low-interest USDA Farm Service Agency emergency loans to cover losses caused by vog.

Sulfates have been identified as important cloud condensation nuclei (CCN) [Cantrell et al., 2000] that can impact cloud microphysics and the hydrologic cycle [Pattantyus and Businger, 2014; Yuan et al., 2011a;b]. Sulfates influence the global radiation budget by reflecting incoming short-wave radiation [Charleson et al., 1992; Kiehl and Briegleb, 1993] and by indirect effects on cloud albedo and lifetimes [Twomey 1977; Jones et al., 2001; Yuan et al., 2011a]. Thus, sulfates can affect both day-to-day weather and global climate through cloud interactions. This broad range of impacts adds significance to determining the production rate of sulfate.

1.2 Vog and Air Quality

It is clear from Hawai'i Department of Health (hereafter referred to as HDOH) air quality monitoring data that vog impacts air quality on a daily basis. SO_2 pollution is observed most frequently adjacent to the volcano (Figure 2). SO_2 pollution is defined as any 1-hr period that exceeds the Environmental Protection Agency (EPA) National Ambient Air Quality Standards (NAAQS) 75 parts per billion (ppb) concentration breakpoint. As one moves further downwind the frequency of SO_2 pollution decreases while $PM_{2.5}$ pollution increases. Pāhala, the nearest community downwind of the volcano during typical trade wind conditions, has exceeded the old EPA SO_2 annual concentration limit of 30 ppb from 2008-2012. $PM_{2.5}$ pollution is defined as any 1-hr period that exceeds the EPA 24-hr $PM_{2.5}$ concentration breakpoint at 12 micrograms per meter cubed ($\mu g\ m^{-3}$). Communities on the leeward coast further downwind from the volcano, such as Kailua-Kona, experience frequent episodes of poor air quality in the form of $PM_{2.5}$ pollution. In Kona, HDOH [2013] has attributed nonattainment for annual average $PM_{2.5}$ NAAQS

($PM_{2.5}$ > 15 µg m^{-3}) in 2011 and 2012 to SO_2 emissions from Kīlauea. EPA data suggests that Kona reached nonattainment in 2013 as well. From 2011 to 2015, data shows that Kona has continuously exceeded the annual average $PM_{2.5}$ concentration set by the World Health Organization (WHO) ($PM_{2.5}$ > 10 µg m^{-3}). Longo [2013] also found the magnitude of health effects had increased in vog-exposed communities since the opening of the summit vent in 2008.

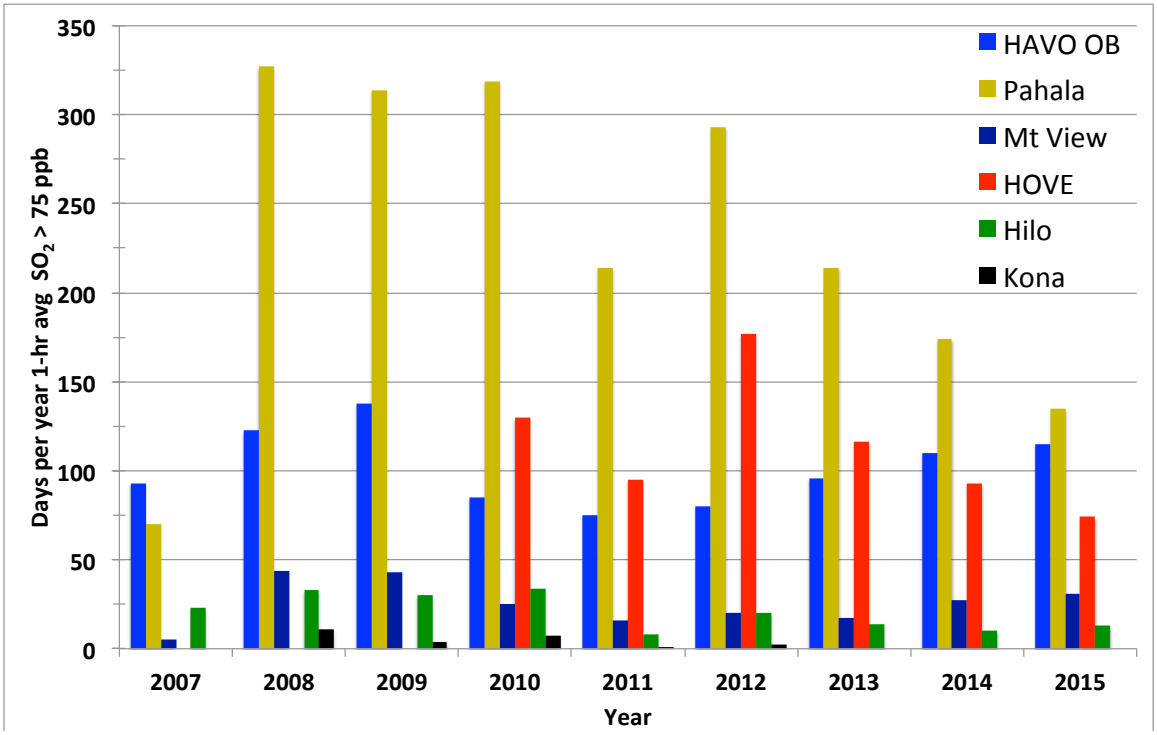

Figure 2: Days per year when EPA 1-hr SO_2 concentration exceeded the National Ambient Air Quality Standard of 75 ppb. HOVE stands for Hawaiian Ocean View Estates and HAVO OB stands for Hawai'i Volcanoes Observatory.

Based on this data, it is apparent that the conversion of sulfur dioxide to sulfate aerosols (hereafter referred to as SO_4) is important for predicting air quality downwind of the volcano and attribution of health symptoms to a particular pollutant species. The rate of SO_2 to sulfate aerosol conversion varies in time and

space but bulk estimates have been made from satellite data [Beirle et al., 2013]. Theoretical conversion rates and past research suggest that dominant conversion processes vary by an order of magnitude. Bulk conversion rates do not adequately resolve the differences in conversion processes but offer a good climatological approximation on monthly timescales. Consequently, bulk conversion rates provide inadequate forecasts for both SO_2 and sulfate aerosol concentrations around the island of Hawai‘i. Forecasts of these pollutants are a major concern for persons over 40, those suffering from asthma or other respiratory problems, and for the HDOH, who use forecasts for regulatory purposes.

1.3 Forecasting Vog

The Vog Measurement and Prediction Project (VMAP), established in 2010, provides daily forecasts of near ground SO_2 and SO_4 concentrations in order to mitigate the impacts of exposure to poor air quality resulting from the ongoing eruption of Kīlauea. Forecasts are produced from the University of Hawai‘i Vog Model (Vog model, hereafter) - a custom application of the Hybrid Single-Particle Lagrangian Integrated Trajectory (HYSPLIT) model [Draxler and Hess 1997, 1998]. Meteorological fields from the Weather Research and Forecast (WRF) model provide input to the Vog model, with a statewide grid spacing of 3 km and a 1-km grid covering Hawai‘i Island. SO_2 emissions from the volcano are estimated by HVO from measurements taken during vehicles traverses under the plume with a FLYSPEC correlation spectrometer and from an array of FLYSPECs aligned downwind of trade wind flow at the summit vent of Halema‘uma‘u [Horton et al., 2006]. The SO_2 sources in the model are represented as vertical line sources

representative of plumes during NE trade wind conditions. At Halemaʻumaʻu vent, 10% of emissions are released from heights between 50 m and 650 m above ground level (AGL) and the remaining 90% are released at 700 m AGL. At Puʻu ʻŌʻo, 10% of emissions are released between 50 and 270 m AGL and the remaining 90% is released at 300 AGL. A constant conversion rate of SO_2 to SO_4 is specified, originally at 10% per hour.

An early validation study of the VMAP forecasts finds that the Vog Model has difficulty forecasting high-end concentrations most hazardous to public health [Businger et al., 2015]. Specifically, correct SO_2 forecasts are a challenge given the rapid conversion rate specified in the model (10% h^{-1}) meaning most instances when SO_2 concentrations exceed 0.1 parts per million (ppm) go unforecasted at all sites downwind of Kīlauea (Figure 3). Only SO_4 forecasts at Kona capture a majority of the observed $PM_{2.5}$ pollution events ($PM_{2.5}$ > 15 μg m^{-3}).

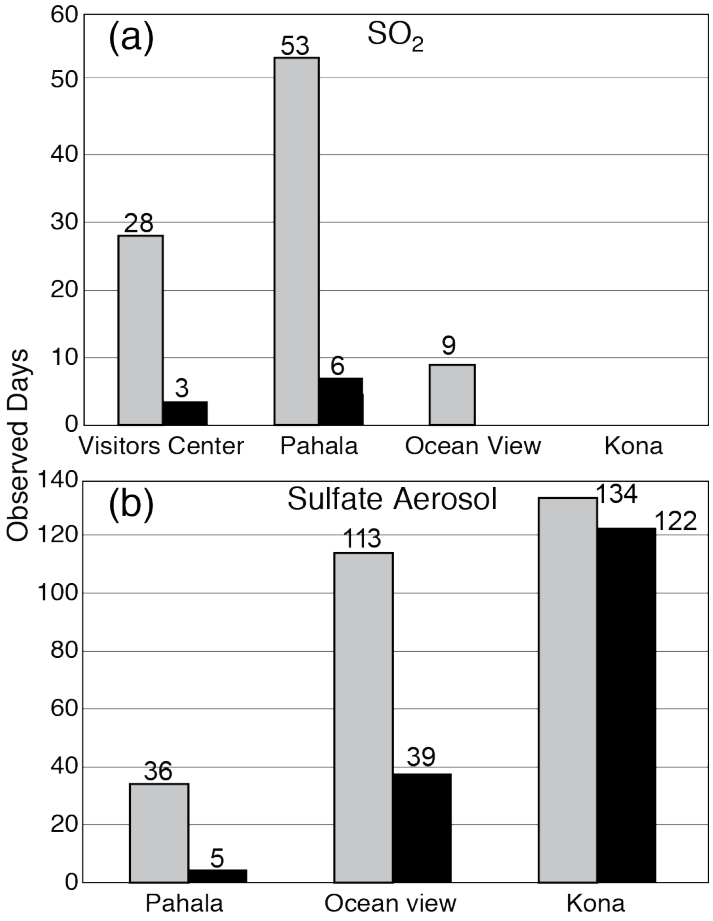

Figure 3: Total number of observations for (a) SO_2 concentrations exceeding 0.1 ppm (grey) and number of forecasts that matched observations (black), and for (b) sulfate aerosols exceeding 15 µg m^{-3}. Note that there were zero SO_2 observations for Kailua-Kona at AQI levels ≥2. Visitor's center refers to the Hawai'i Volcanoes National Park Visitor's Center. Figure adapted from Businger et al. [2015].

1.4 SO_2 to Sulfate Aerosol Conversion

Given the variety of impacts from sulfate aerosols it is of great interest to determine the rate of sulfate formation from sulfur dioxide emitted either naturally or by industry. There are a number of active volcanoes worldwide that degass sulfur dioxide (http://so2.gsfc.nasa.gov/), leading to sulfates that regularly impact the air quality of communities including Iceland, Nicaragua, Italy, and the Caribbean. Coal-burning power plants and industrial smelters also produce large amounts of

sulfur dioxide and sulfates. The rapid expansion of coal power plants in China has led to hazardous air quality impacting local communities, neighboring countries, and locations far downwind [e.g., Hand et al. 2012].

1.4.1 Observations

Many attempts have been made to measure sulfur dioxide loss rates from volcanic emissions, including some in the lower troposphere or planetary boundary layer [McGonigle et al., 2004; Rodriguez et al., 2005; Oppenheimer et al., 1998; Porter et al. 2002]. Generally, little care is taken during these experiments to attribute SO_2 loss to a particular process because the goal is only to determine if SO_2 flux measurements from correlation spectrometers are reliable proxies for source emissions of ash free tropospheric plumes [McGonigle et al., 2004]. The loss rate of SO_2 is important for evaluating the uncertainty of volcanic emissions. If a signifcant portion of SO_2 is lost between emission and measurement then fluxes would not be representative of the real emission rate. Loss rates (s^{-1}), k, are calculated using an exponential decay equation

$$\Phi = \Phi_0 e^{-kt} \tag{1.1}$$

where Φ and Φ_0 represent SO_2 fluxes estimated from transects with correlation spectometers taken at various distances downwind separated by some time, t. McGonigle et al. [2004] have found loss rates of $1\pm2 \times 10^{-5}$ s^{-1} at Mayasa volcano, Nicaragua. Comparatively, Rodriguez et al. [2005] have estimated loss rates of 1.51×10^{-5} to 8.22×10^{-4} s^{-1} at Soufriere Hills volcano, Monserrat, British Virgin Islands. Oppenheimer et al. [1998] have found rates an order of magnitude greater, 1.4 to 5.4×10^{-3} s^{-1}, at Soufriere Hills volcano, but noted that the plume was entrained into

orographic clouds. There is a large difference in the conversion rates that can be explained by the various oxidation pathways responsible for the conversion. The implicit assumption is that most lost SO_2 is converted to sulfate aerosols. Oppenheimer et al. [1998] caution that their observations of rapid loss of volcanic SO_2 in-cloud could lead to a global underestimation of volcanic SO_2 and subsequently underestimate troposperic sulfate and its impacts on climate.

Estimates of sulfate production from Kīlauea calculated using ground-based remote sensing methods imply a rate between 7-18% an hour [Porter et al., 2002]. This assumes no primary sulfate being emitted which may be incorrect based on near-vent measurements by Mather et al. [2012] who found appoximately 1% sulfate relative to SO_2 emissions during the early eruptive period of Halemaʻumaʻu in 2008. This observation suggests a coemitted catalyst (e.g., Fe^{2+}) may cause significant sulfate formation as SO_2 exits the vent, inflating conversion rates estimated further downwind. Such reactions have been implied previously [Eatough et al. 1984].

The height of Halemaʻumaʻu vent (1029 m) often brings the emission plume into contact with orographically induced clouds at or just above the surface increasing the liklihood of aqueous-phase reactions becoming important as the emissions are transported around the flanks of Mauna Loa. Cloud processing of sulfur dioxide to sulfate aerosols is important for determining the shape of sub-micron aerosol size distibutions, increasing the mass of sub-micron particles in the atmosphere, and moves particles into a size range to make them optically active [Caffrey et al. 2001]. Since 90% of clouds that form do not precipitate this produces

a high amount of aerosol mass in the troposphere [Caffrey et al. 2001]. This cloud cycling may be responsible for pollutant concentrations measured at stations downwind [See Appendix].

Conversion rates and processes observed in other locales may not apply at Kīlauea given it's unique features. The isolation of Kīlauea from major pollution sources within the tropical marine boundary layer results in a unique set of environmental conditions not previously documented. Ozone (O_3) and nitrogen oxides (NO_x) are found at much lower concentrations in the remote marine boundary layer than the oft-studied power plant plumes. HDOH [2013] have estimated all anthropogenic sources of SO_2 on Hawai'i island amount to less than 0.5% of the annual SO_2 emissions from Kīlauea. The high SO_2 emission rate at Kīlauea is at least an order of magnitude greater than those observed elsewhere [McGonigle et al., 2004; Nadau, 2006; Oppenheimer et al., 1998]. This abundence of SO_2 at Kīlauea could deplete typical reactants rapidly, limiting conversion rates and increasing the likelihood that additional trace gases and/or metals either emitted or in the ambient environment could become important reactants themselves.

1.4.2 Sulfur Dioxide Chemistry

Atmospheric sulfur chemistry and major processes responsible for sulfate formation are well documented. Homogeneous, gas phase oxidation of sulfur dioxide to sulfate aerosol proceeds via reaction with the hydroxyl radical, OH. Oxidation rates have been reported between 0-6% h^{-1} from power plants [Newman, 1981; Eatough et al., 1981; Forrest et al., 1981; Huang et al., 1982] and smelter plumes [Newman, 1981; Eatough et al., 1982]. Relatively slow reaction rates found

by McGonigle et al. [2004] and Rodriguez et al. [2005] suggest that gas phase oxidation via the OH radical is the dominant conversion mechanism.

In the aqueous phase, reactions may involve hydrogen peroxide, H_2O_2, ozone (O_3), or metal catalysts such as Fe(III) or Mn. Many of these reaction rates are highly dependent on droplet pH, except for H_2O_2. Hydrogen peroxide is considered the dominant reactant at low pH. Ozone reactions are highly pH dependent and only become the leading oxidant at pH > 5.5 [Hegg, 1989; Seinfeld and Pandis, 1998]. Oxidation rates in fog or clouds with ozone and/or hydrogen peroxide are expected to be on the order of 20-100% h^{-1} [Finlayson-Pitts 1986] and rapid reaction rates have been observed [Eatough et al. 1984]. Reactions with metal catalysts are more rare, but are suspected of producing high conversion rates (30 +/- 4% h^{-1}) in power plant plumes entrained into fog or clouds [Eatough et al., 1984].

Simpson [2010] took three approaches to estimate in-cloud oxidation of SO_2 to sulfate aerosols using project-averaged values from the Pacific Atmospheric Sulfur Experiment (PASE) conducted in 2007. Using chemical kinetic theory, the amount of SO_2 oxidized during a single cloud encounter lasting 7 minutes is 50 ± 30%. The ratio of dimethyl sulfide to SO_2 during individual cloud encounters is used to approximate the consumption of SO_2 using method two. Again the loss rate is found to be 50 ± 30%. The third approach estimates conversion with a sulfur flux budget. This method suggests 33-46% total SO_2 is consumed to produce 45-80% of the total sulfate. It is important to note that SO_2 concentrations during PASE are between 1-100 ppt, significantly lower than concentrations in the vicinity of Kīlauea.

1.5 Goals and Document Organization

It is the goal of this research to quantify the conversion rate of sulfur dioxide to sulfate aerosol downwind of Kīlauea volcano on the island of Hawai‘i. Several measurement campaigns have found sulfur dioxide loss rates, but the distinction between gas phase and aqueous phase conversion has not been made clear in many instances resulting in large uncertainty in loss rates. Observations during these campaigns suggest that sulfur dioxide emissions interacting with clouds or fog produce substantially more sulfate aerosols than through processes in clear air. It is the clear air, gas conversion that will impact ground-level concentrations of SO_2 and sulfate aerosols regularly and is of most interest here. Furthermore, only Porter et al. [2002] have quantified sulfate production rates from volcanic emissions by measuring sulfur dioxide and aerosols simulataneously.

The distinction between sulfur dioxide to sulfate aerosol conversion rates in the gas and aqueous phases is necessary to clarify the uncertainty in past estimates. Theoretical conversion rates were calculated for both gas and aqueous phase reactions during both day and night. Observations were collected to estimate environmental conversion rates to reduce uncertainty in theoretical calculations. Theoretical gas phase conversion rates were then refined using observational data and used to construct a new sulfur dioxide conversion routine for the UH Vog Model. It was hypothesized that a more detailed representation of the gas phase sulfur chemistry will produce improved forecasts resulting in higher probability of detection for poor air quality events.

This document is organized into four sections as follows. Sulfur chemistry theory is presented in section two. Field experiments to measure bulk conversion rates of sulfur dioxide to sulfate aerosol is discussed in section three, including methods, observations, and analysis. In section four, a conversion routine is described and evaluated in the UH Vog Model. Section five provides a summary of research observations and conclusions as well as a list of future research and model development needs to build on the findings presented here.

Many attempts have been made to estimate SO_2 to sulfate aerosol conversion rates from volcanic emissions, but none have attempted to use these to forecast emission plume evolution and downstream concentrations of SO_2 and sulfate. This study is the first to do so in an effort to improve air quality forecasting.

CHAPTER 2. SULFUR DIOXIDE TO SULFATE AEROSOL CHEMISTRY

2.1 Introduction

Chemical kinetic theory and observations have shown differences in the efficiency between cloud-free, gas oxidation of sulfur dioxide and aqueous, in-cloud oxidation. There are a number of variables that are thought to influence these processes. Among them are solar insolation, atmospheric mixing, temperature, relative humidity (RH), pH of cloud droplets, and species' concentrations. Two dominant reaction pathways have been identified for the oxidation of sulfur dioxide in Hawai'i. The gas phase pathway is via reaction with the hydroxyl radical, OH. The aqueous phase pathway is via reaction with hydrogen peroxide, H_2O_2.

Given chemical kinetic theory, what range of conversion rates can one expect in the presence of SO_2 emissions from Kīlauea volcano? This will be addressed through a detailed examination of the reaction kinetics of SO_2 with the hydroxyl radical and hydrogen peroxide, including determinations of important variables that influence SO_2 to sulfate conversion. Theoretical conversion rates are then estimated with locally observed quantities and compared with past research. Lastly, the uncertainty of theoretical conversion rates is discussed to highlight the difficulty in estimating the quantity and to provide a baseline for conversion rate estimates from observations.

2.2 Gas Phase

Past research has determined that only the hydroxyl radical, OH, is important for the oxidation of sulfur dioxide to sulfate aerosol in the gas phase during daytime [Eatough et al., 1994; and references therein]. The hydroxyl radical is formed

through photolytic reactions and therefore has diurnal and seasonal cycles. OH is considered the most important oxidizing agent in the atmosphere because it is extremely reactive and able to oxidize most chemicals found in the atmosphere [ESPERE Climate Encyclopedia, 2006]. Despite being highly reactive, OH concentrations remain relatively constant (~ 1.0 part per trillion or ppt) meaning production and loss rates are in balance. Ozone (O_3) is considered the main precursor for OH formation while in the remote marine boundary layer OH is removed through reactions with carbon monoxide (CO) and methane (CH_4).

Once OH is formed the main reaction pathway with SO_2 is:

$$OH + SO_2 + (O_2, N_2) \Rightarrow HOSO_2 + (O_2, N_2) \quad (2.1)$$

$$HOSO_2 + O_2 \Rightarrow SO_3 + HO_2 \quad (2.2)$$

$$SO_3 + H_2O \Rightarrow H_2SO_4 \quad (2.3)$$

A significant fraction of $HOSO_2$ eventually becomes H_2SO_4. Reaction 2.1, between OH with SO_2, is known to be the rate-limiting step in the oxidation of sulfur dioxide to sulfate aerosol. The formation rate of sulfate aerosol, S, can be solved via

$$S = k[SO_2][OH] \quad (2.4)$$

where k is the conversion rate constant (cm^3 $molecules^{-1}$ s^{-1}), and [SO_2] and [OH] are species concentrations (molecules cm^{-3}) [Raes et al., 1992; Simpson, 2010].

Many values have been obtained for *k* at different reference temperatures. The uncertainty of *k,* according to Atkinson et al. [1989], is of the order of a factor 2($\Delta\log(k) = \pm 0.3$). Based on this uncertainty, Raes et al. [1992] used a range of k values from 4.5×10^{-13} to 2.4×10^{-12} cm^3 $molecules^{-1}$ s^{-1} to determine model sensitivity. They found that model results match smog chamber results for a range

of values from 7.8 x 10^{-13} to 1.0 x 10^{-12} cm^3 $molecules^{-1}$ s^{-1}. For comparison the Jet Propulsion Laboratory (JPL) recommended value for k = 1.6 x 10^{-12} cm^3 $molecules^{-1}$ s^{-1} at a temperature of 300 K [Sander et al., 2011] falls within the range of estimates by Raes et al. [1992].

The reaction represented by equation (2.1) has been found to be a function of temperature and relative humidity. Eatough et al. [1994] developed two equations to incorporate the moisture and temperature dependence into calculations for the rate coefficient k. The moisture dependence is described by the dewpoint temperature (T_D) and reference values of k and T_D at 25°C (Eq. 2.5). The temperature dependence was found through a linear regression fit of 109 k values to 1/T (K) (Eq. 2.6). This fit was performed by normalizing all values to 50% RH. The conversion rate at any temperature, T, calculated from equation 2.6 can be converted to any RH using equation 2.5 [Eatough et al. 1994].

$$\frac{\Delta \ln k_1}{\Delta T_D} = 0.0452°C^{-1} \tag{2.5}$$

$$\ln k_1 = (24.91 \pm 0.41) - (8290 \pm 390)/T \tag{2.6}$$

In order to solve equation (2.4), OH concentrations have to either be measured or modeled with a photochemical model. Although OH is not routinely observed, past field campaigns have collected OH data. The most relevant data to Hawai‘i is from INTEX-B collected between 05-07 UTC 1 May 2006. Although this was an overnight flight, it provides a lower bound on the OH diurnal cycle. A mean OH concentration of approximately .01 ppt (~2.5 x 10^5 molecules cm^{-3}) is found.

The diurnal cycle of OH is best illustrated by data from the NASA-P3 during PEM-Tropics B flights 6 and 7 (Figure 1) [Mauldin et al. 2001]. Several legs were flown near the surface during both day and night. Daytime concentrations peaked between 6 x 10^6 molecules cm^{-3} and 1 x 10^7 molecules cm^{-3} with nighttime concentrations approximately two orders of magnitude lower.

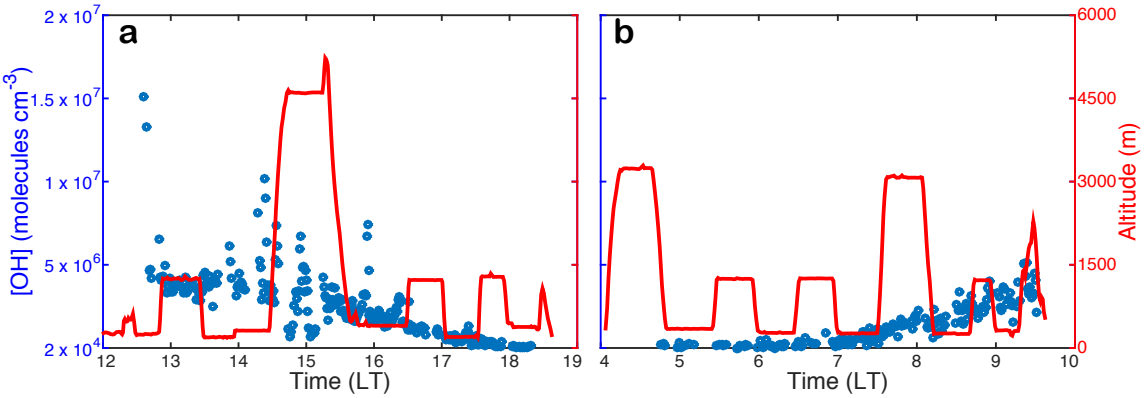

Figure 4: Concentrations of OH (blue dots) measured during flight 6 (a) and 7 (b) during the PEM-Tropics B study. Also shown for reference is an altitude profile (m) for each flight in red. Data are presented as one-minute average [OH]. Adapted from Mauldin et al. [2001].

Further studies have found similar diurnal cycles of OH in the mid-latitudes during various seasons [Forberich et al., 1999; Hand et al., 1986]. Hand et al. [1986] found a range of OH concentrations from a peak of 4 x 10^6 molecules cm^{-3} during the day to a minimum that oscillated about 1-5 x 10^5 molecules cm^{-3} overnight. Forberich et al. [1999] found a larger daytime range over several days from an early morning minimum on the order of 10^5 molecules cm^{-3} to a maximum of 8-11 x 10^6 molecules cm^{-3}.

Hypothetical limits of sulfur dioxide oxidation by the hydroxyl radical can be calculated with the use of values from Figure 4 and equation (2.4). For this calculation hourly average temperature and RH values from 20 July 2014 at Hawai‘i

Volcanoes National Park Observatory (HAVO-OB) were used to determine *k*. This site is chosen for its proximity to the Halema‘uma‘u Crater vent. Nighttime and daytime temperature and RH values for HAVO-OB were 17.1°C and 100% and 21.9°C and 79%, respectively. An SO_2 concentration of 2.46 x 10^{11} molecules cm^{-3} (10 ppb) is used for both daytime and nighttime calculations. OH concentrations are obtained from PEM-Tropics B data represented in figure 4 and set at 2 x10^5 molecules cm^{-3} and 1 x 10^7 molecules cm^{-3} for night and day, respectively. The subsequent k values calculated from equations (2.5) and (2.6) were 4.04 x 10^{-13} molecules cm^{-3} s^{-1} and 5.58 x 10^{-13} molecules cm^{-3} s^{-1} for night and day, respectively. The difference in k values is approximately 30%, given the relatively small ΔT (4.8°C) and ΔRH (21%). If one assumes 100% conversion, this results in SO_2 to sulfate conversion rates of 1.98 x 10^4 molecules cm^{-3} s^{-1} and 1.37 x 10^6 molecules cm^{-3} s^{-1} for night and day, respectively. That works out to 7.13 x 10^7 molecules cm^{-3} h^{-1} and 4.9 x 10^9 molecules cm^{-3} h^{-1} for night and day, respectively. By percentage of SO_2 concentration for each time period that works out to a rate of .03% h^{-1} and 2% h^{-1} for nighttime and daytime.

These rates of sulfate formation are lower than those found by Porter et al. [2002] but are within the range of values for SO_2 loss found elsewhere [McGonigle et al., 2004; Rodriguez et al., 2005]. The uncertainty in *k,* represented in equations (2.6), results in a range from 2.29 x 10^{-13} to 1.42 x 10^{-12} molecules cm^{-3} s^{-1} during the day and 1.64 x 10^{-13} to 1.06 x 10^{-12} molecules cm^{-3} s^{-1} at night. The range of corresponding conversion rates is 0.8 - 5% h^{-1} during the day and 0.01 - 0.07% h^{-1} at night.

It is important to note that theoretical conversion rate coefficients are meant to represent standard atmospheric conditions. A typical atmospheric concentration of SO_2 is in the range of 1-100 ppt (2.46×10^7 molecules cm^{-3} to 2.46×10^9 molecules cm^{-3}), much lower than the concentration used above (10 ppb). SO_2 concentrations can easily exceed 100 ppm (2.46×10^{15} molecules cm^{-3}) above Halemaʻumaʻu Crater vent (Andrew Sutton 2015, personal communication). Given such high concentrations of SO_2, eight to nine orders of magnitude greater than OH, the reaction rate would be limited by OH concentrations and how rapidly OH can be produced. This will be discussed in more detail in a later section.

Theoretical, gas phase conversion rates estimated for conversion of SO_2 to sulfate aerosol display rates less than 10% h^{-1}. Daytime conversion rates are estimated to be 2.9 ± 2.1 % h^{-1} while nighttime conversion rates are estimated to be 0.04 ± 0.3 % h^{-1}. Very high concentrations of SO_2 have been observed near the vents and could lead to this reaction being severely limited by availability of OH. There is some uncertainty in the rate that stems from the temperature and moisture dependence of the reaction between OH and SO_2, which is represented in the conversion rate coefficient, k. Sander et al. [2011] suggest the uncertainty associated with the temperature dependence of the reaction is minimized near room temperatures (25-27°C) - a temperature range typical of Hawaiʻi's climate.

2.3 Aqueous Phase

When SO_2 dissolves in water it forms a weak acid that undergoes two dissociations to form a total of three species, $HSO_3^-, H_2O \cdot SO_2, SO_3^{2-}$, the sum of which are known collectively as S_{IV}. The solubility of SO_2 is a function of temperature and pH of the solution. At pH 2-7, S_{IV} is almost entirely in the form of the bisulfite ion (HSO_3^-) [Seinfeld and Pandis, 1998]. At lower temperatures there will be higher solubility. At the same time the reaction rate will decrease with decreasing temperature, however, the increased reactant concentration will tend to counterbalance the decreased reaction rate [Eatough et al., 1994].

Hydrogen peroxide (H_2O_2) and ozone (O_3) are the most likely oxidants for SO_2 in the aqueous phase. However, ozone reactions are highly pH dependent and only become the leading oxidant at pH > 5.5 [Hegg, 1989; Seinfeld and Pandis, 1998]. Hydrogen peroxide reactions are relatively independent of pH (Figure 5). The pH of atmospheric water droplets reported is typically 3-6 [Eatough et al., 1994]. Rainwater samples taken in Hawai‘i have yielded an average pH = 4.5 [Miller and Yoshinaga, 1981] while Siegel et al. [1990] found 84% of rain samples downwind of Kīlauea had pH values less than 5.0. The large particle size of rain droplets relative to cloud droplets suggests that the pH of the smaller volume cloud droplets will likely be even lower and the pH of rain droplets represents an upper limit. This suggests that hydrogen peroxide is the leading oxidant of sulfur dioxide in the vicinity of Kīlauea. Hydrogen peroxide, like the hydroxyl radical, is produced photochemically, both in the gas phase and aqueous phase [Warneck, 1999]. The

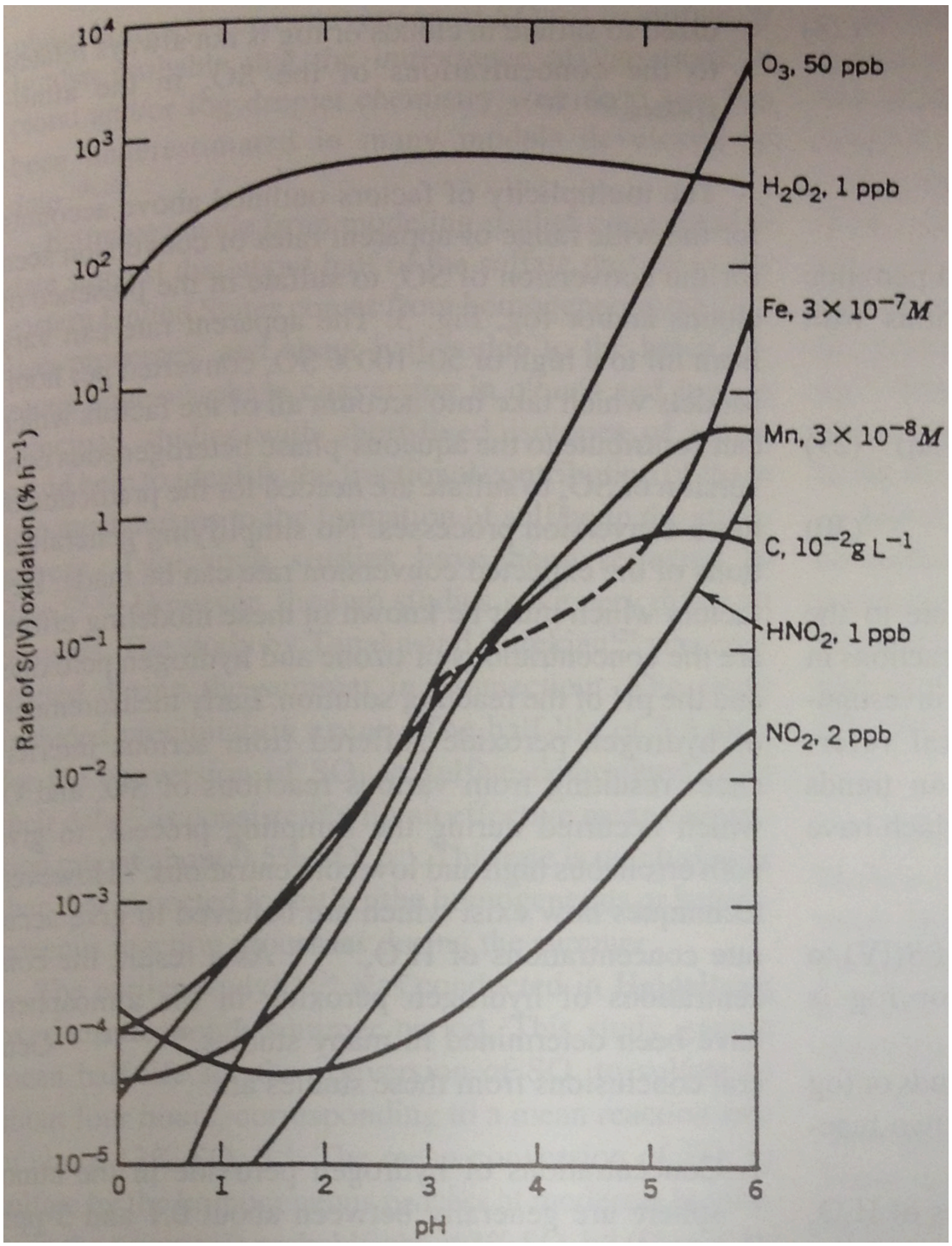

Figure 5: Variations for reaction rate constants for the oxidation of aqueous S(IV) by various oxidants as a function of the solution pH. Adapted from Eatough et al. [1994].

average concentration of hydrogen peroxide found during PASE was 1.0 ppb [Simpson, 2010].

In order for the aqueous phase reaction to occur, both sulfur dioxide and hydrogen peroxide gases must be dissolved in cloud water. Hydrogen peroxide is considered highly soluble and sulfur dioxide moderately soluble. Equilibrium between the gas and aqueous phase concentrations is reached on very short time scales relative to droplet lifetime so that equilibrium can be considered. This allows the use of Henry's Law constants to determine aqueous phase concentrations. Henry's Law has a strong dependence on temperature. This dependence has been found by Huang and Chen [2010] for hydrogen peroxide and can be expressed as

$$K_H[\mathrm{H2O2}] = exp\left(\frac{a}{T} - b\right) \tag{2.7}$$

where a =7024 ± 138 and b = 11.97 ± 0.48 and T (K) is the equilibrium temperature. Huang and Chen [2010] showed this relation to be relatively independent of solution pH in the range of 1 - 7. This relationship results in $K_H[H_2O_2] = 1.08 \times 10^5$ M atm^{-1} at 25°C [Huang and Chen, 2010], where M, molarity, is the concentration of solute in solution expressed as 1 mol L^{-1} or 1 x 10^{-3} mol cm^{-3}. The recommended value of $K_H[H_2O_2]$ by the JPL is 8.44×10^4 M atm^{-1} (for 278 K < T < 303 K) with temperature dependence values a=7600 and b=14.16 [Sander et al., 2011]. The recommended value for $K_H[SO_2]$ from JPL is 1.36 M atm^{-1} and the temperature dependence is given by

$$K_H[\mathrm{SO2}] = exp\left(\frac{a}{T} - b + cT\right) \tag{2.8}$$

where a = 4250, b = 39.72, and c = 4.525 [Sander et al., 2011]. The uncertainty in K_H is given as 10 to 50%.

The aqueous phase reaction of sulfur dioxide and hydrogen peroxide is expressed by Hoffman and Calvert [1985] as

$$-\frac{d[S_{IV}]}{dt} = \frac{k[H^+][H_2O_2][HSO_3^-]}{1 + K[H^+]} \tag{2.9}$$

where the reaction constant, k = 7.45x 10^7 M^{-2} s^{-1}, K = 13 M^{-1} at 298 K, $[HSO_3^-] \approx [SO_2](aq)$, since it is assumed that most dissolved SO_2 is in the form of bisulfite, and $[S_{IV}] \approx [SO_2](aq)$. Martin and Damschen [1981] provide another popular estimate of k = 5.2 x 10^6 M^{-2} s^{-1}. The concentration of the hydrogen ion, $[H^+]$, is the estimate of water droplet pH. A pH of 4.5 is assumed here which corresponds to an H^+ concentration of 3.16 x 10^{-5} M. Given this pH value and that the reaction is relatively independent of pH, the denominator is approximately 1, and equation (2.9) becomes

$$-\frac{d([SO_2](aq))}{dt} = k[H^+][H_2O_2][SO_2](aq) \tag{2.10}$$

where k = 9.1 (± 0.5) x 10^7 M^{-2} s^{-1} as proposed by Maass et al. [1999]. Caffrey et al. [2001] found this kinetic relation to work best for their modeling of cloud particle growth. If we assume 100% conversion efficiency to sulfate aerosol, equation (2.10) can be treated as an aerosol production equation by changing the left hand term to

$$\frac{d([SO_4](aq))}{dt} = k[H^+][H_2O_2][SO_2](aq) \tag{2.11}$$

The limiting factor of this reaction rate will be the lower of the two solute concentrations.

Overnight observations at HAVO-OB on 20 July 2014 are used to estimate aqueous phase conversion rates because RH = 100% during this period. K_H values are corrected for pressure (altitude) using the 2014 annual mean station pressure from HAVO-OB. Values calculated from equations (2.7) and (2.8) at a temperature = 290.35 K and p = 0.867 atm are $K_H[H_2O_2] = 1.78 \times 10^5$ M atm^{-1} and $K_H[SO_2] = 1.55$ M atm^{-1} for hydrogen peroxide and sulfur dioxide, respectively. When multiplied by the gas concentrations for H_2O_2 (1×10^{-9} atm^{-1}) and SO_2 (1×10^{-8} atm^{-1}) the aqueous phase concentrations are 1.78×10^{-4} M and 1.55×10^{-8} M, respectively.

Note that the SO_2 gas ($[SO_2](g)$) concentration is an order of magnitude greater than $[H_2O_2](g)$, but the solubility of H_2O_2 results in dissolved concentrations of $[H_2O_2](aq)$ four magnitudes greater than $[SO_2](aq)$. Thus, $[SO_2](aq)$ concentrations will be lower than $[H_2O_2](aq)$ initially, however, higher $[SO_2](g)$ concentrations will continue to dissolve and react with $[H_2O_2](aq)$ and ultimately $[H_2O_2](g)$ will be the limiting reactant. Using the rate coefficient, $k = 9.1 \times 10^7$ M^{-2} s^{-1}, provided by Maass et al. [1999] the loss rate of $[SO_2](aq)$ is 7.9×10^{-9} M s^{-1}, or roughly a 50% decrease in $[SO_2](aq)$ per second. This rate is an order of magnitude higher than past theoretical conversion rates found by Seinfeld and Pandis [1998], likely due to a difference in magnitudes of Henry's Law constants and higher SO_2 concentrations being used here. Again, 100% conversion has been assumed for this reaction, which may be unrealistic and have led to extremely high conversion rates.

This reaction is known to be very fast and should deplete all H_2O_2 within a matter of minutes, which is the typical residence time of an air parcel in-cloud. Measurements by Daum et al. [1984] suggest that both reactants rarely coexist in

clouds or fog. Further evidence in measurements by Barth et al. [1989] reveal that aqueous concentrations of hydrogen peroxide are always below those expected in equilibrium from Henry's Law. This suggests that the sulfur dioxide sink is removing hydrogen peroxide faster than it can be replaced. In light of these observations and results stated above it is important to assess the uncertainty in the reaction rate because a significant depletion of H_2O_2 will make reactions between SO_2 and other reactants increasingly important.

Much of the uncertainty associated with the aqueous phase reaction of SO_2 with H_2O_2 stems from the uncertainty in the temperature dependence of the Henry's Law constants and the conversion rate coefficients. The uncertainty for $K_H[SO_2]$ is approximately 50% [Sander et al., 2011] while $K_H[H_2O_2]$ is less than 1% (1.76 (± 0.01) x 10^5 M atm^{-1}). Since the reaction is limited by H_2O_2 concentrations any error resulting from uncertainty in SO_2 solubility is negligible. Estimates of k range from 5.2 x 10^6 M^{-2} s^{-1} to 9.6 x 10^7 M^{-2} s^{-1}. By using the lower bound $[SO_2](aq)$ loss will be 3% per second - roughly a factor of 17.5 less than the upper bound estimate. While this lower conversion rate will deplete H_2O_2 much slower, estimates from Hua et al. [2008] suggest H_2O_2 production peaks at less than 1 ppb h^{-1}, meaning that over time (especially overnight) H_2O_2 may still be depleted.

If the rate of H_2O_2 production cannot keep pace with removal through aqueous SO_2 reactions than secondary reaction pathways will become important. Although O_3 reactions are more dependent on solution pH, this pathway remains important at pH 3-6 (Figure 5) should H_2O_2 be absent in significant concentrations [Eatough et al., 1994]. O_3 concentrations in the marine boundary layer are higher

than H_2O_2, with mean concentrations between 15-19 ppb, and it is moderately soluble with a Henry's Law coefficient of 1.3 x 10^{-2} M. The O_3 rate expression is given as

$$-\frac{d[\mathrm{S_{IV}}]}{dt} = (k_0[\mathrm{SO_2 \cdot H_2O}] + k_1[\mathrm{HSO_3^-}] + k_2[\mathrm{SO_3^{2-}}])[\mathrm{O_3(aq)}] \quad (2.12)$$

where k_0 = 2.4 x 10^4 M^{-1} s^{-1}, k_1 = 3.7 x 10^5 M^{-1} s^{-1}, and k_2 = 1.5 x 10^9 M^{-1} s^{-1} [Hoffman and Calvert, 1985], however, if all H_2O_2 is consumed in reactions with SO_2 then solution pH can easily drop below 3 making this reaction negligible.

Emission estimates from Halemaʻumaʻu Crater in 2008 by Mather et al. [2012] show traces of Fe and Mn are being emitted, making conversion via these pathways possible as well. Figure 5 suggests that these reactants may be important conversion mechanisms near Halemaʻumaʻu Crater from pH 3.5 to 6. The rate expressions are given as

$$-\frac{d[\mathrm{S_{IV}}]}{dt} = k_{Fe}[\mathrm{Fe(III)}][\mathrm{SO_3^{2-}}] \quad (2.13)$$

$$-\frac{d[\mathrm{S_{IV}}]}{dt} = k_{Mn}[Mn(II)][S_{IV}] \quad (2.14)$$

where k_{Fe} = 1.2 x 10^6 M^{-1} s^{-1} for pH ≤ 5 [Hoffman and Calvert, 1985] and k_{Mn} = 1000 M^{-1} s^{-1} [Martin and Hill, 1987]. Fe and Mn emissions are estimated by Mather et al. [2012] as the ratio of Fe mass with SO_2 mass = 7.7 x 10^{-5} and Mn mass with SO_2 mass = 1.4 x 10^{-6}. Given an SO_2 emission rate of 3000 t d^{-1} this amounts to Fe emission of 0.231 t d^{-1} and Mn emission of 4.2 x 10^{-3} t d^{-1}. $PM_{2.5}$ speciation measurements available from the Interagency Monitoring of Protected Visual Environments (IMPROVE) site at Hawaii Volcanoes Visitor's Center display 24-hr concentrations of Mn = 1.6 x 10^{-4} μg m^{-3} and Fe = 9.4 x 10^{-3} μg m^{-3}. If one assumes all this mass is

dissolved in cloud and assume a sulfur species concentration of 1.55 M then the reaction rate for Fe = 3.1×10^{-7} M s^{-1} and Mn = 4.5×10^{-12} M s^{-1}. The reaction with Mn can be neglected because of its magnitude but the reaction rate with Fe is more rapid than with H_2O_2. The assumption that all Fe will dissolve is unrealistic. If instead one assumes that only 1% is dissolved then the rate drops to 3.1×10^{-9} M s^{-1}. This reaction rate is still fast enough to compete with hydrogen peroxide. Figure 5 shows this reaction is also highly dependent on solution pH suggesting such high concentrations of Fe in solution may be unrealistic. However, given the relatively high emission rate of Fe this reaction may be important near the vent, especially in the presence of clouds or fog at the summit of Kīlauea.

A further mechanism for SO_2 oxidation in solution is proposed via halogen compounds HOCl and HOBr [Vogt et al., 1996]. Keene et al. [1998] find reactions with HOCl to be more rapid than H_2O_2 at a pH range from 3 – 5.5 and HOBr more rapid than H_2O_2 at pH 5.5. Due to the low pH in Hawai‘i, the HOBr reaction can be neglected. HOCl concentrations are 10 ppt while H_2O_2 concentrations are 600 ppt in the study of Keene et al. [1998]. So while the reaction rate may be faster, the total amount of SO_2 a 10 ppt HOCl concentration is able to convert is less than 2% of the total amount from a 600 ppt H_2O_2 concentration. Thus the HOCl mechanism is responsible for a trivial amount of SO_2 to SO_4 conversion and can be neglected.

2.4 Summary

Estimates of gas and aqueous phase oxidation of SO_2 at Kīlauea Volcano have been calculated to document that hydroxyl radical and hydrogen peroxide are the dominant reaction pathways. The range of conversion rates from these reaction pathways are estimated, where the range is representative of the uncertainty. Limitations of these reaction rates theoretically exist based on environmental factors and emission rates.

Oxidation of SO_2 in the gas phase is dominated by reactions with the hydroxyl radical, OH. Reaction rates are estimated for daytime and nighttime conditions observed at HVO. Daytime rates range from 0.8 to 5% h^{-1} and nighttime rates range from 0.01 to 0.07% h^{-1}. Since OH concentrations and production peak during the day and production ceases overnight, this diurnal signal is expected. Uncertainty in the conversion rate is a result of the temperature and moisture dependence of the reaction and is represented through the reaction coefficient, k. This reaction will be limited by the lower reactant concentration. Under most circumstances the limiting agent will be SO_2, however near Halemaʻumaʻu Crater SO_2 concentrations can exceed 100 ppm. Under such conditions OH would be completely depleted through reactions with SO_2 and will be the limiting agent. This reaction limit is reached with SO_2 concentrations as low as 10 ppm, however concentrations of this magnitude are not common beyond a few kilometers downwind from the source. A more detailed discussion of this reaction-limiting process will be covered during the discussion of observations in the following chapter.

The aqueous phase oxidation of SO_2 is dominated by reaction with hydrogen peroxide, H_2O_2, because of the independence of this reaction on solution pH between 2-7. Past observations of pH in Hawai‘i suggest a likely range of pH values between 3 and 5.5. H_2O_2 is highly soluble while SO_2 is moderately soluble resulting in higher initial solution concentrations of H_2O_2 than SO_2, however given lower ambient concentrations of H_2O_2 than SO_2 in the gas phase, H_2O_2 will be the limiting factor. Estimated reaction rates suggest a conversion rate of dissolved SO_2 between 3-50% s^{-1}. Such a rapid reaction coupled with a rapid diffusion process is unsustainable over long periods of time and will quickly lead to the depletion the limiting reactant. Given that parcels of air spend no more than a few minutes in-cloud and the observations of Daum et al. [1984] and Barth et al. [1989], the reaction is limited by the ambient H_2O_2 concentrations. Thus for an air parcel penetrating a cloud with 10 ppb SO_2 and 1 ppb H_2O_2, the maximum loss of SO_2 through conversion to SO_4 is 1 ppb.

Other aqueous phase reactions via O_3, Fe(III), and Mn(II) are considered to determine if the conversion rate is significant relative to H_2O_2. O_3 reactions are highly pH dependent and would become important only in the event that H_2O_2 is drawn down first. A reduction in H_2O_2 via reaction with SO_2 will produce sulfuric acid, H_2SO_4, and thus also reduce solution pH making any contribution from O_3 negligible. Fe and Mn are emitted from Halema‘uma‘u [Mather et al., 2012] and are measured by the IMPROVE network at Hawai‘i Volcanoes National Park. Measured concentrations of Fe and Mn and reaction kinetics suggest that reactions with Mn are negligible as well. If as much as 1% of emitted Fe is dissolved in solution,

reaction kinetics indicate this process could compete with H_2O_2. This importance of this reaction is limited to the region around the vents due to low Fe emission rates but periods of clouds near the summit of Kīlauea will increase the significance of this rapid reaction rate.

The oxidation of SO_2 from Kīlauea is dominated by the hydroxyl radical in the gas phase and hydrogen peroxide in the aqueous phase. Given high SO_2 emissions from the summit vent at Halemaʻumaʻu Crater, the oxidation by these reactants is limited by their modest ambient concentrations. Under such circumstances secondary reactions may become important, such as Fe(III) for aqueous conversion. However these circumstances are limited to SO_2 concentrations ≥ 10 ppm and high concentrations of Fe that are typically only found close to the emission source. Beyond that oxidation via OH is expected in the range of 0.8 to 5% h^{-1} and oxidation via H_2O_2 is limited in-cloud by ambient concentrations but can reach 100% for SO_2 gas concentrations < H_2O_2 gas concentrations.

CHAPTER 3. OBSERVATIONS

3.1 Introduction

Historically, estimates of SO_2 loss from volcanoes have not been adequately compared to theoretical conversion processes. Thus there is little understanding of the sulfur chemistry occurring inside volcanic plumes. By taking measurements of the emission plume at Kīlauea, it is possible to constrain theoretical conversion rate estimates of sulfur dioxide to sulfate aerosols.

Based on past observation campaigns [Oppenheimer, 1998; Porter et al., 2002; McGonigle et al., 2006; Nadau, 2006], this is done by performing transects under the plume to detect SO_2 and/or aerosols. However, the possibility of driving transects at any distance downwind of Kīlauea is made difficult by a lack of roadways. A scanning strategy is also made difficult by terrain, sun interference, and low, near-ground plume heights (Andrew Sutton 2014, personal communication). Due to consistent trade wind patterns combined with the effects of trade winds impinging on the high terrain of Hawai‘i, stationary measurements of the plume are possible over long periods of time.

High-resolution measurements of SO_2 are possible in clear air using correlation spectrometers such as the FLYSPEC [Elias and Sutton, 2012; Horton et al., 2006; Nadau, 2006]. Simultaneous measurements of aerosol optical depth (AOD) using sun photometers can be used to constrain the loss of SO_2 since oxidation largely results in the creation of sulfate aerosols (SO_4) [Porter et al., 2002], which are optically active. Photometer measurements are not continuous in time, however they can be used to calibrate lidar measurements. Continuous lidar scans

provide information on the vertical distribution of aerosols, which is not possible with photometer measurements of AOD. Münkel et al. [2004] and Charles et al. [2007] have found high correlations between ceilometer observations near the ground and both PM_{10} and $PM_{2.5}$ observations.

A good estimation of plume speed is required to calculate fluxes and determine the time period over which conversion occurs between measurement transects or scans. Due to the terrain at Kīlauea and nature of the plume near the ground, surface wind speeds can adequately describe plume speed (Tamar Elias 2014, personal communication).

In order to observe the plume with ground-based remote sensing instruments, a few environmental conditions need to be met. Days when trade winds are forecast from a mean direction between 10° and 70° are required to collect SO_2 observations close to the vent at Halemaʻumaʻu Crater with the stationary FLYSPEC array operated by HVO. Ideally, atmospheric conditions will allow a plume feature to be identified and tracked visually so that observations of this feature can be made as it propagates downstream. Cloudless skies help to visually track the plume but are also necessary to collect AOD observations. The second, downwind observation location is mobile, allowing observations to be taken far downstream the windward coast on Mamalahoa Highway (Rt. 11) starting at Hawaiʻi Volcanoes National Park (HVNP) down to Nā ʻālehu, near South Point, over a distance of ~50 km (Figure 1).

Once observations are collected, they are temporally averaged and multiplied by plume speed to come up with an SO_2 flux rate and SO_4 flux rate at each location.

SO_2 loss rates and SO_4 production rates are then derived from differences in flux rates at adjacent sites using

$$\Phi = \Phi_0 e^{-kt} \tag{3.1}$$

where Φ_0 is the initial flux, Φ is the flux after some time, t, and k is the SO_2 loss (SO_4 production) rate. These estimates, when compared with theoretical conversion rates, provide a baseline for future estimates.

Measurements of aqueous-phase conversion are challenging using ground-based remote sensing. UV spectrometers are not be able to detect SO_2 for optically thick clouds, though it may be possible to measure inflow and outflow to give an approximation of in-cloud conversion. While lidars are able to detect aerosols, differentiating between sulfates and cloud droplets is impossible without multiple wavelength lidars. Sulfate aerosols occur predominantly in the accumulation mode [Altshuller, 1982], however it is impossible to disentangle the effects of accumulation, RH, and droplet volume with remote sensing instruments to get sulfate information. If conversion is high in the region of cloud/plume interaction a peak in lidar backscatter may signify sulfate formation. A stationary orographic cloud is necessary to obtain such observations and the likelihood of observing such an event is low. Due to the challenges posed for observing aqueous phase conversion, the observing strategy focuses on obtaining measurements to estimate gas phase conversion only.

It is becoming increasingly popular to perform virtual field campaigns prior to entering the field with real instrumentation. In this way, one can test a variety of measurement strategies and work out expected and unexpected problems that may

arise in the field. The goal is to improve strategies for collecting meaningful data. In this instance, there is also a real possibility that environmental conditions during the period of the field campaign will not be conducive for observations with ground based remote sensing instruments (i.e., overcast conditions, precipitation, weak winds, southerly or westerly winds).

A virtual field experiment (VFE) provides an alternative to collecting real observational data when it becomes unavailable. In the following section a VFE will be described and results discussed, including challenges in obtaining simulated observations. Based on the results of the VFE a refined approach was undertaken in a field experiment, as described in section three, including a description of instrumentation and data reduction methodology. The results of the field experiment will be covered in section four, including the estimated conversion rates. Finally, section five will contain a summary of the field experiment and conclusions.

3.2 Virtual Field Experiment

A virtual field experiment was performed using University of Hawai‘i Vog Model output from February 3, 2015. The model was forced with 1.0 km Weather Research and Forecast model (WRF) forecast grids from Mauna Kea Weather Center (MKWC) and mean SO_2 flux rates from Hawai‘i Volcanoes Observatory (HVO). A period of northeasterly trade wind flow observed at surface stations near the Halema‘uma‘u Crater vent was used for this test case. The plumes were represented by Gaussian puffs in the horizontal and 3-D particles in the vertical. This was done to be able to quantify model dispersion of the plume and to clearly detect plume extent.

Model forecasts of SO_2 and SO_4 concentrations were output on 11 unevenly spaced levels from 10 m to 2800 m (AGL). Columnar pollutant concentrations were extracted for the two observation traverse/scan sites to derive simulated measurements (Figure 6). The proximal observation site (site 1) was within the stationary FLYSPEC array operated by HVO just downwind of Halema‘uma‘u Crater (Figure 6). The distant site (site 2) was chosen based on UH Vog Model forward trajectories and WRF wind fields, and was just off Rt. 11. Forward trajectories suggested vertical wind shear in the boundary layer that could disperse the plume over the course of an hour. Thus site two was chosen to maximize the plume being sampled while keeping the length of plume traverses relatively short to maximize temporal sampling resolution.

Hourly model SO_2 output was used to simulate concentration path-length measurements (ppm-m) obtained with a FLYSPEC, while model SO_4 concentration data was used to simulate AOD values as if measured with a sun photometer. SO_2 forecasts were extracted from nine model levels and converted from g m^{-3} to ppm. The values were then multiplied by the height of the level on which they were reported to produce path-length concentrations (ppm-m).

Flux rates over each traverse were estimated by summing the flux rate (F) for each traverse segment using the formulation from Williams-Jones et al. [2008]

$$F = [\mathrm{SO_2}]_{pl} \cos\theta d_{seg} U C_f \qquad (3.2)$$

where $[SO_2]_{pl}$ is the average SO_2 path-length concentration for each traverse segment, θ is the deviation from the perpendicularity of the segment with respect to the plume, d_{seg} is the length (m) of a particular traverse segment, U is the average

plume speed (m s^{-1}), and C_f is a conversion factor changing ppm m^3 s^{-1} to metric tonnes per day (t d^{-1}). As explained by Williams-Jones et al. [2008], one ppm-m of SO_2 is one cubic centimeter of SO_2 gas uniformly mixed in one cubic meter of air and viewed by the correlation spectrometer over an optical path of one meter at a pressure of 101.325 kPa and a temperature of 20°C. Williams-Jones et al. [2008] define C_f as

$$C_f = \rho_{SO2} C_{fSTP} 0.001\ 10^{-6}\ 86{,}400\ s\ d^{-1} \tag{3.3}$$

where ρ_{SO2} is the density of SO_2 gas at standard temperature and pressure (STP) (2.86 kg m^{-3}), C_{fSTP} is a correction factor to change the SO_2 density from STP to environmental temperature and pressure, 0.001 converts the kg term in the density to metric tonnes, and 10^{-6} represents the mixing ratio of SO_2.

The dependence of SO_2 path-length concentrations on standard temperature and pressure is derived by Gerlach [2003]

$$b_{\mathrm{SO}_2} = \left(\frac{TP_r}{PT_r}\right) b_{\mathrm{SO}_{2\mathrm{r}}} \tag{3.4}$$

where b_{SO2r} is the reference path-length concentration, b_{SO2} is the corrected path-length concentration, P_r and T_r are atmospheric STP values, and T and P are the environmental values.

In the VFE, SO_2 flux rates were estimated from the model data at the two locations presented in figure 6 using equations (3.2)-(3.4). The sampling transects were perpendicular to the plume (θ=0) and corrected for both temperature and pressure. The difference in altitude of the two transects is approximately 300 m. Plume speeds for both transects were estimated from model wind speed profiles

taken near the center of the plume. The average wind speed from the model boundary layer, defined by the temperature profile from the Hilo radiosonde (PHTO), was used to represent the average plume translation speed, U = 8.18 m s^{-1}.

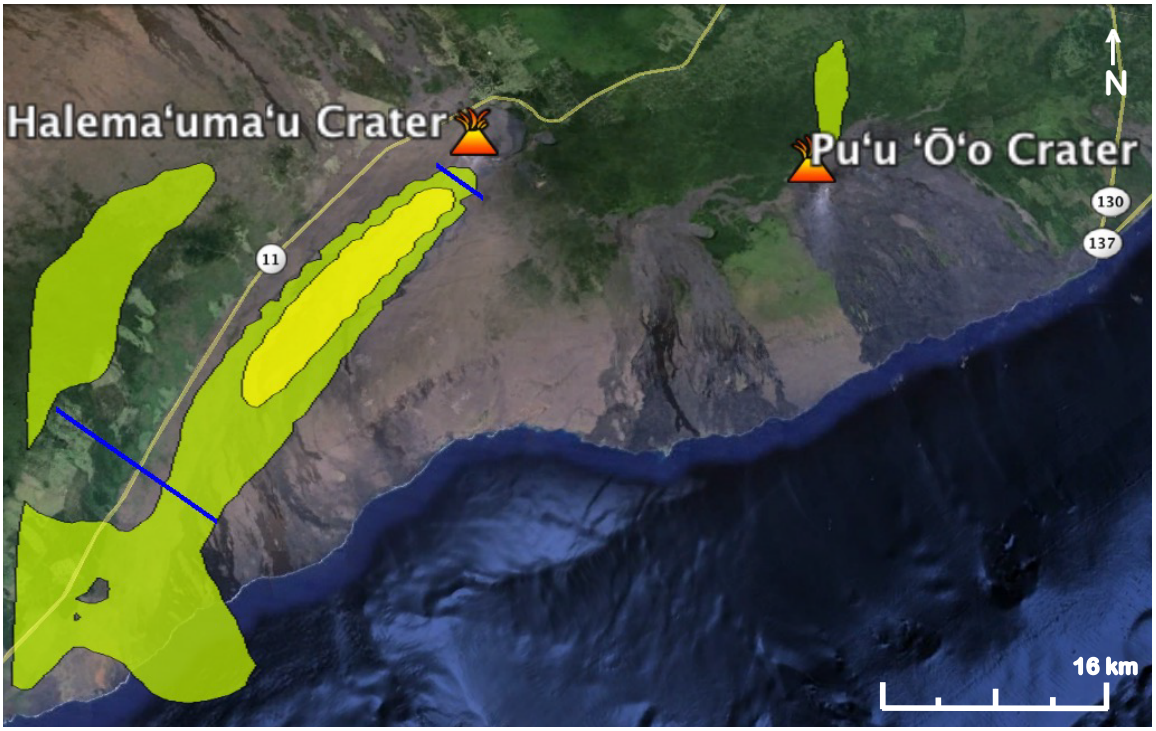

Figure 6: Representation of Virtual Field Experiment at 18 UTC 3 February 2015. The plume is represented by the 1-hr mean SO_2 concentration in the 100-400 m layer AGL. Green areas represent concentrations greater than 0.1 ppm and yellow regions represent concentrations greater than 1.0 ppm. Blue lines indicate locations where model data was used to simulate instrument measurements of the plume done by scans or traverses.

A constant SO_2 to SO_4 conversion rate of 1% h^{-1} was specified in the model and served as the expected value for the VFE. The SO_2 loss rate estimated from simulated data was k = -2.56 x 10^{-5} s^{-1}, much faster than the model defined conversion rate of 1% h^{-1} (-2.77 x 10^{-6} s^{-1}). The reduction in SO_2 flux between site one and two was nearly 10% causing a more rapid conversion rate to manifest. The large reduction in SO_2 flux between measurement sites was caused by plume

dispersion resulting from vertical wind shear. Dry deposition of SO_2 and SO_4 was calculated by the model and found to be trivial to the loss rate. Estimates for plume translation speed or average plume velocity, U, were another large source of uncertainty in these calculations that potentially impacted the flux calculations.

Sulfate particle fluxes were derived from simulated sun photometer AOD measurements. AOD was calculated from model output concentrations of SO_4 based on

$$AOD = \tau = \int_a^b k(\lambda)\, \rho\, ds \tag{3.5}$$

where τ is the AOD, $k(\lambda)$ = 7.7 $m^2\ g^{-1}$ is the mass scattering coefficient derived by Porter et al. [2002], ρ is the density of particles given by the model output, and *ds* is the depth of the layer between a and b as given by model output. The flux of dry sulfate aerosol (F_{SO4}) was then estimated following Porter et al. [2002]

$$F_{SO4} = \left(\frac{U}{k}\right) \sum_{i=1}^{n} (w_i \tau_i) \tag{3.6}$$

where k is the mass scattering coefficient, w_i is the effective width for the interval i, and τ_i is the AOD for the interval (transect).

Based on the calculated fluxes at the two sites an SO_4 production rate was estimated using equation (3.1). The production rate was k = 5.37 x 10^{-4} s^{-1}. This value was more rapid than the loss rate of SO_2 (k = -2.56 x 10^{-5} s^{-1}). This difference may be partially accounted for by the differing parameterized deposition rates for the two species (the SO_2 deposition velocity being twice the magnitude of the SO_4 velocity). The lower observed sulfate levels near the source may bias the calculation

of the SO_4 production rate, suggesting the proximal site (site 1) may need to be moved further downwind from the source.

The results of the virtual field experiment highlighted a number of factors that could complicate the estimates of flux rates from ground based-remote sensing instruments between two distant locations. Complicating factors include dry deposition rates, directional and speed wind shear, and plume dispersion in the horizontal that results in low concentrations that fall below the detection limit. Additionally, when meteorological conditions (stability and or wind speeds) permit emissions from Puʻu ʻŌʻo to be advected in the same direction as Halemaʻumaʻu, additional mass may be included in the flux at one location over another complicating the loss/production estimates.

The idealized sampling strategy used here warrants revision. Although sampling the plume from a fixed location through instrument scans may be possible, other factors may limit the ability to perform measurement scans. Factors include cloud cover, obstructed sightline, and low sun angles. An alternative sampling approach would involve performing observations at a fixed point below the plume. In this way, many of the complicating factors of a scanning strategy can be mitigated.

Regardless of the sampling strategy a large uncertainty in the flux estimates stems from the estimation of the plume speed. Ground-based anemometer measurements and wind profiles from nearby airports have been used frequently as proxies for plume speed, however wind speeds near the plume are not necessarily representative of the speed of the plume itself [Nadau, 2006]. This results in

uncertainties for derived fluxes of 10-40% [Stoiber et al., 1983; Doukas, 2002] to more than 100% [Williams-Jones et al., 2006]. Nadau [2006] estimated plume speed using the multiple-spectrometer method described by Williams-Jones et al. [2006] and compared this with anemometer measurements. Comparison of values showed significantly different estimates of plume speed with no consistency, which ruled out scaling of ground based measurements for plume level winds. The uncertainty of the multiple-spectrometer method is estimated to be 15%.

The following example will demonstrate that rate coefficient calculations are sensitive to estimated plume speed. The wind speed of the lowest model level will be used as the proxy for plume speed for this exercise. At the proximal site the plume speed is 7.1 m s^{-1} and at the distant site it is 0.9 m s^{-1}. The resulting rate coefficient $k = -4.42 \times 10^{-4}$ s^{-1}, a full order of magnitude faster than the previous estimate. Based on the sensitivity of the rate coefficient, much care should be made when estimating plume speed for flux calculations.

In summation, several challenges for estimating sulfur dioxide to sulfate aerosol conversion rates were highlighted during the virtual field experiment. The observing strategy involved side scans of the volcanic plume or simulated transects below the plume using sun photometers, lidars, and FLYSPEC's, however this would require rotating motors for both the FLYSPEC and lidars while the sun photometer cannot be operated in such a mode. The possibility of the simulated transects below the plume is severely limited by infrastructure and complex terrain. Estimating fluxes at sites separated by a 22 km distance were particularly challenging because of plume dispersion and estimation of plume speed. Over such a distance, plume

dispersion can occur between observing sites that cannot be accounted for by using a scanning or transect sampling method. Given the lack of plume-level wind speeds, estimating plume speeds is a large source of uncertainty for estimating conversion rates. Over large distances, the assumption of a constant plume speed does not necessarily hold. Good estimates of plume speed are necessary to reduce uncertainty of conversion rate estimates.

3.3 Field Experiment

A field experiment was conducted between the 7th and 15th of July 2015 to improve our understanding of the sulfur dioxide to sulfate aerosol conversion rate around Kīlauea Volcano, Hawai'i. To address the challenges posed during the virtual field experiment a new sampling strategy was applied for the field experiment. Measurements would be taken from stationary points below the plume in order to collect a large amount of data over short periods of time with favorable environmental conditions. SO_2 and SO_4 fluxes were then estimated and used as a ratio to determine conversion rates between sites. This method implicitly accounted for dispersion.

Measurements were made only on days when there were clear skies near Halema'uma'u Crater. These days were also dominated by northeast trade winds (between 30-60°) near the crater and relatively clear skies downwind. Situating observation locations near other stations measuring surface winds is also important for estimating plume translation speeds. Given that the plume tends to propagate along the terrain, surface wind data provide the best approximation for estimating plume speeds over long distances.

Three instruments were deployed at two locations downwind of Halemaʻumaʻu Crater on July 9th, 10th, and 14th, 2015 to observe the plume (Figure 7). A FLYSPEC was used to determine the SO_2 load of the plume. A simple 2-channel GLOBE sun-photometer was used to measure the aerosol optical depth (AOD) of the plume. To constrain the observations of SO_2 and AOD, a ceilometer was used to determine the depth of the plume being sampled by the FLYSPEC and sun photometer. The ceilometer also provided information on the mixing-level height (important for plume dispersion/spreading) and cloud base height. Additional meteorological, SO_2, and $PM_{2.5}$ observations were gathered from the National Park Service, Hawaiʻi Volcanoes Observatory, Hawaiʻi Department of Health (HDOH), and Weather Underground to supplement field experiment observation data.

The proximal site was collocated with FLYSPEC-0, part of the stationary FLYSPEC array at HVNP, at a distance of ~2.6 km from Halemaʻumaʻu Crater vent. The distant site was mobile but was collocated with the HDOH monitoring site in Pāhala on the 9th and 10th July to collect coincident data in a community frequently impacted by vog. The distant site on the 14th of July was located along Highway 11 just north of Pāhala where researchers witnessed the plume crossing over the highway.

3.3.1 Synoptic Conditions

Environmental conditions during the field experiment were anomalous with a number of tropical systems observed in the Central Pacific Basin throughout early July 2015 modifying the persistent northeast trade winds typical of summer in Hawaiʻi. These systems inhibited collection of data on a number of days and altered

the synoptic environment. A typical trade wind inversion was present between 2.5-3 km on July 8th before eroding on July 9th as Tropical Storm Ela approached Hawai‘i from the east. Conditions were mostly clear early on July 9th before trade cumulus began to build around noon. These clouds filled in along the slopes of Mauna Loa and by 1400 HST conditions had become mostly cloudy at both sites.

The inversion built back in on July 10th as Ela weakened to a tropical depression, however Ela transported an airmass with higher precipitable water content into the region. In the early hours of July 10th, Tropical Depression Two-C formed south of Hawai‘i and tracked west-northwest. This system, together with the decaying TC Ela to the north, weakened the pressure gradient over the Hawai‘i and reduced wind speeds. A band of clouds and precipitation associated with TD Two-C impacted the island. While the rain ceased around sunrise, a cloud band persisted along the windward coast through the day.

The movement of these storms around the islands left Hawai‘i under a ridge with weak winds and high humidity from July 11th to 13th. A small disturbance associated with the return of easterly trade winds impacted the windward coast during the morning of July 13th bringing rain and cloud cover to the Kīlauea summit area and southern windward coast. The trade wind inversion was weak and elevated over this time but began to return to typical strength between 2.5 and 3 km overnight on July 13th. Trade winds on July 14th were more easterly with lower RH in the boundary layer resulting in low cloud cover at the summit, however orographic clouds built up along the slopes of Mauna Loa and formed mostly cloudy skies in the early afternoon at the distant site.

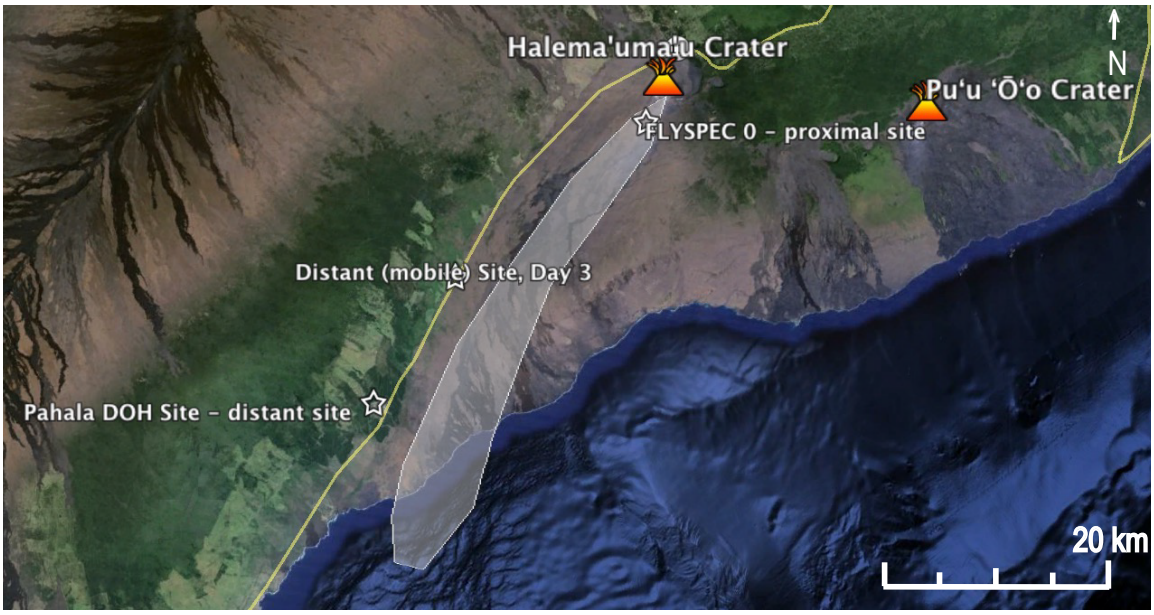

Figure 7: Map of study area. The typical plume trajectory from Halema'uma'u Crater is shown as the grey area parallel to Mamalahoa Highway (Highway 11). Measurements were collected at the proximal site which was collocated with FLYSPEC-0 of the stationary FLYSPEC array operated by HVO. The distant site was collocated in Pāhala at the Hawai'i DOH air quality monitoring site on 9-10 July. The distant site was located along Hwy 11 on 14 July.

3.3.2 Primary Instruments

3.3.2.1 FLYSPEC

Correlation spectrometers have long been used as the primary tool to monitor and measure volcanic SO_2 [Stoiber et al.,1983]. FLYSPEC, described in Horton et al. [2006], is a miniature, low-cost spectrometer that was developed as computer and electronic technology improved in the 1990's (Figure 8). FLYSPEC uses an Ocean Optics USB2000 spectrometer. A 25-micron slit provides 0.25 nm spectral resolution between the wavelengths of 177-330 nm. The instrument field of view is 44 mrad. The FLYSPEC includes three SO_2 calibration cells within each unit for concentrations of 1 ppm, 100 ppm, and 1000 ppm and a 'dark' calibration

cell. This allows calibrations to be carried out in the field and eliminates the need for further atmospheric corrections [Horten et al., 2006]. Data is then processed according to differential optical absorption spectroscopy methodology [Platt, 1994] using a dual-fit window to calculate total columnar SO_2 measurements in ppm·m. A GPS unit is integrated with each FLYSPEC. A compact laptop computer collects the FLYSPEC data and calibrations are performed automatically at the top of each hour to account for changes in solar zenith angle and cloud cover. Lapfly v5.0 software is used to operate and collect data for each FLYSPEC. Data is reported to two significant digits (0.01).

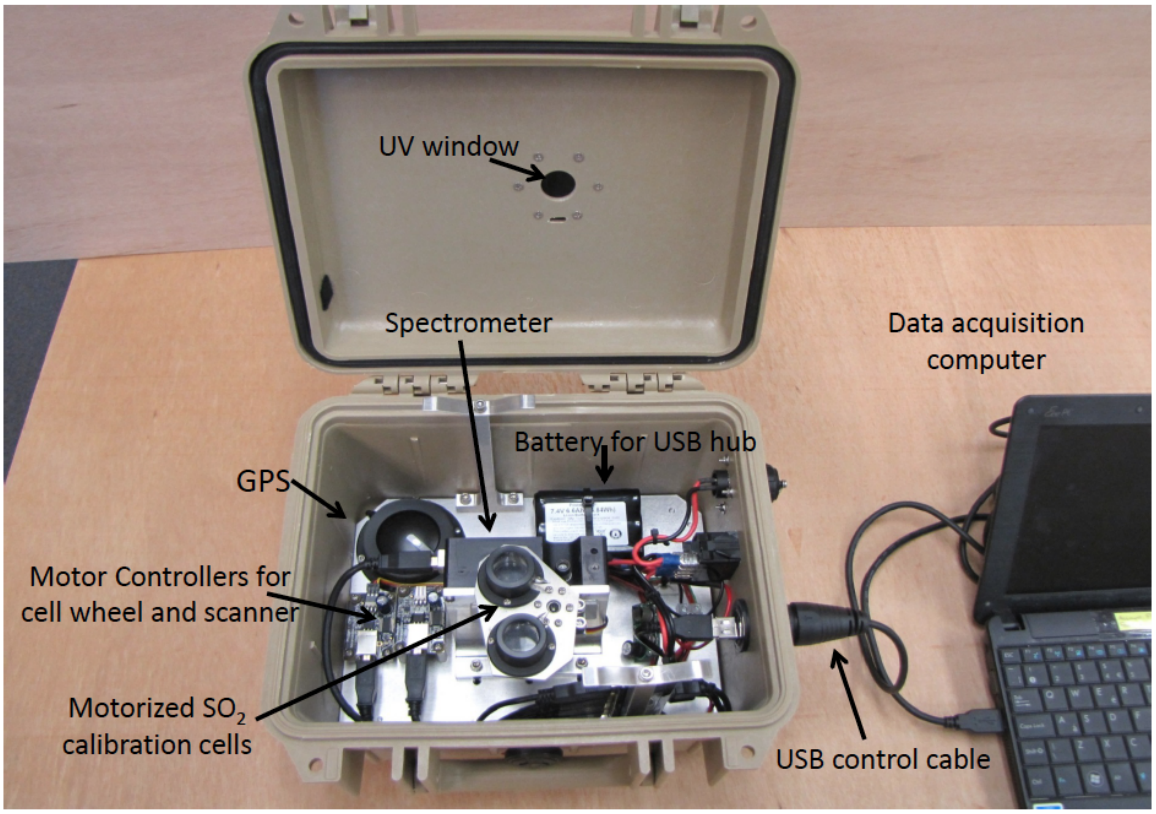

Figure 8: FLYSPEC-V3 layout and components. Used with permission from Keith Horton and FLYSPEC, Inc.

Before field experiment data collection began, the FLYSPEC GPS unit was used to get a lock on the instrument location. Prior to data collection a 'clear-sky' reference spectrum was collected for use in data processing. For the mobile site, this was done along Highway 11 while the plume was visible in the distance. A full calibration was also done at this time to ensure that the sensors did not saturate. Subsequent calibrations were done on site as sky conditions changed.

The accuracy of FLYSPEC measurements can be assessed through methods defined by the EPA in 40 CFR Part 136 Appendix B (http://www3.epa.gov/region09/qa/pdfs/40cfr136_03.pdf). The method detection limits set out by the EPA result in minimum concentration values between 3.55 and 3.80 ppm·m with 99% confidence. The SO_2 retrieval methodology is basically self-calibrating since the fit of the data being collected is against samples of known pathlength-concentrations. In terms of reproducibility, retrieved values are consistently within 2.5% of known values. Self-calibration of reference cells consistently retrieve values within 2.5% of known values.

3.3.2.2 GLOBE Sun Photometer

The GLOBE sun photometer is designed as a low cost educational tool and is described in Brooks and Mims [2001]. These sun photometers utilize LED detectors instead of narrow-bandpass filters. This reduces cost and increases the lifetime of each detector. LEDs are also very stable over time, however their spectral bandpass is large relative to standard sun photometers. Two channels are available – 505 nm (green) and 625 nm (red). Each unit has a built in digital panel meter and an internal air temperature sensor.

Calibration for a few reference instruments was completed at the Mauna Loa Observatory in June 2015, followed by Langley analysis to produce unique calibration constants (V_0) for each channel. These reference instruments were then used to transfer calibrations for other instruments. Brooks and Mims [2001] found the resulting error of transfer calibrations is on the order of 1% for V_0.

Further error analysis was performed by Boersma and Vroom [2006]. They concluded that the aerosol optical thickness (AOT) values are most sensitive to errors in V_0 and measured signal V for measurements performed during midday. Estimated errors in V are between 1-3% [Boersma and Vroom, 2006]. Systematic errors are also possible from heating of the LED detectors, which will affect instrument sensitivity. GLOBE sun photometers are designed for short-term use (< 10 min) and should be kept at room temperature (10 - 20°C). Temperature sensitivity tests with earlier instrument versions suggest that for an AOT of 0.25 the error is about 1.8%/°C [Brooks and Mims, 2001].

Boersma and Vroom [2006] have compared AOT retrievals from GLOBE instruments to more sophisticated automated sun photometers. In a side-by-side comparison they found high correlation coefficients, small biases, and root mean squared error (RMSE) below 0.12 AOT. When measurements were taken by secondary school students correlation coefficients with nearby AERONET observations were still high, but biases and RMSE were slightly higher but much of this they attributed to spatiotemporal differences in the airmass being sampled.

Data were collected manually for each sun photometer (Figure 9). Each unit was mounted on a tripod and aimed at the sun. Each channel voltage was read off

the instrument and recorded in a notebook. The internal temperature was then recorded, followed by the dark voltage reading, and the whole process was repeated each minute. Detailed notes were also taken to record instances of cloud cover or changing sky conditions.

Figure 9: GLOBE sun photometer. A toggle switch on the right-hand side allows the user to switch between the red and green channels as well as the internal temperature sensor.

3.3.2.3 Ceilometers

Two Vaisala ceilometers were utilized – the CT25K and the CL31 (Figure 10). Both ceilometers are low-energy, eye-safe lasers and are ideal for aerosol studies. Each laser pulse is reflected by aerosols and returned to the receiver providing a vertical backscatter profile. Technical specifications for both instruments can be

found in Table 1. The older CT25K provides more detailed information than the newer CL31 model. However, the CL31 can provide finer resolution data in both time and space. A single lens optics set-up provides total signal overlap allowing detection of aerosols to near 0 m AGL. The CT25K is also capable of tilting with a range of -15° to +90°.

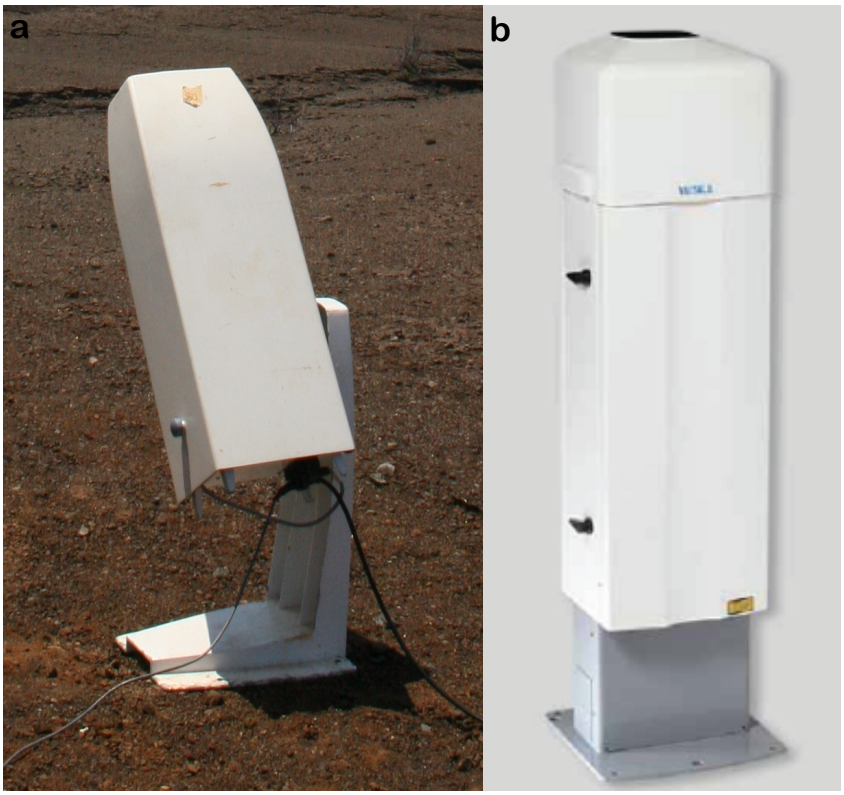

Figure 10: Vaisala CT25K (a) and CL31 (b).

Vaisala CL-VIEW software was used to collect ceilometer data. This software includes a cloud base algorithm that allows up to three distinct cloud layers to be retrieved in each profile.

Both ceilometers operate at a wavelength of 905 nm, making them well suited to observed aerosols larger than 1 μm. Sulfate aerosols are typically in the accumulation mode [Altshuller, 1982] defined by 0.1 μm < particle size < 2.5 μm.

This means that the ceilometers will only be able to detect a small fraction of sulfate aerosols present.

Table 1. Technical properties of ceilometers used during field experiment.

	CT25K	**CL31**
Measurement range (m)	0-7500	0-7500
Resolution (m)	30	5
Wavelength (nm)	905	905
Sampling Rate (s)	15	4
Repetition Rate (kHz)	5.57	10.0
Normalized Units (srad *km)$^{-1}$	10^4	10^5

3.3.3 Data Reduction Methodology

3.3.3.1 SO_2 Flux

SO_2 fluxes were calculated at site 1 based on FLYSPEC observations. Site 1 was established next to FLYSPEC-0, part of HVO's stationary FLYSPEC array (Figure 11). The FLYSPEC was vertically pointed and data was available every 10 seconds. Data at site 1 were averaged every 10 minutes based on the availability of wind data from the Sand Hill meteorological station upwind needed to calculate fluxes. Ten minutes was approximately the advective timescale [Stull, 1988] between the emission source and FLYSPEC-0. Fluxes were then calculated according to the method of Williams-Jones et al. [2008] where d_{seg} is taken as the FLYSPEC field of view at the top of the plume. SO_2 pathlength measurements were temperature and pressure corrected following Gerlach [2003] using temperature data from the Sand

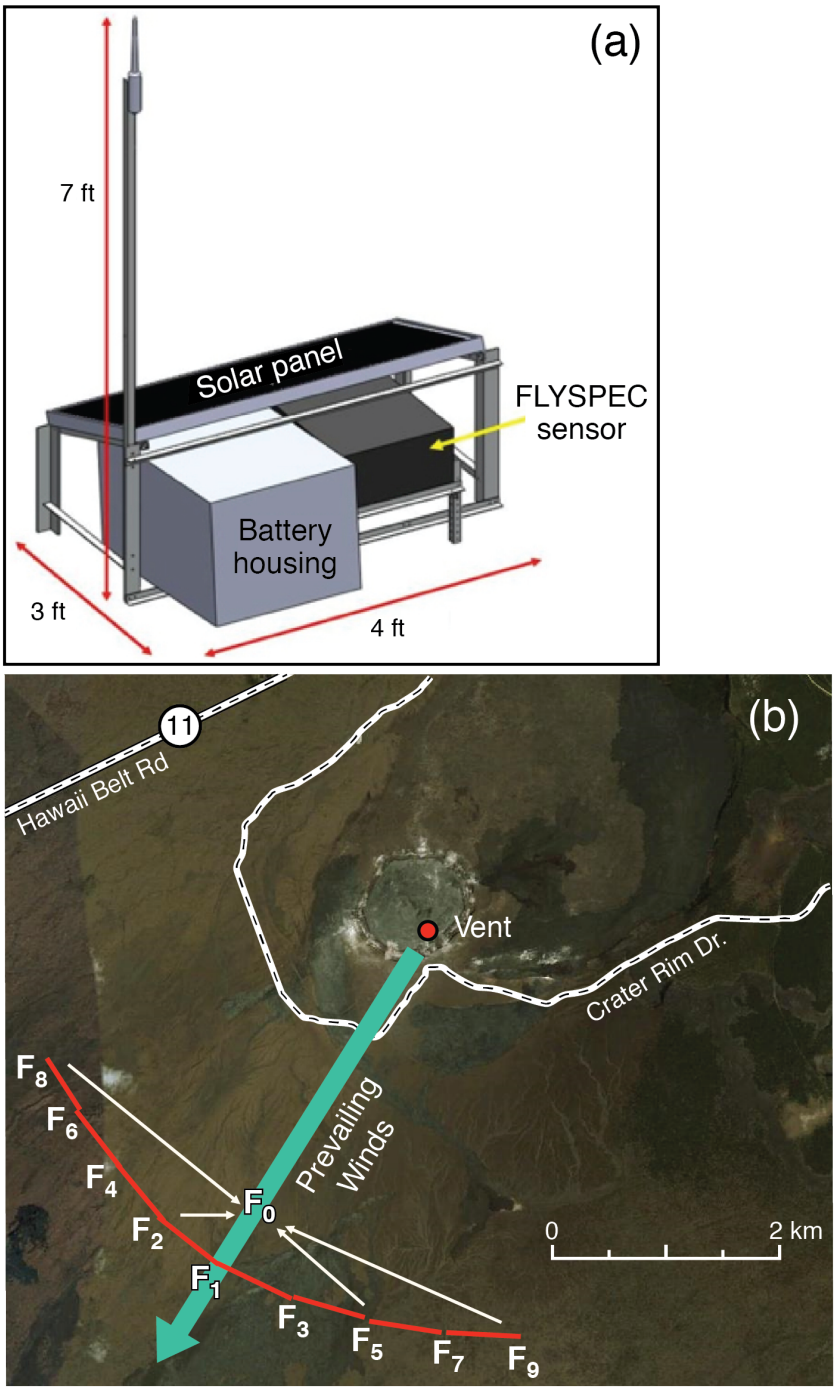

Figure 11: a) Schematic diagram of FLYSPEC instrument configuration with 160-W solar panel. FLYSPEC sensor, electronics, and computer are in the black box under the aluminum housing that supports the solar panel. Grey box contains the deep cycle battery and charge controller. b) Aerial view of approximate FLYSPEC locations for the SO_2 monitoring array. F_0 represents FLYSPEC-0, F_1 - FLYSPEC-1, and so on. Sensor array is located approximately 2.7 km from source vent at Halema‘uma‘u.

Hill meteorological station (approximately 100 m away from FLYSPEC-0) and pressure data from HVO (approximately 3 km away from FLYSPEC-0). The top of the plume was defined by the backscatter signal from the ceilometer. Ceilometer data were averaged over 10 minutes and over 60 m in the vertical. A signal greater than 700 backscatter units (bu) = $[10^4 \text{ srad*km}]^{-1}$ was used to define the plume.

3.3.3.2 SO_4 Flux

Voltages recorded from the GLOBE sun photometers first needed to be converted to AOD values. This method was developed by manufacturer Dr. David Brooks. The internal temperature was used to correct the calibration voltage for each channel according to

$$V_{green} = V_0[1 + .0009(T - 21.5)] \tag{3.6}$$

$$V_{red} = V_0[1 + .0072(T - 21.5)] \tag{3.7}$$

where T is the internal temperature. Date, time, and location information were then input to calculate solar parameters. Station pressure (mb) from HVO was used to calculate the relative airmass through which observations were taken. AOD was then calculated using

$$AOD = \frac{\ln(V_0/r_e^2) - \ln(V - V_D) - a * m * p/1013.25}{m} \tag{3.8}$$

where a is a coefficient dependent on wavelength, m is the relative airmass (approximately equal to the secant of the solar zenith angle), p is the station pressure in mb, V_D is dark voltage (dependent on wavelength), V is the solar voltage given by instrument, and r_e is the earth-sun distance in AU. Wavelength dependent

ozone corrections were then applied to each observation. Further details of this method are found in Brooks and Mims [2001].

Sulfate aerosol fluxes were calculated using the green channel only. This was done for two reasons: 1) the 505 nm channel is more sensitive to sulfates; 2) AOD calculations from the green channel are less sensitive to changes in internal temperature, i.e., equation (3.6). AOD values were then averaged over 10 minutes, similar to SO_2 values.

The sulfate aerosol flux was calculated following Porter et al. [2002] with gamma = 7.7 $m^2\ g^{-1}$. This value was high because it assumed a wetted aerosol, however Hand and Malm [2006] estimate lower mass scattering efficiencies of ammonium sulfate. For small mass size distributions they estimated gamma = 2.2 $m^2\ g^{-1}$ and for large mass size distributions 4.8 $m^2\ g^{-1}$. Given the high humidity in Hawai‘i, the higher estimate of Porter et al. [2002] was preferred. The wind speed from Sand Hill was used as the plume speed and the interval width was given by the instrument field of view (0.008 m). Flux calculations at the mobile site used wind speeds from the Pāhala DOH site on July 9th and 10th 2015, while on July 14th 2015 the Kapapala Ranch RAWS site was used due to distance from mobile site.

3.3.3.3 Plume Speed

The Halema‘uma‘u plume passed near or over the proximal site at FLYSPEC-0 on all observation days. Wind data from the Sand Hill meteorological station just upwind of FLYSPEC-0 provided reliable plume translation speed estimates when compared with plume speeds derived with the multiple-spectrometer method between FLYSPEC-0 and FLYSPEC-1 (Figure 12). Plume speeds using the multiple-

spectrometer method showed good agreement with wind speeds from the Sand Hill station, especially during July 9th.

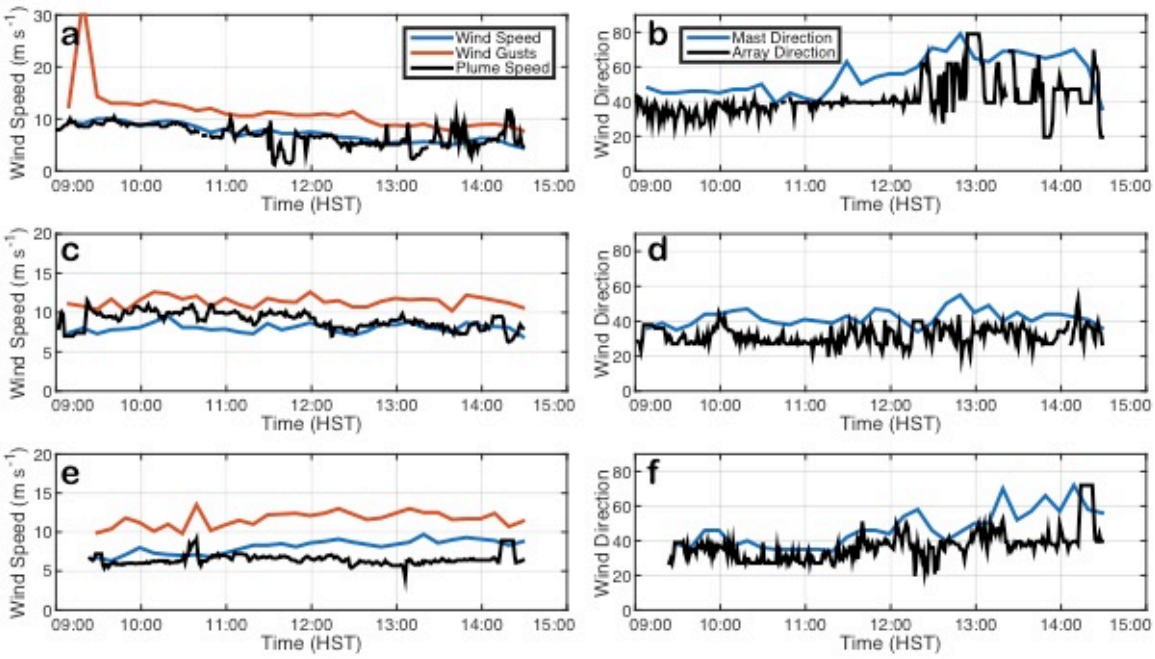

Figure 12: Wind data from the Sand Hill station just upwind from FLYSPEC-0 and plume speed and direction data calculated from the multiple-spectrometer method valid during observational periods on (a, b) 9 July 2015, (c, d) 10 July 2015, and (e, f) 14 July 2015.

Visual observations confirm the plume continued along a trajectory for some distance downwind that ran parallel to Highway 11 but did not cross it (Figure 13). Backwards trajectories from Pāhala calculated using the UH Vog Model, followed this general path suggesting the average travel time back to the Halemaʻumaʻu Crater was at least 5 hours. High-resolution WRF wind fields reveal the complex local circulation that exists in this area of Hawaiʻi (Figure 13). Trade winds existed across Kīlauea's summit, while a mountain circulation dominates in the Pāhala region, where trade winds were blocked by the Kīlauea summit. Conditions on July 10th were similar with the plume moving more easterly out over the Kaʻū desert

after passing over the proximal site. The uncertainty in plume speed between sites created uncertainty in conversion rates for these days. Also, the length of observation periods (< 5 hours) on July 9th and 10th made it unlikely that the same plume was sampled at both sites. Visual identification of the plume crossing Highway 11 on July 14th reduced uncertainty when estimating a conversion rate given the shorter plume trajectory and travel time. Forward and backward trajectories agreed that the travel time between observation sites was approximately one hour.

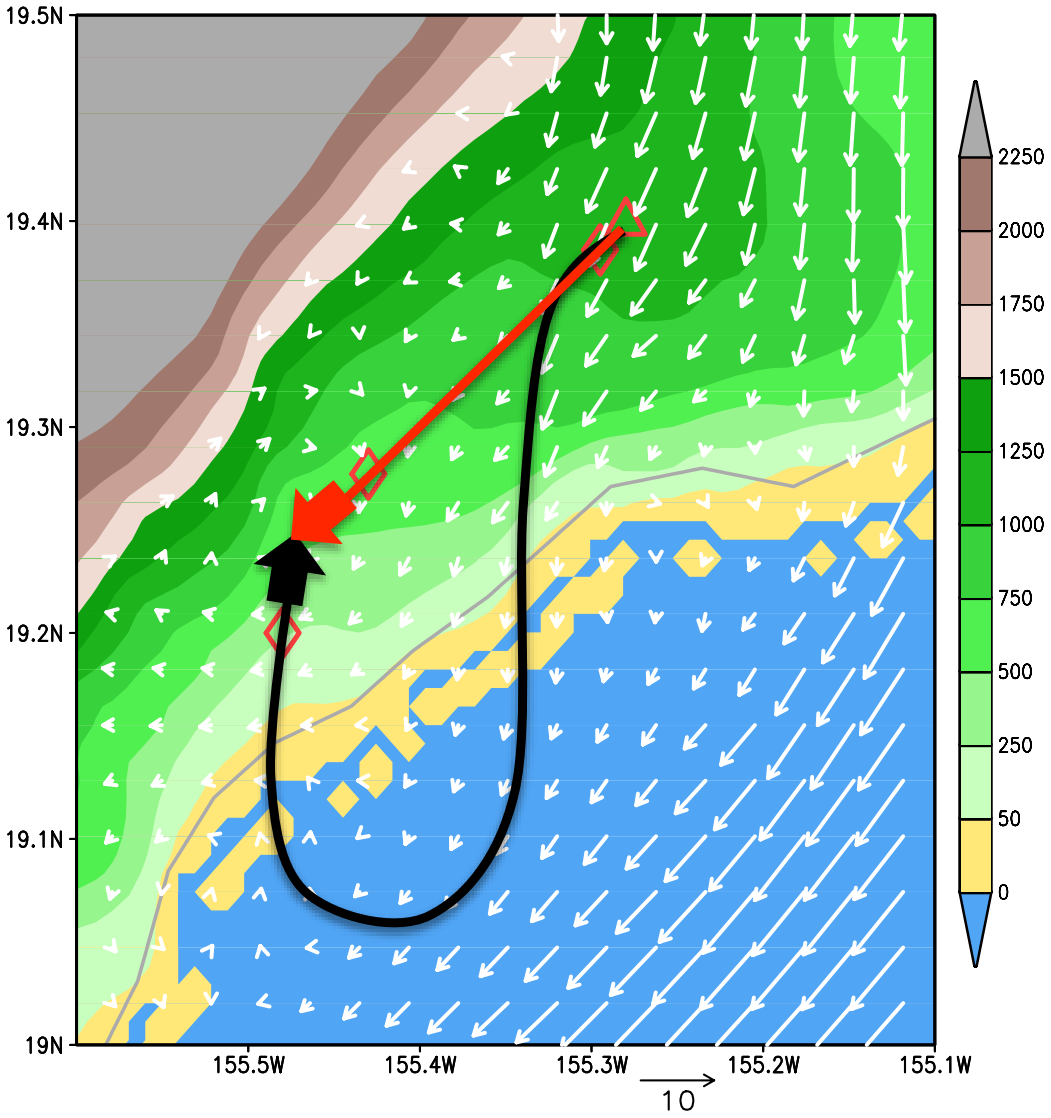

Figure 13: High-resolution WRF wind vectors valid 0900 HST 9 July 2015. Wind vectors are mean boundary layer vectors defined as winds from 0 to 2000 m MSL. The triangle represents Halema'uma'u Vent, the diamond next to it represents the proximal measurement site and the diamonds further downstream represent the distant measurement sites. On 9 and 10 July the distant site was at Pāhala and on 14 July the distant site was along Highway 11, at a point between the proximal site and Pāhala. The black trajectory based on visual observations, local wind observations, and model trajectories represents the plume path on 9 and 10 July. The red trajectory represents the plume path on 14 July. The reference vector is in m s^{-1}. Terrain contours (m) are shaded.

3.3.4 Results

SO_2 emissions from volcanoes are estimated by calculating SO_2 fluxes from observations. By taking observations at multiple points downwind of a volcano SO_2 fluxes can also be used to estimate conversion rates of SO_2 to sulfate aerosols (SO_4).

SO_2 and SO_4 fluxes (kg s^{-1}) were calculated at each measurement site for each observation day and the results are shown in figure 14. Due to cloudiness, AOD observations were not always possible, resulting in gaps in the SO_4 flux time series. There were large swings in species concentrations caused by the uneven nature of the plume passing over the proximal site. At the distant site fluxes were much lower and steady. Interestingly, raw SO_2 values measured in Pāhala were the same magnitude as those routinely measured along Chain of Craters Rd below the Pu‘u ‘Ō‘o plume (Tamar Elias and Andrew Sutton, personal communication 2015).

It can be seen that the SO_4 fluxes were consistently orders of magnitude lower than SO_2 fluxes at the proximal site. This was expected since sulfate must form from the emitted SO_2 between the source and measurement site. Fluxes generally changed in unison with the exception of cloudy periods often found at the beginning and end of each observation day. SO_2 fluxes on day two were an order of magnitude lower than on days one and three due to lower observed SO_2.

Fluxes at the distant site were steadier than the proximal site because the pollutants were well mixed in the boundary layer by this point. SO_4 fluxes were three orders of magnitude lower than SO_2 fluxes. Owing to the long trajectories estimated between sites on July 9th and 10th, much of the plume sampled at the distant site was not sampled at proximal site. Regardless, the amount of SO_4 relative

to SO_2 increased between sites. This was evident when partitioning between the two sulfur species was done via

$$f_s = [SO_4]/([SO_4] + [SO_2]) \quad (3.9)$$

where f_s is the fraction of sulfur observed as sulfate [Kroll et al., 2015]. Partitioning is shown for the three observation days in figure 15.

Owing to the large uncertainty in plume age resulting from the plume trajectory between observation sites much of the data presented was not suitable for estimating conversion rates. Long trajectories and distances between observation sites suggested that observations at the proximal site might not have been observed at site two. Kroll et al. [2015] faced a similar problem when estimating plume age during their field experiment. By allowing our distant observation site to relocate based on plume movement, visual identification of the plume allowed measurements to be obtained on July 14th 2015 with a good approximation of plume age to allow for conversion rates to be estimated. Only a limited amount of observations were suitable for analysis however, and as a result additional methods of estimating conversion rates were devised.

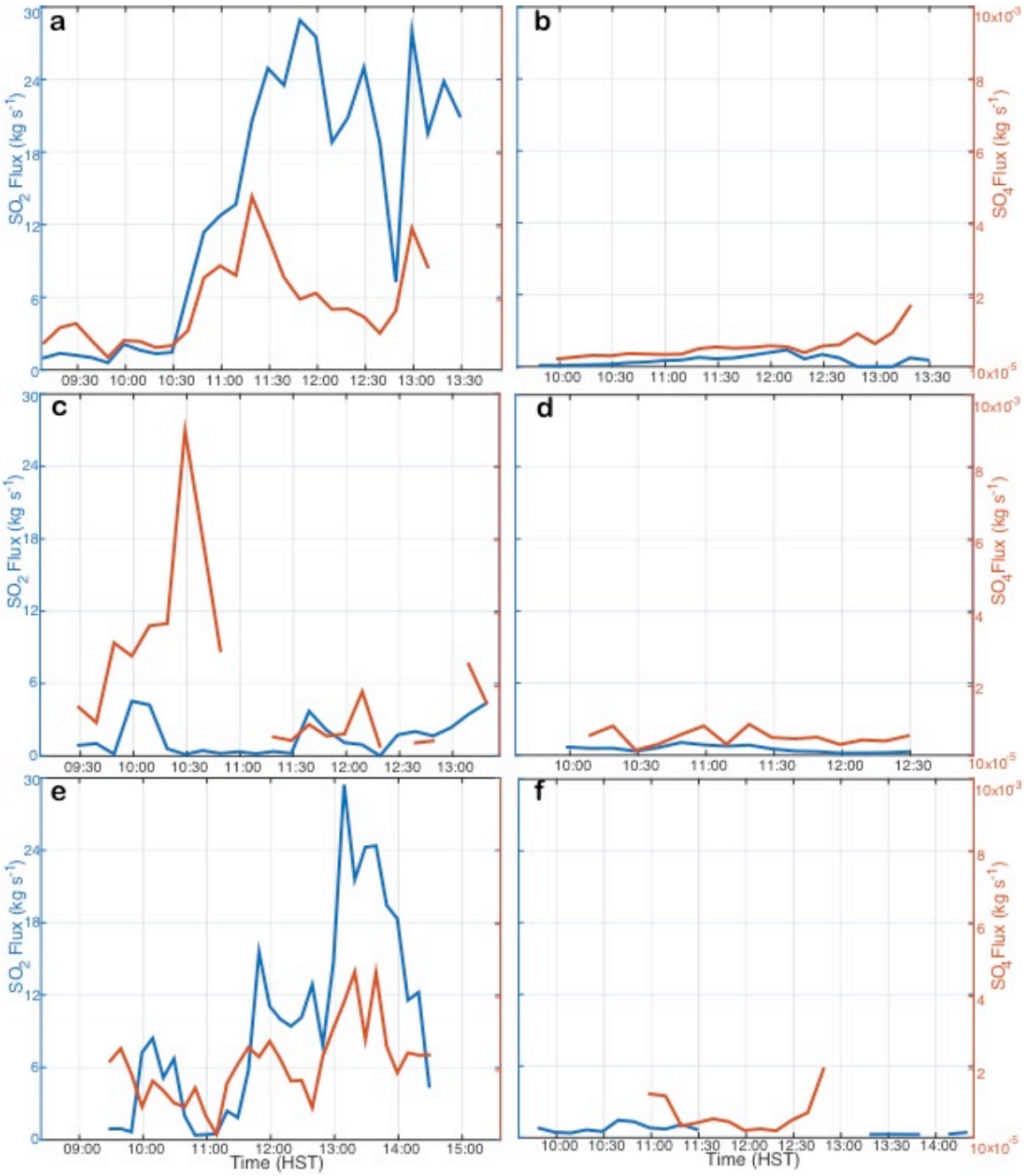

Figure 14: Time series of SO_2 and SO_4 fluxes calculated at the proximal site valid (a) 9 July, (c) 10 July, and (e) 14 July 2015. Fluxes calculated at the distant site are valid (b) 9 July, (d) 10 July, and (f) 14 July 2015. The distant site was located in Pāhala on 9 and 10 July and along Hwy 11 on 14 July.

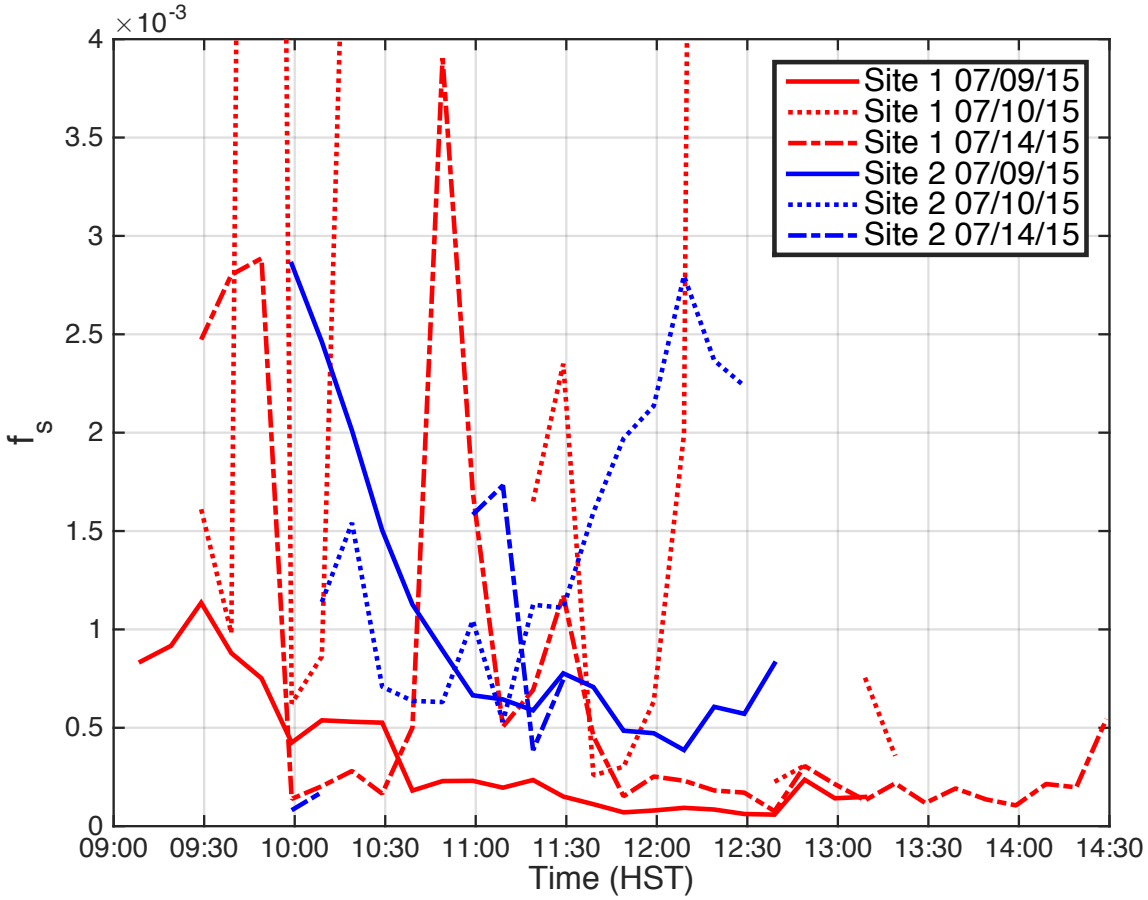

Figure 15: Fraction of sulfur observed as sulfate, f_s, derived from 10-minute averaged flux values.

Three methods for estimating conversion rate were employed. Estimating the conversion rate with the exponential decay function, equation (3.1), for both SO_2 and SO_4 fluxes was done for method one. Sulfate ratios obtained through sulfur partitioning were used with equation (3.1) for method two. The first two methods utilized data collected on July 14th 2015, when the distance travelled by the plume between observation sites was well known. Both of these methods resulted in fewer than thirty combined estimates of conversion rates making it difficult to draw any meaningful conclusions. Additionally, method one did not account for dispersion and has a larger source of uncertainty than method two. Method three was devised

to obtain many estimates of conversion rates with lower uncertainty from plume speed or plume age.

Data from the proximal site on July 9th 2015 was used in method three. Conversion rates were estimated by assuming all observed sulfate had formed in the short time between emission and observation. Since SO_4 fluxes were much less than SO_2 fluxes this conversion resulted in almost no loss in SO_2 mass flux. Thus, by taking observed SO_2 flux + observed SO_4 flux = Φ_0 and SO_2 flux = Φ conversion was estimated with equation (3.1), while also correcting for differences in molecular mass between species (ie., $[SO_4] = 1.5*[SO_2]$).

3.3.4.1 Method One

Conversion rates were calculated from observations on July 14th 2015 during a 40-minute period (between 0900 and 1130 HST) when both SO_4 and SO_2 flux data were available at both sites. The short distance between observation sites and wind observations that suggested a rather straight-line trajectory for the plume between sites, limited uncertainty in the transport time. A 50 (±10) minute transport time was used with the 10-minute averaged fluxes for estimating the conversion rate via equation (3.1). SO_2 loss rates were on the order of 4×10^{-4} s^{-1} to 7×10^{-4} s^{-1} while SO_4 production rates were on the order of 1×10^{-4} s^{-1} to 2×10^{-4} s^{-1}. SO_2 rates were more sensitive to the elapsed time while SO_4 rates were not. This was a reflection of measurement sensitivity for the observed quantities of total columnar SO_2 and AOD. Since AOD observations were not as sensitive as SO_2 observations, the method used to derive SO_4 fluxes may not be suitable for estimation of conversion rates on their own. These values imply a rapid conversion

rate (20-50% hr^{-1}) similar to those measured at Mt. Etna and Mt. Erebus involving heterogeneous and multiphase reactions [Oppenheimer et al., 1998].

These results highlighted the limitations of using remote sensing instruments to observe and estimate purely homogenous reactions in clear air. Visual observations of the plume suggested condensation of co-emitted water vapor that would allow heterogeneous reactions to occur and account for these large loss/production rates, however a major limitation for this method is that horizontal dispersion of the plume was not taken into account and could be attributed to a significant fraction of the change in fluxes seen between sites.

3.3.4.2 Method Two

To account for dispersion of the plume, sulfur partitioning of fluxes was performed and conversion rates were estimated from changes in sulfate fraction between sites. Data from July 14th 2015 (Figure 15) were used for this method over the same 40-minute period as in method one. Using equation (3.1) and taking $\Phi = SO_2/(1 - f_s)$ at both sites, the conversion rate was calculated based on SO_2 loss. Estimates ranged from $k = 7.3 \times 10^{-8}\ s^{-1}$ to $6.1 \times 10^{-7}\ s^{-1}$, which correspond to very slow reaction rates on the order of .03% h^{-1} to .22% h^{-1}.

Rates of this magnitude were reported only for the eruptions of Mt. Pinatubo in 1991 and Mt. St. Helen in 1981 [Read et al., 1993; Hobbs et al., 1982], however estimates from Mt Pinatubo were made in the stratosphere while the estimates from Mt St. Helen were from the troposphere and boundary layer. Such slow conversion rates estimated here could have resulted from depletion of reactants inside the plume combined with minimal mixing between the plume and the environment.

Using method two to take into account dispersion highlighted that there may be greater uncertainty in the plume speed than originally thought. The distance between observation sites was 18 to 20 km and the impact of the complex terrain on the plume speed between the sites was unknown. Surface station wind data displayed wind speeds near the proximal site at the summit of Kīlauea between 6 – 10 m s^{-1} from the northeast (32 – 72°) while wind speeds near the distant site were between 2 – 3 m s^{-1} from the east-southeast (116 – 158°), suggesting the plume may have decelerated and turned sharply from a southerly trajectory to a more northerly one between observation sites. A further estimate of conversion rates over a shorter distance with a relatively steady wind field was sought to further reduce uncertainty in conversion rates by constraining estimates of plume speed.

3.3.4.3 Method Three

In light of the limited amount of estimated conversion rates provided by the previous methods and the limitations of the data and methods used in the calculations, another approach was taken to estimate environmental conversion rates at the proximal site. For this method, one-minute fluxes of SO_2 and SO_4 were calculated from data collected on July 9th 2015 using the methodology described previously. This day represented the most ideal conditions regarding consistent trade winds and low cloud cover. One-minute fluxes were used because the region being considered was the summit area, and correlations between surface wind speeds and dual-spectrometer plume speeds (available every minute) were high (Figure 12), providing good estimates of plume speed over a 2 – 3 km distance.

Periods when both fluxes were present were then used to calculate sulfate ratios via sulfur partitioning.

The flux of SO_4 followed the SO_2 flux closely, especially early in the period when fluxes were low (Figure 16). Then both SO_2 and SO_4 fluxes increased dramatically at 1030 HST. The increase in fluxes were a result of a three-fold increase in emissions estimated by both the FLYSPEC array and real-time seismic amplitude (RSAM) network, which show a strong correlation as RSAM measurements relate to gas movement in the magma chamber [Elias and Sutton, 2012].

It was clear from sulfur partitioning that as the amount of SO_2 detected increased, SO_4 did not rise proportionally (Figure 17). Initially the fraction of SO_4 to SO_2 was relatively high, at $SO_4/SO_2 \geq 10^{-4}$, but then decreased when SO_2 emissions increased at 1030 HST, $SO_4/SO_2 \leq 10^{-5}$. Based on theoretical calculations, this made sense because the limiting agent in the reaction was not SO_2 but the hydroxyl radical. An upper bound on sulfate formation via the OH pathway was reached after SO_2 emissions increased dramatically, which pushed down sulfate fractions.

The sulfate fractions reflected theoretical values from gas phase reactions over relatively short time periods. Given that sulfate fluxes were several orders of magnitude smaller than SO_2 fluxes, the partitioned values could be considered as SO_2 loss between the source and observation site. The conversion rate could be solved using equation (3.1) by taking Φ_0 = SO_2 flux + SO_4 flux observed at the proximal site and Φ = SO_2 flux while also correcting for differences in molecular mass between species (i.e., $[SO_4] = 1.5*[SO_2]$). Reaction rates fluctuated between 0

and 3 % h^{-1} (k = 3.4 x 10^{-9} – 6.7 x 10^{-6} s^{-1}), but when SO_2 fluxes increased over 5.0 kg s^{-1}, the reaction rate fell below 0.5 % h^{-1} (Figure 18). The conversion rates before 1030 HST were similar to the theoretical calculations made during the daytime. When emissions increased and reaction rates fell below 0.5 % the rates resembled the lower conversion rates during nighttime when reactions were limited due to OH concentrations.

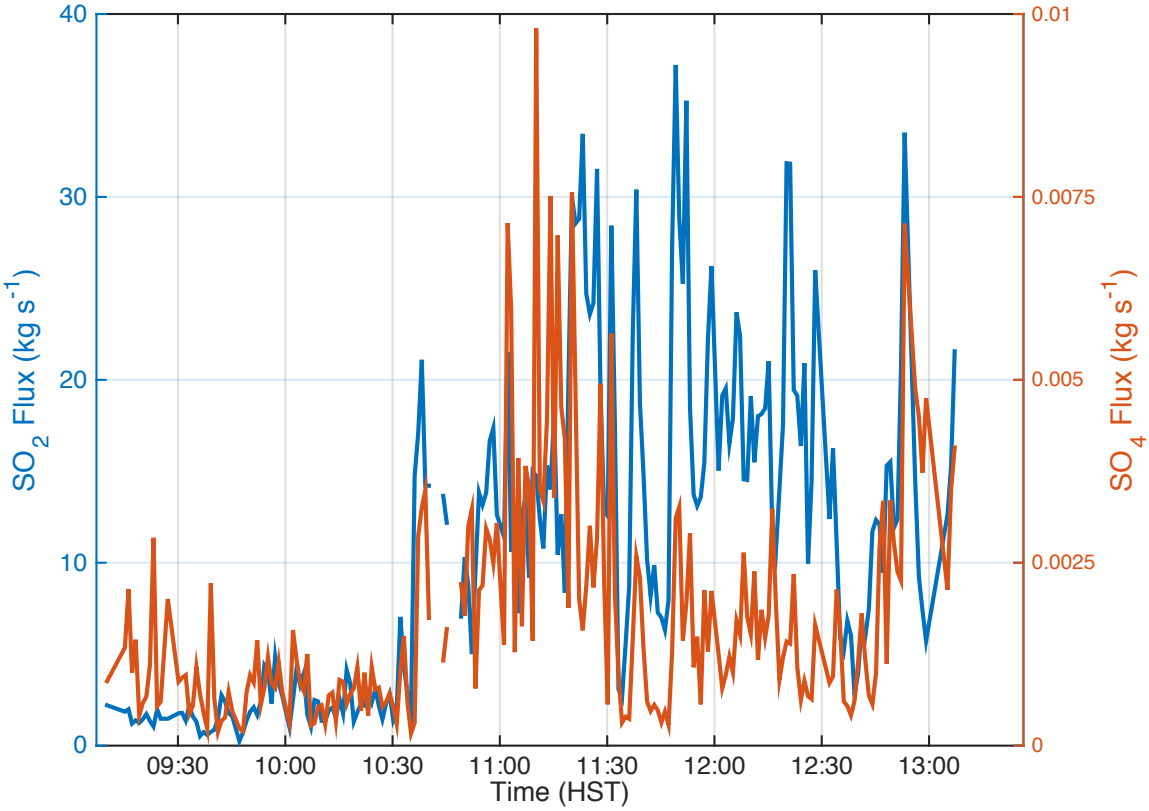

Figure 16: 1-minute averaged SO_2 and SO_4 fluxes (kg s^{-1}) calculated at site 1 on 9 July 2015.

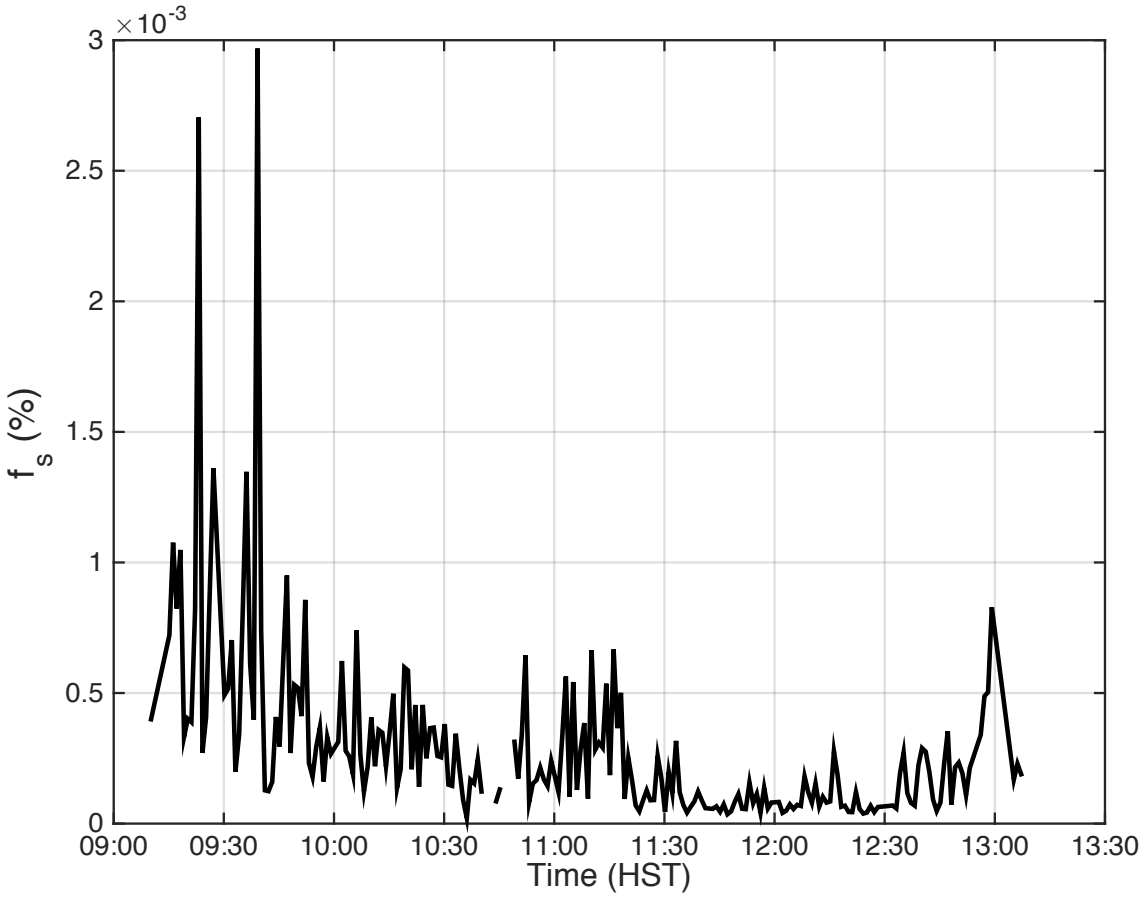

Figure 17: Sulfate fraction (f_s) calculated from SO_2 and SO_4 (c.f. Figure 10) at site 1 on 9 July 2015.

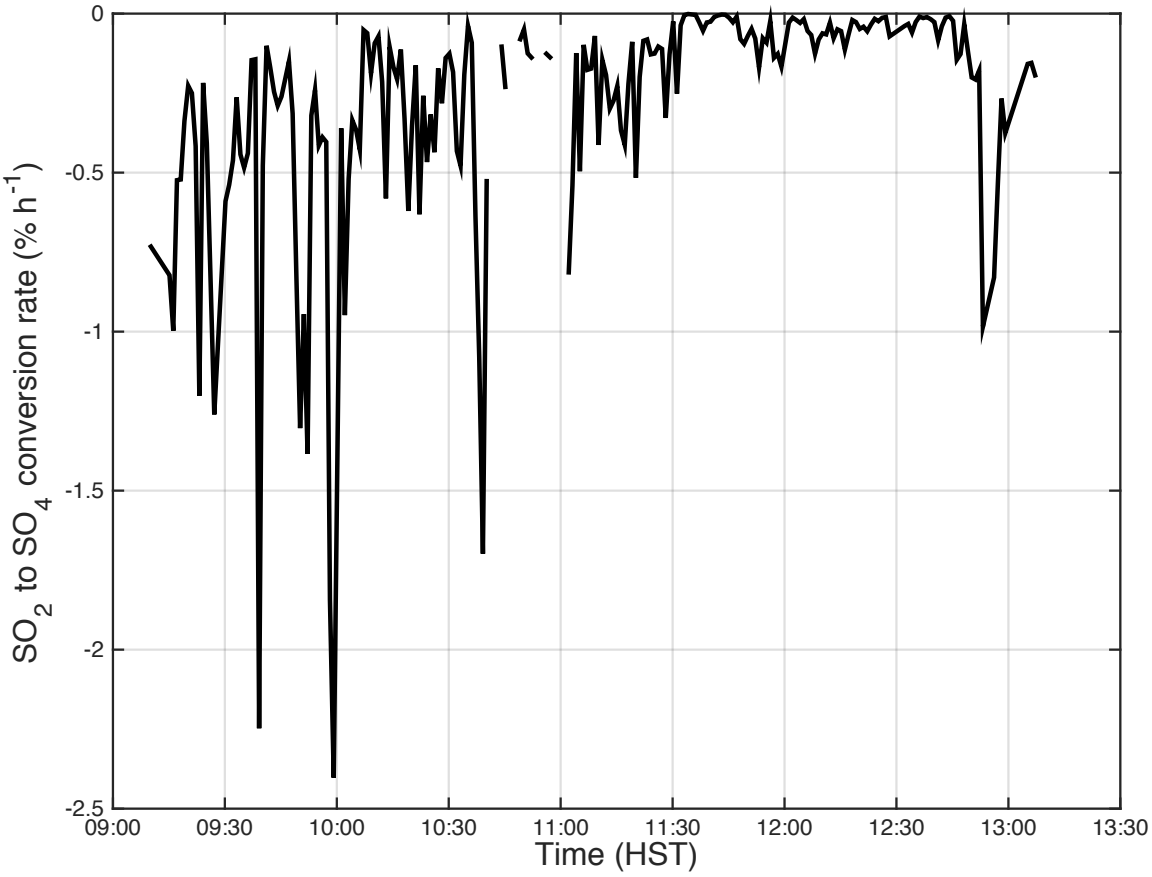

Figure 18: SO_2 to $S0_4$ conversion rates (% h^{-1}) estimated from observations on 9 July 2015.

3.4 Conclusions

To estimate environmental conversion rates of sulfur dioxide to sulfate aerosols at Kīlauea Volcano, both a virtual field experiment and a field experiment were conducted. Measurements of sulfur dioxide, aerosol optical depth, and plume depth were made simultaneously at two sites downwind of Halemaʻumaʻu Crater and provided information on the composition and evolution of the plume. Estimating conversion rates between these sites was made difficult due to:

1) long plume trajectories resulting in advection times greater than observation periods,
2) cloud cover,

3) plume dispersion, and
4) complex wind fields downwind of the volcano.

Three methods for estimating conversion rates were used, where each successive method reduced uncertainty in the previous method. Detailed observations near the vent during ideal conditions on July 9th 2015 provided the best estimates of sulfur dioxide conversion rates in clear air.

A virtual field experiment was conducted during February 2015 to test the proposed sampling strategy and methodology for estimating conversion rates. Results suggested that the proposed sampling strategy, conducting scans or transects of the plume, was impossible given limitations of both infrastructure and instrumentation. The standard method for estimating conversion rates using an exponential decay function resulted in overestimates of conversion rates. Possible sources of error for conversion rates included:

1) plume dispersion,
2) dry deposition of SO_2 and SO_4, and
3) estimates of plume speed.

Dry deposition was quickly discounted as a major sink when total modeled deposition amounted to approximately 0.2% of total SO_2 emissions. Nadau [2006] also discounted dry deposition as a major SO_2 sink and capped it at 5% of total SO_2 loss. While it was difficult to account for dispersion, estimates of conversion rates were found to be very sensitive to assumed plume speeds.

Given the results of the virtual field experiment a new sampling strategy was proposed for the field experiment conducted in July 2015. Stationary

measurements from below the plume were taken at two sites downwind during three observing periods. Fluxes of sulfur dioxide and sulfate aerosol were estimated from observations and conversion rates were estimated using three methods. Plume trajectories during two observing periods provided a level of uncertainty that was deemed unsuitable for estimating conversion rates between observing sites.

Conversion rates were estimated with two different methods using data from a short time-window during one observing period. The first method estimated conversion rates from fluxes and found conversion rates were very high and could be due to not taking into account dispersion (Table 2). Using a second method, the ratio of SO_4/SO_2 flux at both sites was used to estimate conversion rates. This implicitly accounted for dispersion. Conversion rates were very slow, which suggested that gas phase conversion was taking place but was somehow being limited. Due to the complex wind field during this observing period there was uncertainty in the plume speed that may have influenced the estimated conversion rates. Another method for calculating conversion rates from data collected near the vent was used to reduce this uncertainty. Estimated conversion rates using this method reflected values proposed by theoretical calculations for SO_2 oxidation by OH, but also suggested that the conversion rate was being limited by high concentrations of SO_2 emissions that depleted OH faster than it could be produced.

Table 2. SO_2 to SO_4 environmental conversion rates at Kīlauea Volcano estimated from measurements collected during 2015 field experiment.

Method	Conversion Rate, k (s^{-1})	Conversion Rate, % h^{-1}
1	$4 \times 10^{-4} - 7 \times 10^{-4}$	20 – 50
2	$7.3 \times 10^{-8} - 6.1 \times 10^{-7}$	.03 – .22
3	$3.4 \times 10^{-9} - 6.7 \times 10^{-6}$	.001 – 2.4

The findings of this field experiment support the assertion that gas phase oxidation of sulfur dioxide was important for the formation of sulfate aerosol near Kīlauea Volcano. Although estimating the environmental conversion rate was challenging due to prevailing conditions and sensor placement, best estimates suggested the rate was close to theoretical values for conversion via OH. Estimates also suggested the rate was limited when high concentrations of SO_2 were observed which would have depleted OH concentrations faster than they could be produced.

Observations from all days suggest that a minimum, background concentration of sulfate aerosol is present near the vent. If we consider this relative to the observed SO_2, this background sulfate concentration represents .01% of SO_2. This value is much lower than the 1% of SO_2 as 'primary sulfate' estimated by Mather et al. [2013]. Given SO_2 emission rates of thousands of tons per day, such a small fraction of primary sulfate is non-trivial and will need to be accounted for in any numerical dispersion model.

CHAPTER 4. A NEW SULFUR CHEMISTRY SCHEME FOR THE UNIVERSITY OF HAWAIʻI VOG MODEL

4.1 Introduction

The UH Vog Model forecasts near ground concentrations of both SO_2 and SO_4 to help mitigate the health impacts of vog, such as respiratory ailments and skin irritation. Air quality monitoring data from the island of Hawaiʻi shows that instances of SO_4 pollution (defined by EPA $PM_{2.5}$ 24-hour breakpoints) increase as one travels downwind of Kīlauea while instances of SO_2 pollution (defined by DOH SO_2 hourly breakpoints) decrease simultaneously (See Appendix). This suggests that the conversion of SO_2 to SO_4 is an important process to represent in the University of Hawaiʻi (UH) Vog Model. However the conversion of SO_2 to SO_4 remains a major source of forecast uncertainty in the system. The ultimate goal of the evaluation is to determine which of the model configurations would be reliable enough to continue to develop into a product that can be used to issue statements, watches, and warnings for poor air quality similar to statements issued by NOAA agencies that are readily picked up by news outlets or other (i.e., National Weather Service statements regarding severe weather or tropical storms).

The UH Vog Model produces forecasts twice daily for near ground SO_2 and SO_4 concentrations (http://weather.hawaii.edu/vmap/hysplit/). The Vog Model is a customized version of the Hybrid Single Particle Lagrangian Trajectory (HYSPLIT) model [Draxler and Hess 1997, 1998]. The forecast region extends over the state of Hawaiʻi with a 1-km grid and utilizes meteorological forcing from the Mauna Kea Weather Center (MKWC) Weather Research and Forecasting (WRF) model.

Forecasts extend out to 59 hours. SO_2 emissions to initialize the model are provided from the Hawai‘i Volcanoes Observatory (HVO). The SO_2 source term remains the largest source of uncertainty in the modeling system, however there is no proven method for forecasting future emission rates especially on timescales of hours to days. Emission sources are represented as vertically tilted plumes from 50 m to 700 m (AGL). The tilt represents shear during typically trade wind conditions. Initialization of the plume in this manner provides another major source of uncertainty in the model, which becomes an error source during periods of non-trade wind flow. The conversion of SO_2 to SO_4 is represented by a constant conversion rate of 1% per hour. This value was lowered from 10% per hour in the initial iteration of the Vog Model because it lacked any physical basis. Another large source of uncertainty is in the meteorological fields forcing the dispersion model, especially wind fields [Pattantyus and Businger, 2015]. Uncertainty in the meteorological fields included physics parameterizations or simplifications, numeric schemes, and model initial conditions.

Recent observations suggest that during the day, gas phase conversion involving the hydroxyl radical, OH dominated conversion. A new sulfur conversion scheme based on the chemical kinetics of this reaction was created and compared with existing chemistry options in the UH Vog Model. Although this scheme was limited by the absence of nocturnal observations and subsequent estimates of conversion rates, there was expectation based on theory that minimal gas phase conversion was taking place overnight. The results of this model evaluation showed

improved forecast detection of high concentrations of both SO_2 and SO_4 with the new chemistry scheme.

4.2 Model Chemistry Background

Sulfur chemistry options were available through HYSPLIT v4 for use in the UH Vog Model. The operational UH Vog Model used a simple approach to convert SO_2 to SO_4 at a constant rate of 1% per hour and adjusts the mass of SO_4 according to the relative change in molecular mass between the two species ($[SO_4] = 1.5*[SO_2]$). Rolph et al. [1992, 1993] developed a comprehensive sulfur chemistry module for use in HYSPLIT as part of the Across North America Tracer Experiments (ANATEX). This scheme accounted for both gas and aqueous phase conversion of SO_2 to SO_4, but was not used in Hawai'i operationally due to computational inefficiencies - the complex sulfur chemistry model can be run on only one meteorological domain at a time. This scheme limited the ability of the Vog Model to forecast over larger domains while retaining the benefits of finer grids that exist as inner nests. Although the model could use course input grids to interpolate output concentration data to finer grids there was a loss of information as the scale of the forcing data and underlying topography becomes larger. In addition the routine required three chemical species to be specified, sulfur dioxide (SO_2), sulfate (SO_4), and wetted sulfate (SO_4[aq]), which increased the computational load for the model.

The gas-phase pathway in the scheme of Rolph et al. [1992, 1993] reflects the loss of SO_2 via the hydroxyl radical, OH. This is a photolytic reaction with a strong diurnal cycle. The conversion rates (fractional percent/hr) are prescribed prior to execution of the model. Separate rates are defined for the daytime and nighttime,

where daylight is defined by incoming shortwave radiation from input model data. The daytime rate is then corrected for latitude and time of day via solar sun angle (SSA) calculations at each grid.

The aqueous-phase pathway in the scheme of Rolph et al. [1992, 1993] reflects the loss of SO_2 via hydrogen peroxide, H_2O_2. Several parameters need to be prescribed for this conversion pathway including, the H_2O_2 concentration (ppb), the minimum relative humidity (RH) for wet (in-cloud) oxidation to occur, the fraction of SO_4 activated in-cloud, and cloud liquid water content (LWC). The H_2O_2 concentration is adjusted by SSA calculations to account for latitudinal dependence of H_2O_2 concentrations observed by Barth et al. [1989] and Van Valin et al. [1987]. Barth et al. [1989] also found the aqueous-phase H_2O_2 concentrations were below those expected based on Henry's Law and were related to SO_2 concentrations. Based on this finding the aqueous-phase rate constant, k_w, is a function of H_2O_2 concentration, SO_2 concentration, and LWC. A later update to the code allowed for dynamic LWC values to be calculated from WRF input data (Ariel Stein, personal communication 2014). This scheme, while simple, was effective for course grids (~200 km) and time-steps (6 hr) [Rolph et al. 1992, 1993].

4.3 Constructing a New Sulfur Dioxide Chemistry Scheme

A new gas-phase conversion scheme was written following the chemical kinetics for conversion of SO_2 to SO_4 via reaction with OH following equation (2.4). In order to perform this calculation, some concentration of OH was necessary to specify. Measured OH concentrations from the Pacific Ocean Basin collected during PEM Tropics B (1999) and INTEX-B (2006) were used to construct a diurnal range

of OH concentrations for Hawai'i (Figure 19, Table 3). Data in figure 19 showed that OH concentrations peaked around noon local time regardless of altitude and decreased to minimum values overnight. Since most SO_2 emissions from Kīlauea have been trapped below the trade wind inversion (between 1.5 and 2.5 km), values gathered much higher than this level can be removed. By binning the OH data collected below 3 km altitude by hour a look-up table of expected OH concentrations was constructed for Hawai'i (Table 3). Values peaked before noon (5.55×10^6 molecules cm^{-3}) and a minimum was reached after midnight (1.59×10^5 molecules cm^{-3}). Some interpolation was necessary to fill data gaps and to smooth the curve.

Temperature and relative humidity data from the meteorological model (WRF) were pulled into the module to calculate the rate coefficient, *k*. This was done following equations (2.5) and (2.6). Prior to solving these equations, the meteorological data was first used to calculate the dewpoint temperature (T_D) and the reference T_D (RH = 50%) at each point according to the Clausius-Clapyron Equation that also includes the August- Roche-Magnus formula [Alduchov and Eskridge, 1996] for the temperature dependence of the saturation vapor pressure

$$T_D = 243.04 * \left(\ln\frac{RH}{100} + \left(\frac{17.625 * T}{243.04 + T}\right) / (17.625 - \ln\frac{RH}{100} - \left(\frac{17.625 * T}{243.04 + T}\right))\right) \quad (4.1)$$

The rate coefficient, *k*, was then found via a modified version of equation (2.5)

$$k = A * e^{(T_{Dref} - T_D)} * 0.452C^{-1} - e^{k_1}. \quad (4.2)$$

Where k_1 is from equation (2.6), and A is a scaling factor = 1×10^{-12}.

These *k* values are fed into the existing sulfur module structure of Rolph et al. [1992, 1993] to solve for SO_2 to SO_4 conversion. The existing structure solves for the fraction of SO_2 (fSO_2) remaining after conversion

$$fSO_2 = e^{(-k*t)}. \quad (4.3)$$

The new scheme adds only a bit of complexity to this equation while producing similar results

$$fSO_2 = e^{(-k*OH*t)}. \quad (4.4)$$

Table 3: Mean OH concentrations (10^3 molecules cm^{-3}) derived from INTEX-B and PEM Tropics B measurements for each hour (HST). OH final, represents the values used in the new sulfur chemistry module. Hours with no data are filled with a dash.

Hour (HST)	OH (All)	OH (< 3 km)	OH Final
0	308	159	159
1	272	258	159
2	357	337	159
3	590	–	159
4	242	249	159
5	520	255	214
6	822	269	269
7	1491	758	758
8	3188	2138	2140
9	3450	3270	3270
10	4290	4850	4850
11	5740	5550	5550
12	5550	5440	5440
13	4980	4470	5060
14	5040	4670	4670
15	3220	3200	3200
16	1720	1680	1680
17	820	690	694
18	428	503	503
19	448	486	422
20	300	342	300
21	291	–	291
22	282	–	255
23	430	–	159

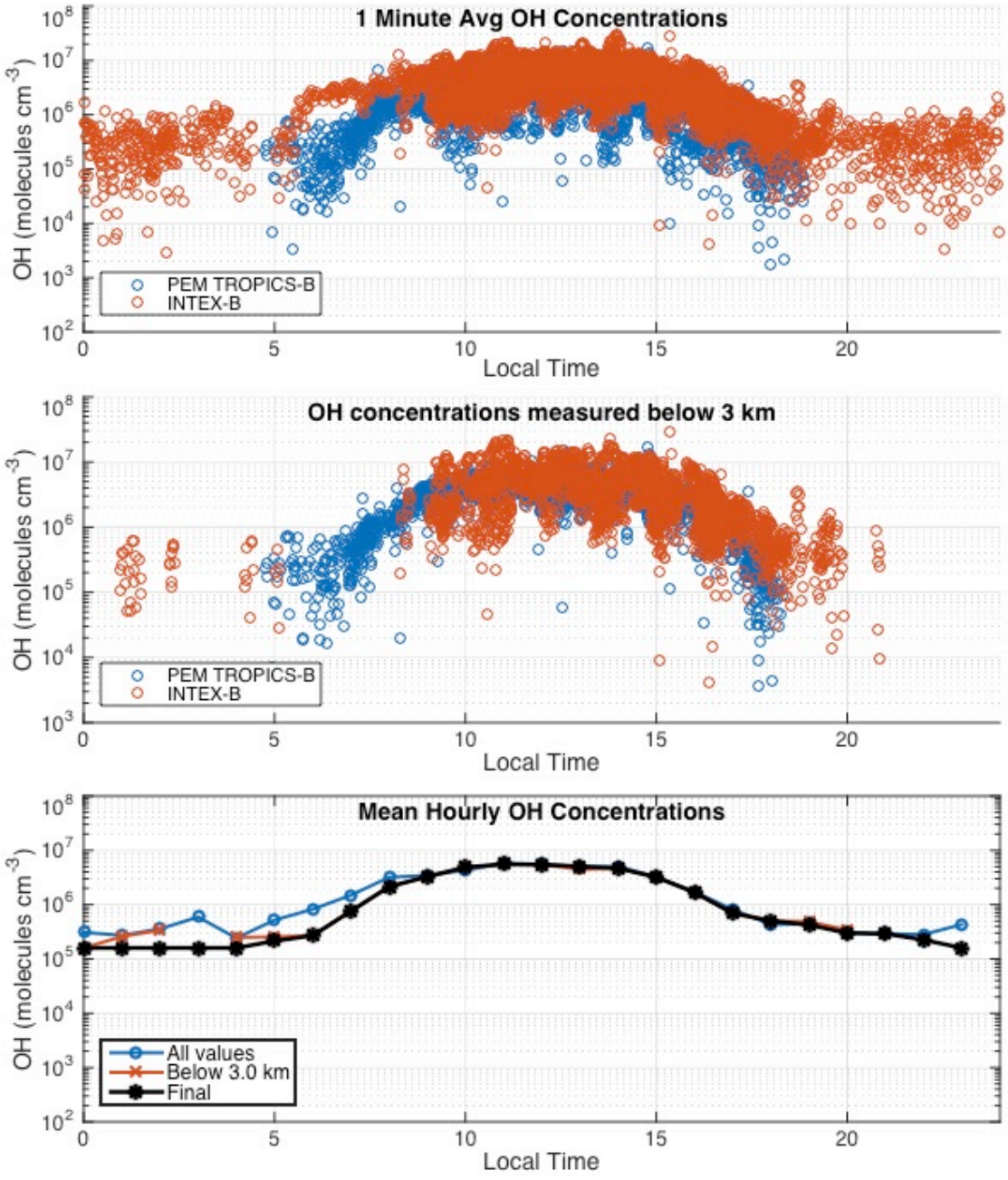

Figure 19: 1-Minute averaged OH concentrations (molecules cm^{-3}) from INTEX-B (2006) and PEM Tropics B (1999) taken across the Pacific Ocean from the surface to 12 km altitude (a), from the surface to 3.0 km altitude (b), and the mean OH concentrations by hour (Local Time) for all observations (c). Data are plotted using a logarithmic scale on the y-axis. The black line in (c) represents the values used for the new sulfur module, which are similar to the mean values below 3.0 km but with some smoothing and interpolating to fill gaps in the data.

4.4 Results

4.4.1 Comparison with Field Measurements

This routine was first tested with the observations from the proximal site on July 9th 2015. Modeled SO_2 fluxes were calculated using observed SO_2 fluxes multiplied by the fraction of SO_2 remaining after conversion calculated from equation (4.4). The amount of sulfate aerosols produced after conversion were estimated as SO_4 flux = $1.5 \cdot (1 - f_{SO_2} \cdot SO_2$ flux), where the 1.5 factor is taking into account the difference in molecular mass between SO_2 and SO_4. The time over which the conversion took place was estimated from the vent to FLYSPEC-0 distance (~2.6 km) and FLYSPEC derived plume speed data. Figure 20 suggested this scheme worked well until 1030 HST when SO_2 emissions increased sharply. Due to the increase in available SO_2 for conversion the scheme converted more to SO_4 but this was not represented by estimated SO_4 fluxes. As mentioned previously it appears the reaction was limited by OH concentrations, since they were several orders of magnitude lower than SO_2 concentrations.

Reaction kinetics suggested that OH concentrations were rapidly depleted and could not replenish as fast as they were removed through reactions with SO_2 and other trace gases. This draw down was estimated with equation (4.4) by solving for the OH concentrations given the flux values estimated from observations and time (Figure 21). Estimated OH concentrations from observations were similar to the calculated OH concentrations up until 1000 HST and then diverged. Estimated flux values suggested that corresponding OH concentrations declined by an order of magnitude from those prescribed.

OH concentrations were estimated to be many orders of magnitude lower than SO_2 concentrations in the plume and may have been depleted almost instantaneously by reaction with SO_2. Since the concentration of OH was considered stable, the formation rate can be approximated by the loss rate via carbon monoxide (CO) and methane (CH_4). CO and CH_4 would have been the leading reactants with OH in the marine boundary layer given the absence of volatile organic compound (VOC) sources upwind and concentration data for these gases were available from the INTEX-B data set. The loss/production rate was estimated via

$$\frac{d\mathrm{OH}}{dt} = -k_{CO}[\mathrm{OH}][\mathrm{CO}] - k_{CH4}[\mathrm{OH}][\mathrm{CH_4}\} \quad (4.5)$$

where [CO] is the atmospheric concentration of carbon monoxide, [CH_4] is the concentration of methane, $k_{CO} = 3.45 \times 10^{-13}$ cm^3 $molecules^{-1}$ s^{-1} [Baulch et al., 1980], and $k_{CH4} = 6.3 \times 10^{-15}$ cm^3 $molecules^{-1}$ s^{-1} [Sander et al., 2011]. The loss/production rate of OH was approximately 2×10^{-8} s^{-1} and was dominated by reactions with CO. This represented a cap on OH reactions with SO_2, which would have been reached as SO_2 concentrations approached 1×10^{14} (~10 ppm) during maximum OH concentrations. This limit remained proportional to SO_2 concentrations throughout the diurnal cycle as both OH concentrations and formation rates change in unison (Figure 22).

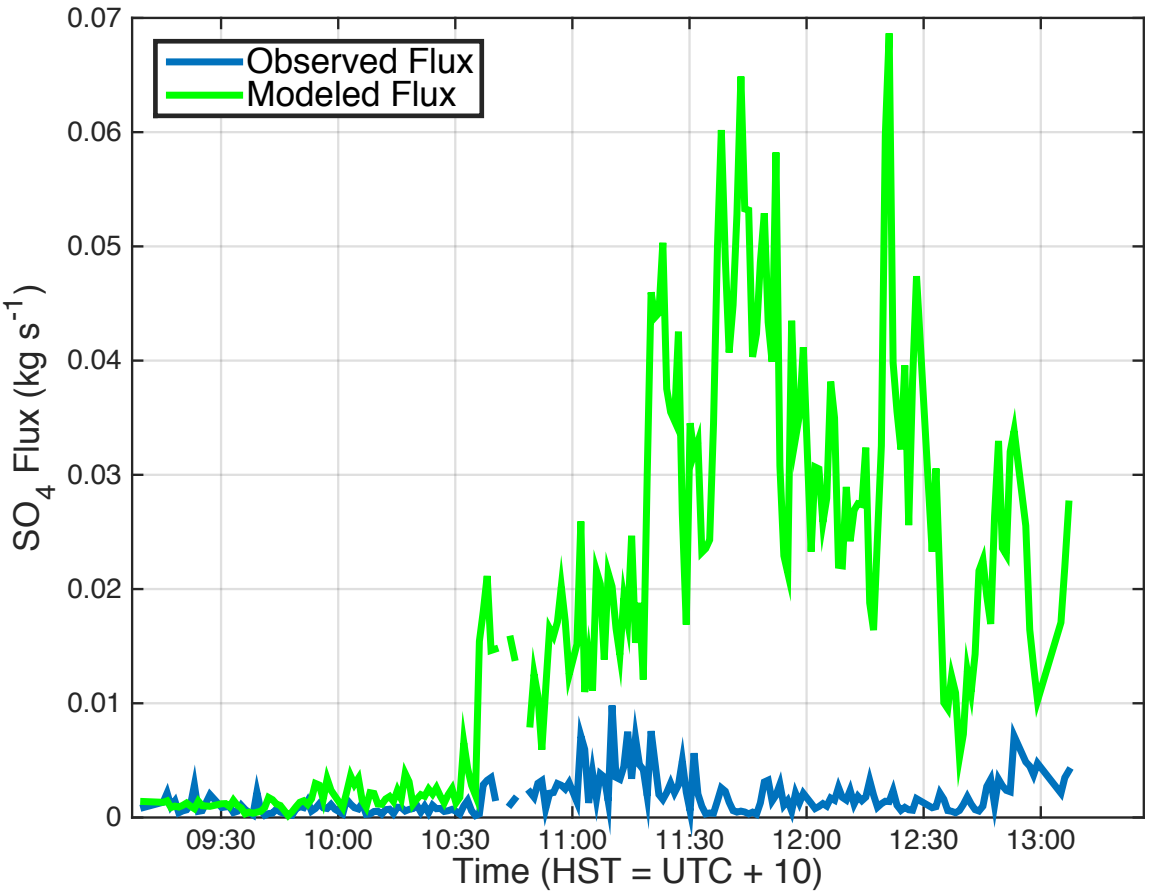

Figure 20: Comparison of estimated sulfate aerosol flux based on observations with a flux derived from sulfur dioxide fluxes at the same site and the new sulfur chemistry methodology. When SO_2 emissions increase around 1030 HST the numeric scheme estimates a much higher sulfate flux than what is estimated from observations.

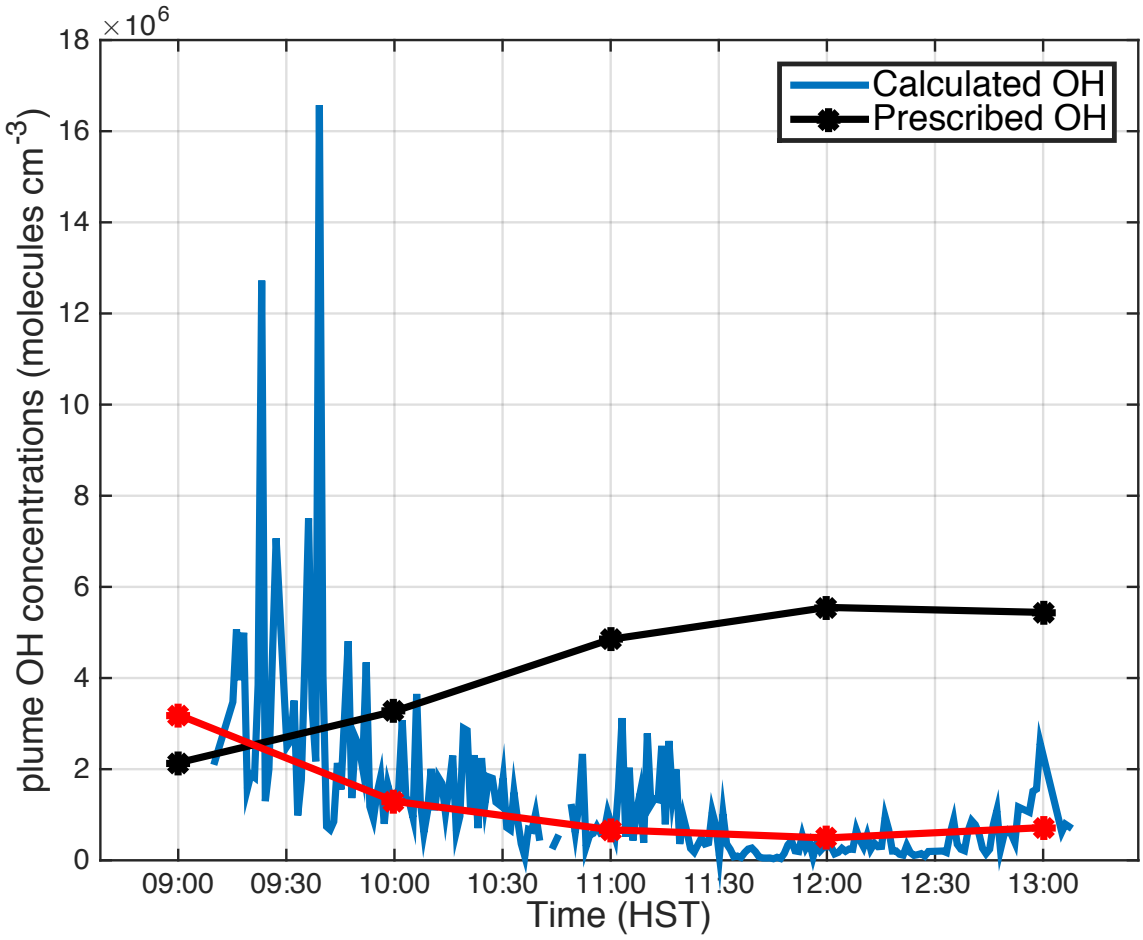

Figure 21: Calculated OH concentrations for 9 July 2015 compared to mean OH concentrations prescribed for the model sulfur scheme. Red line represents hourly averaged OH concentrations calculated from flux data.

Representing this apparent limit of the OH conversion pathway in the gridded environment of the model is challenging and may turn out to be unnecessary. Observations of the plume reflect a relatively small volume of air with dense concentrations of SO_2 and SO_4. In a modeling framework, the plume is represented by values averaged over the larger atmospheric volume of the model grid. This reduces the likelihood that the rate-limiting SO_2 concentration will be reached within the model grid. Given the small grid sizes, especially near the

surface where there are four model levels below 200 m AGL, modeled emission particles split often into several smaller particles, each with a fraction of the original particle mass, as the particles disperse and spread out over multiple meteorological grid points. Details of this process can be found in Draxler and Hess [1997, 1998].

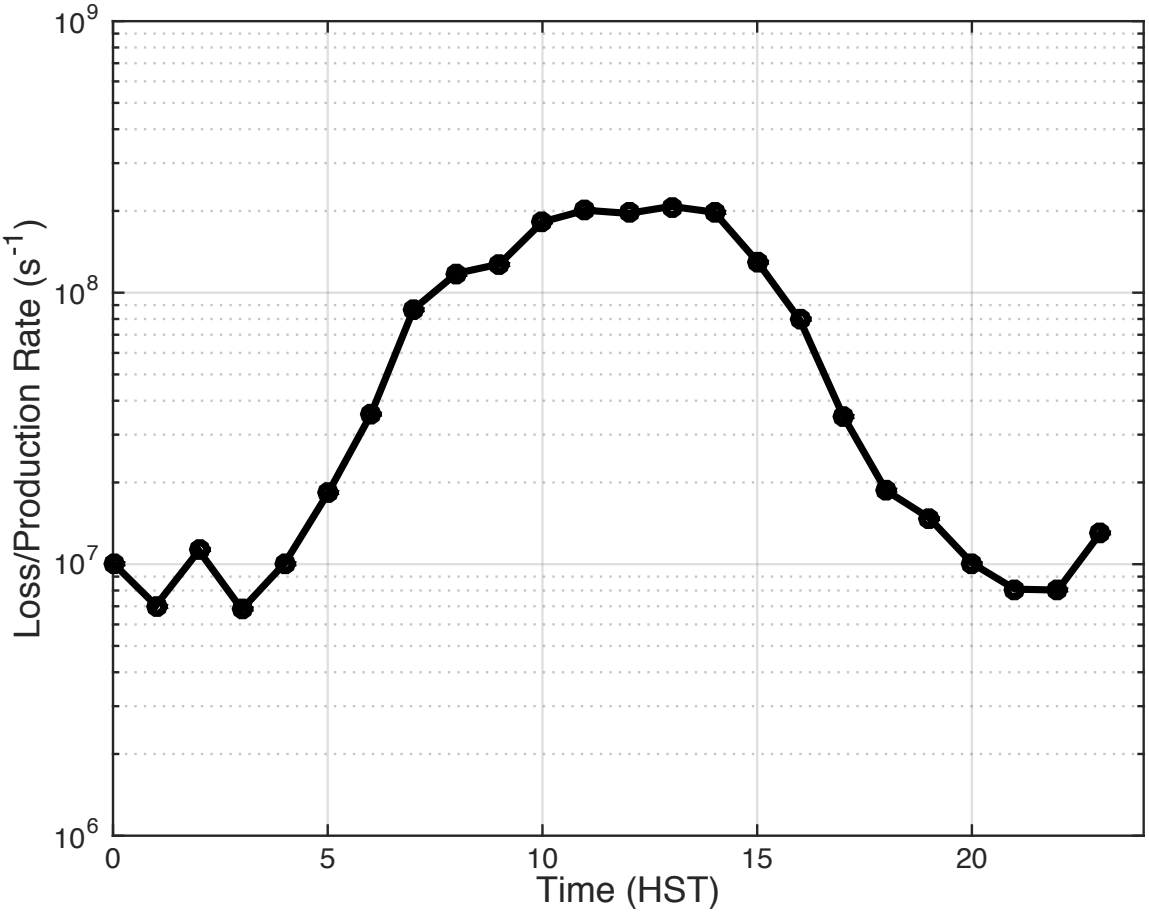

Figure 22: Estimated loss/production rate (s^{-1}) of OH calculated from INTEX-B CO, CH4, and OH data.

4.4.2 Qualitative Evaluation

The new sulfur chemistry routine (hereafter referred to as NEW) was implemented in the UH Vog Model and tested against existing chemistry options. These options include the constant conversion between SO_2 and SO_4 used in the operational model (hereafter referred to as the operational scheme or OPS) and the

prior version of the sulfur chemistry module described by Rolph et al. [1992; 1993] (hereafter referred to as the old chemistry scheme or OLD). Model output was compared using these chemistry routines and observations of SO_2 and $PM_{2.5}$ (where available) for the three days of the field experiment at the proximal site, the distant site (Pāhala), and Ocean View further downwind. SO_2 and SO_4 output was averaged over each simulation hour and for the surface layer from 0-100 AGL, and converted from kg m^{-3} to ppm and μg m^{-3}, respectively. For OLD, a daytime conversion rate of 1.5% hr^{-1} and nighttime conversion rate of .01% hr^{-1} were prescribed. OPS output was pulled from the model archive and used to represent the constant conversion rate option for model chemistry. A rate of 1% hr^{-1} was used in the operational model setting.

Neither NEW nor OLD model configurations used the vertical plume configuration for initialization. Instead emissions for these simulations were released at 100 m AGL directly above the source location. Initialization of the plume was identified as a major source of error for OPS previously [Businger et al., 2015], so a more simplistic initialization approach for the plume was taken to reduce this source of error for testing of advanced chemistry options.

Since the same plume initialization method was employed for both OLD and NEW configurations that impact of this change could be assessed by comparison with OPS. The plume initialization method appeared to have the greatest impact on SO_2 forecasts at the proximal site. Both NEW and OLD had similar forecasts at the proximal site and showed improved forecast bias at downwind sites while OPS forecasts were consistently lower. The impact of the plume initialization likely

propagated downwind to impact forecasts at other sites as well, but attributing forecast error to plume initialization or chemistry becomes more challenging downwind.

Comparison of model forecasts with observations for July 9th 2015 showed improved forecasts with NEW (Figure 23). Forecasts were extended through July 10th to examine if the diurnal trend in observed quantities at stations downwind were seen in model forecasts. For SO_2 forecasts, NEW was greatly improved over OLD and OPS at Pāhala and Ocean View whereas at the proximal site the forecasts from NEW and OLD were nearly identical. NEW SO_2 forecasts at the proximal site are slightly higher than those from OLD indicating that the conversion rate was lower in NEW. This positive SO_2 bias was magnified at stations downwind where NEW showed elevated levels of SO_2 better than the other options, which displayed only short-term spikes in concentrations.

Comparisons of SO_4 forecasts with observations were more difficult because observations were made for $PM_{2.5}$ of which SO_4 makes up only a fraction. $PM_{2.5}$ observations were not collected at the proximal site but comparison between schemes showed that NEW predicted much higher concentrations then either of the other options. At sites further downwind NEW had lower forecast bias than OLD, which displayed a large negative bias, while OPS had a positive bias resulting from overestimating SO_4 concentrations by one to two orders of magnitude during brief spikes in concentrations. Day 2 and 3 forecasts displayed improved forecasts with NEW as well (Figures 24 and 25). OPS forecasts overestimated both SO_2 and SO_4 concentrations downwind while OLD tended to underestimate both quantities.

Qualitative model results were promising with NEW. Results suggested more stable forecasted concentrations and lower overall bias with NEW compared to OLD and OPS forecasts over the same period. Further evaluation was necessary to determine if this perceived improvement was indeed real. Also, did this forecast improvement extend to other locations as well during kona wind events?

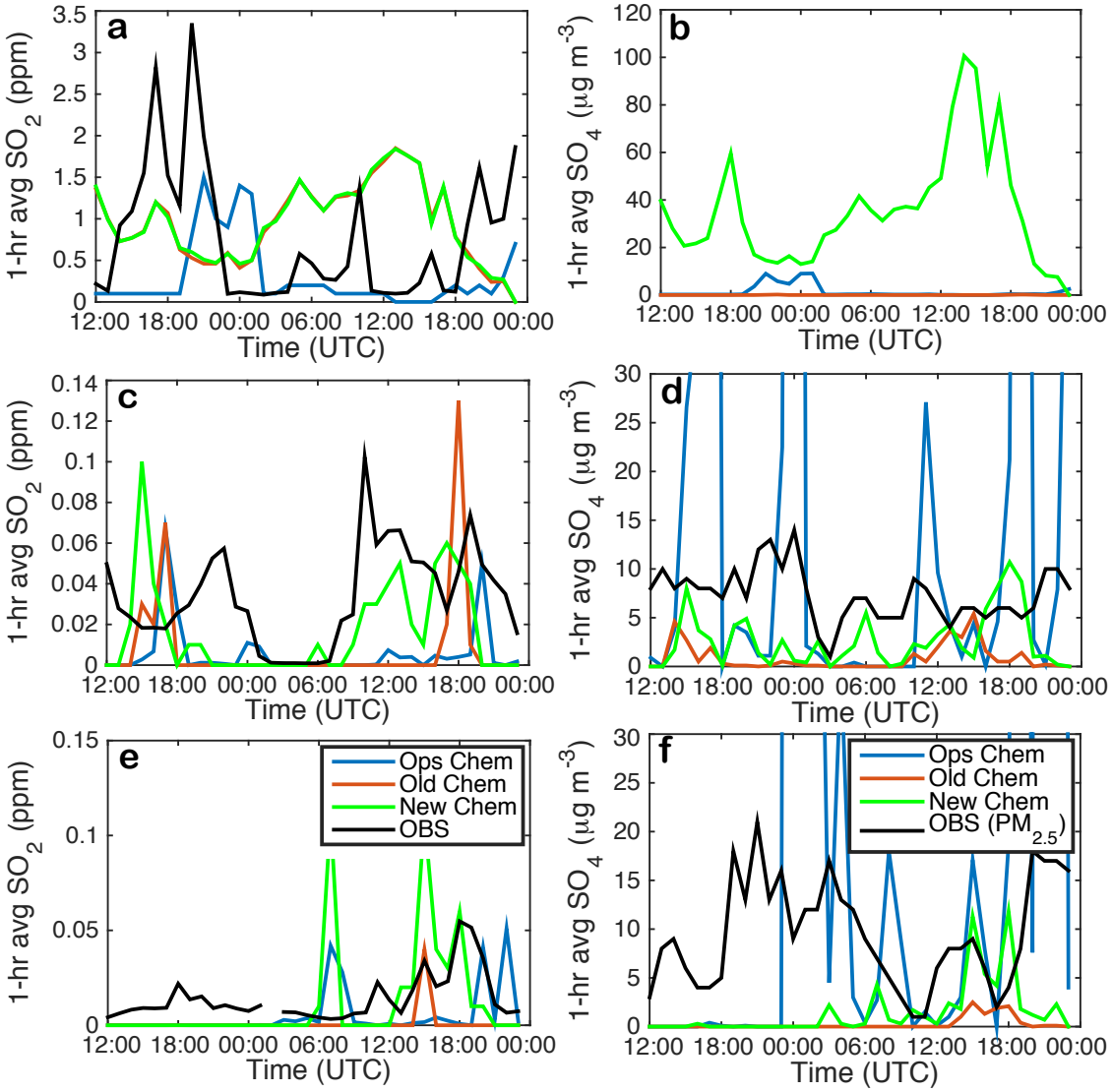

Figure 23: Comparison of model forecasts using the operational model chemistry or OPS (blue), the old chemistry routine developed by Rolph et al. [1992, 1993], or OLD (orange), and the new chemistry routine, or NEW (green) with observations (black) of SO_2 (ppm) or $PM_{2.5}$ ($\mu g\ m^{-3}$) at the proximal observation site (a and b), Pāhala (c and d), and Ocean View (e and f), valid 1200 UTC 9 July 2015 to 0600 UTC 11 July 2015. Note the proximal site has no $PM_{2.5}$ observations (b).

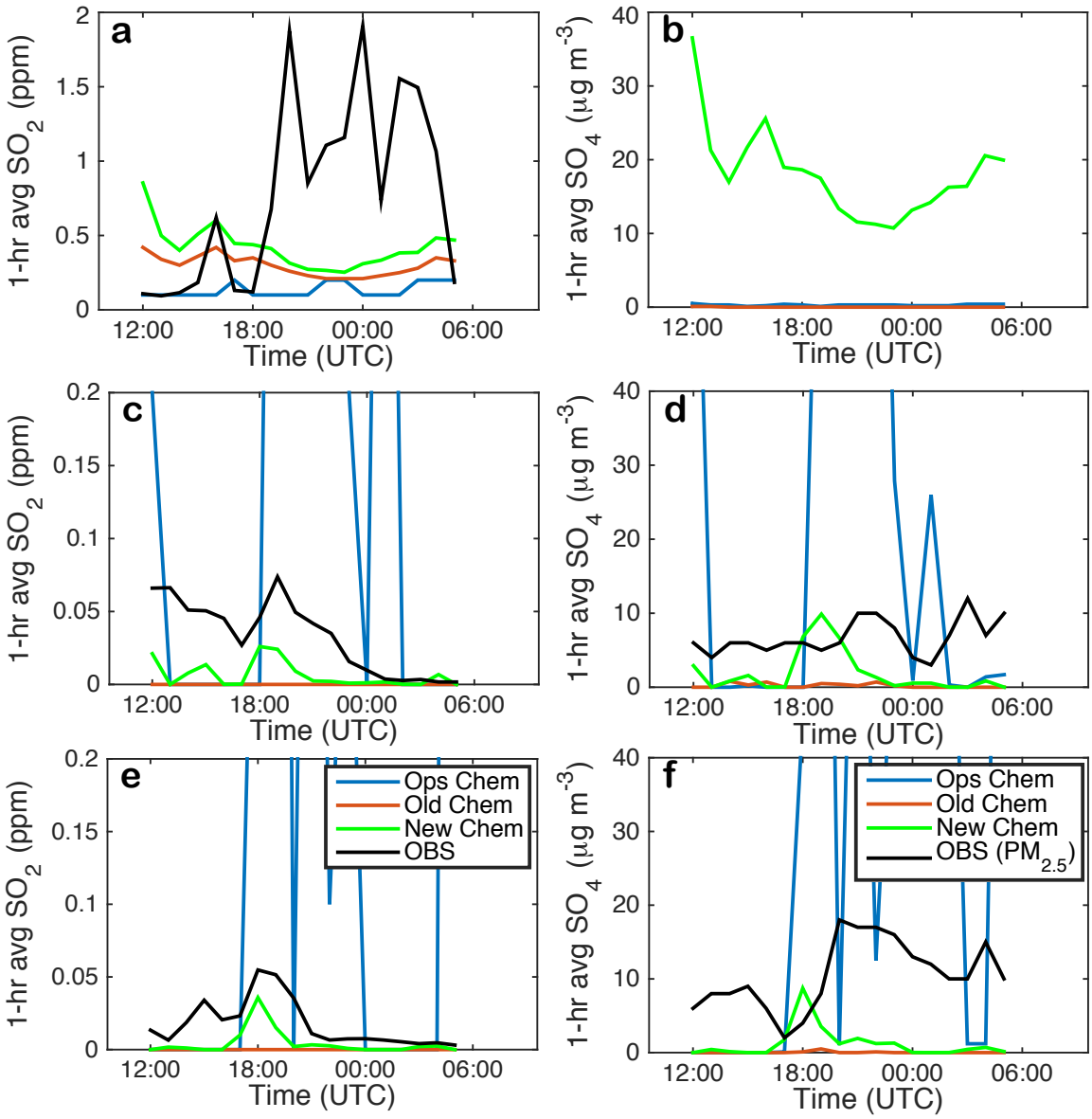

Figure 24: Comparison of model forecasts using OPS (blue), OLD (orange), and NEW (green) with observations (black) of SO_2 (ppm) or $PM_{2.5}$ (μg m^{-3}) at the proximal observation site (a and b), Pāhala (c and d), and Ocean View (e and f) valid 1200 UTC 10 July 2015 to 0600 UTC 11 July 2015. Note the proximal site has no $PM_{2.5}$ observations (b).

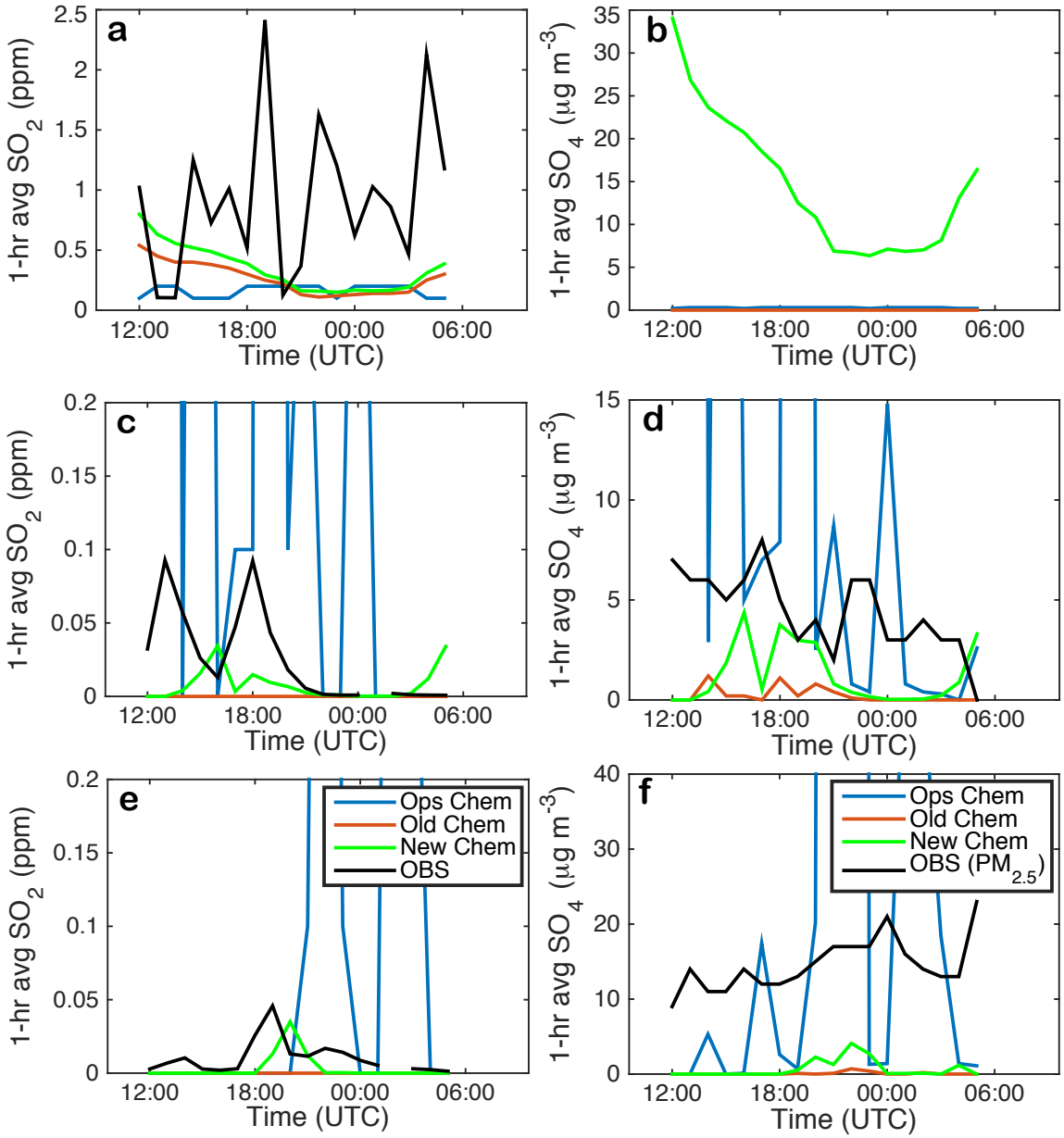

Figure 25: Comparison of model forecasts using OPS (blue), OLD (orange), and NEW (green) with observations (black) of SO_2 (ppm) or $PM_{2.5}$ (μg m^{-3}) at the proximal observation site (a and b), Pāhala (c and d), and Ocean View (e and f) valid 1200 UTC 14 July 2015 to 0600 UTC 15 July 2015. Note the proximal site has no $PM_{2.5}$ observations (b).

4.4.3 Quantitative Evaluation

We know from past validation that the UH Vog Model did well forecasting periods of low SO_2 and SO_4 concentrations, within Air Quality Index (AQI) level 1 (Table 4), but did not perform as well when concentrations increased into AQI levels ≥ 2 [Businger et al., 2015]. Forecasts of high concentrations were the most important for Hawai‘i Department of Health officials and Hawai‘i Volcanoes National Park officials as they attempted to protect the public from poor air quality. Since the three field experiment cases had very few periods of observed higher concentrations, it was hard to say if NEW had shown improvement in representing the higher-end of the concentration distribution.

Therefore the three schemes were run over the course of November 2015 for comparison with observations. This time period contained one prolonged kona wind period for analysis, allowing model performance at additional stations to be done. Model performance was evaluated at Pāhala, Hawaiian Ocean View Estates (HOVE), Hawai‘i Volcanoes National Park Visitor’s Center (VC), Hawai‘i Volcanoes Observatory (HVO), Mountain View (Mt View), and Hilo. Although Kona experienced poor air quality regularly in the form of $PM_{2.5}$ pollution from the volcano (See Appendix), limitations in obtaining data and model configurations did not allow analysis for Kona at this time.

The starting point in the process to determine which model configuration would be most reliable for use by NOAA and other agencies, was to determine how well the models represent high-end concentrations when the observed air quality index (AQI) exceeds level 2 for SO_2 and $PM_{2.5}$ (sulfate aerosols) (Table 4). 1-hr, 3-hr,

and 6-hr time windows were used for all forecast cycles and compared with observations. The 1-hr time period was used primarily to evaluate the impact of the chemistry options on the forecasts, however such a short forecast window would be inadequate for issuing watches and warnings. Thus longer forecast windows were used to determine which model solution would be most appropriate for issuing air quality alerts for high concentrations of pollutants. Time-windows when the observed values exceeded AQI level 2 were compared with the maximum predicted values over these windows.

Table 4. SO_2 (ppm) and particulate matter ($\mu g/m^3$) concentrations used to define the VMAP color codes. The SO_2 designations are consistent with those used by the Hawai'i State Department of Health for their short-term (1-hr) SO_2 index. Environmental Protection Agency (EPA) uses $PM_{2.5}$ concentration thresholds for their 24-hour AQI designations. AQI level 1 = Good, 2 = Moderate, 3 = Unhealthy for sensitive groups, 4 = Unhealthy, 5 = Very unhealthy, and 6 = Hazardous.

AQI level	1	2	3	4	5	6
SO_2 (ppm)	0 - 0.1	0.11 - 0.2	0.21 - 1.0	1.01 - 3.0	3.01 - 5.0	> 5.01
$PM_{2.5}$ ($\mu g/m^3$)	0 - 15	15.01 - 35	35.01 - 65	65.01 - 150	150.01 - 250	> 250.01

Table 5. The 2 x 2 contingency table

		Event Observed	
		Yes	No
Event Forecasted	Yes	H	F
	No	M	Z

Model skill was determined with a 2-by-2 contingency table (Table 5), following the methods of Pearson and Weiss [1979]. From this, the Perfect Prognosis Forecasts (PPF), False Alarm Ratio (FAR), and Probability of Detection (POD) were calculated as follows

$$PPF = (H + Z)/(H + F + M + Z) \tag{4.5}$$

$$FAR = F/(F + Z) \tag{4.6}$$

$$POD = H/(H + M) \tag{4.7}$$

A good model should have a PPF and POD close to one and FAR close to zero. For the purpose of issuing air quality alerts, a high POD was the most desired parameter.

The UH Vog Model was run twice a day out to 59 hours for the entire month of November 2015 with the three different sulfur chemistry routines. This resulted in 60 model cycles for each chemistry option. The first three days were used to spin up the NEW and OLD model simulations (OPS had a fully developed pollutant field due to previous cycles from October), and were not be used in analysis, leaving 54 model cycles for analysis at Pāhala and Ocean View, and 14 cycles at all other sites covering the forecast period of the kona wind event (21 November to 25 November 2015). $PM_{2.5}$ observations at HVO were only available for a short period during the kona wind event due to instrumentation problems.

The UH Vog Model was run using the 1.0 km WRF output grid from the Mauna Kea Weather Center with UH Vog Model output covering an identical 1.0 km grid. Details of this WRF configuration can be found in Businger et al. [2015]. The model was forced with emission data (t d^{-1}) obtained from the Hawai‘i Volcanoes Observatory (HVO) (Figure 26). This data was then converted to units of kg h^{-1} for

input to the model (Figure 27). Although the operational model distributed these emission estimates in the vertical [Businger et al., 2015], this approach was not taken when testing the more complex chemistry schemes (OLD and NEW). This was because the vertical distribution of emissions reflects trade wind conditions and would not reflect the kona wind event properly. OLD and NEW were initialized with emissions released at 100 m AGL. To account for all the emissions being emitted at the boundary of the 0-100 m AGL layer used for model output some factoring of model output was performed to make results comparable to observations being collected at 2.0 m AGL.

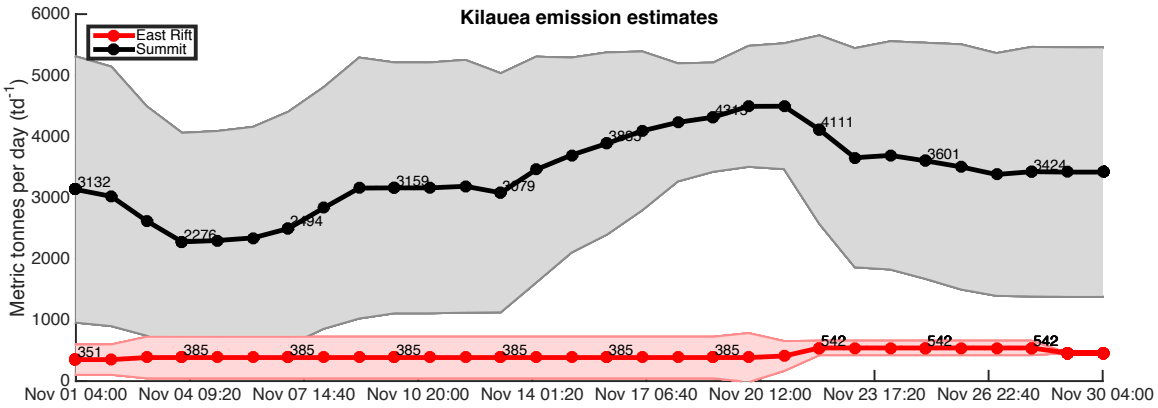

Figure 26: Estimated sulfur dioxide (SO_2) emissions from Kīlauea volcano vents. Estimates are in metric tons per day (t d^{-1}). The shaded area represents the region that encompasses approximately 70% of estimated emissions each day.

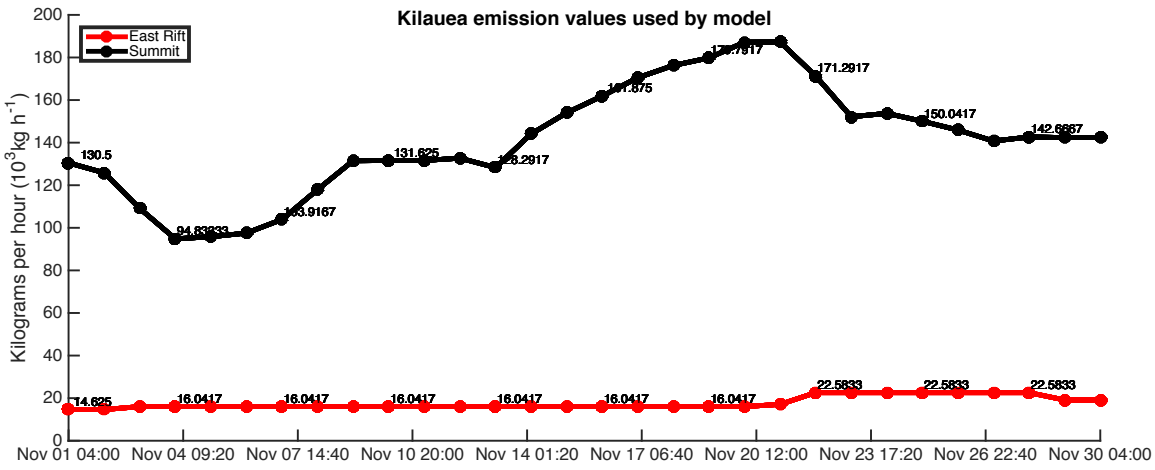

Figure 27: SO_2 emissions (kg h^{-1}) used for model input. Each point represents the values used every hour for both model cycles (00 and 12 UTC) initialized that day.

Measures of model skill for SO_2 and SO_4 forecasts were tabulated for the 1-hr time-window at all stations (Figure 28). NEW showed a significantly higher SO_2 POD than OPS at Pāhala, but only modest gains were had at HOVE, VC, and HVO. Surprisingly, OLD had zero SO_2 POD at either VC or HVO, while NEW showed improvements over OPS, and both NEW and OLD were initialized with the same configuration. NEW SO_2 forecasts improved at Mt View as well, where POD doubled, while Hilo observed no periods when SO_2 exceeded AQI level 2 (0.1 ppm).

The downside of NEW was larger numbers of forecasts that were not observed (F) at all sites, which caused the FAR to increase. Further analysis (not shown) indicated that the more complex chemistry options (OLD and NEW) had a positive forecast bias whereas OPS had a negative forecast bias. The large FAR values at Pāhala, and possibly HOVE, could be attributed to systemic errors in WRF wind fields that resulted in more direct trajectories of the plume than are typically seen. A more direct path limited the amount of SO_2 that was converted to SO_4 by

reducing the travel time between points and thus higher SO_2 concentrations were forecasted.

For SO_4 forecasts, the comparison was more challenging because of the mismatch in observed ($PM_{2.5}$) to forecasted quantities (SO_4). Modest improvements in POD were obtained with NEW and OLD at all sites due to extremely low POD values for OPS. Slight differences in SO_4 POD and FAR between OLD and NEW were seen at all stations. PPF decreased substantially at Pāhala for both SO_2 and SO_4 with NEW and OLD due to FAR increasing proportionally to POD. Minor decreases in PPF were seen with NEW and OLD at Mt View and Hilo for both SO_2 and SO_4, and HVO for SO_2 only.

Similar analysis was performed for 3-hr and 6-hr forecast windows (Figures 29 and 30). For the 3-hr forecast windows PPF values decreased as the number of samples decreased and because FAR and POD increased simultaneously (Figure 29). Pāhala, Mt View, and HVO SO_2 forecasts had the greatest decreases in PPF while POD and FAR increased. VC, HOVE, and Hilo had only slight decreases in in PPF while Hilo saw a slight increase in FAR. SO_4 PPF decreased at all stations and for all model solutions, but at HOVE and HVO the OLD and NEW PPF were slightly better than OPS. This was due to increased POD with OLD and NEW while little improvement was seen in OPS.

POD continued to increase using 6-hr forecast windows (Figure 30). SO_2 POD using NEW exceeded 70% at Pāhala, while VC and Mt View POD approached 50%. The maximum POD using OPS was only 30% at VC and less than 20% at Pāhala. FAR continued to increase for all model solutions, particularly at Pāhala.

SO_4 POD was also greatly improved with both OLD and NEW compared with OPS and approached 40% at Pāhala, HOVE, and Mt View.

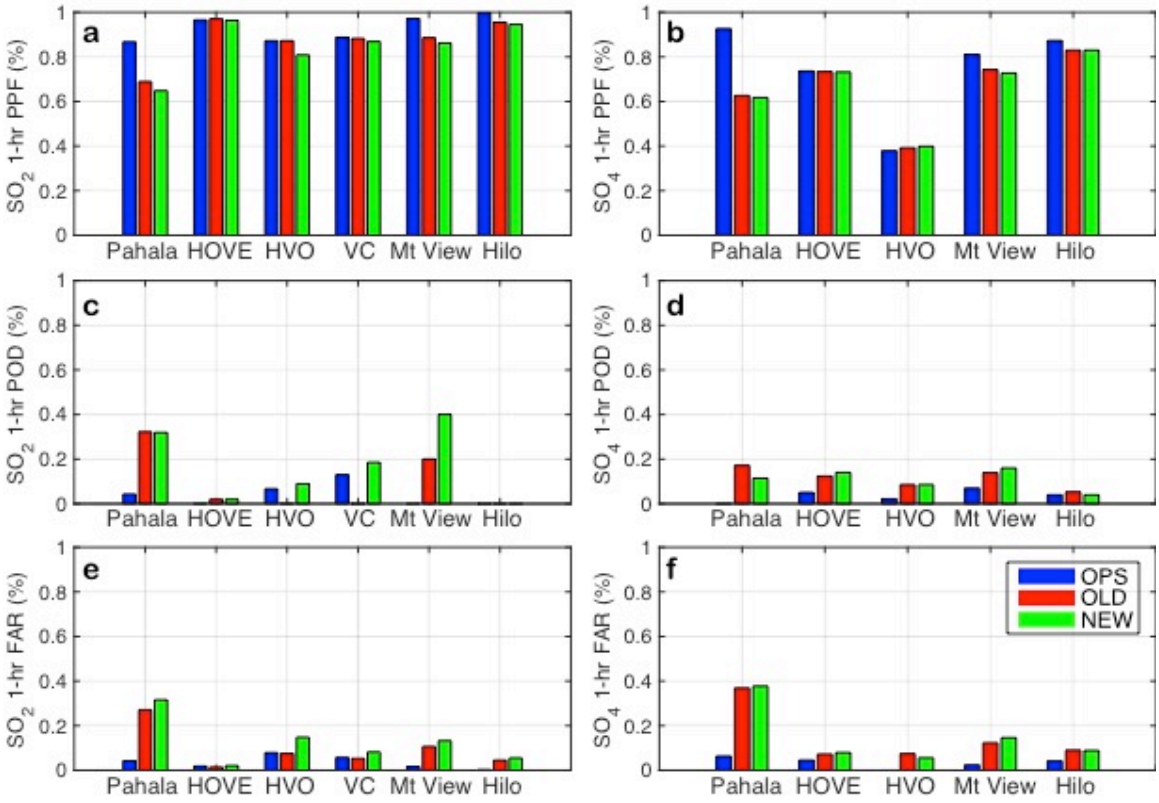

Figure 28: Model skill at all sites evaluated for forecasted concentrations of SO_2 and SO_4 that exceed AQI level 2 over 1-hr forecast windows using Perfect Prognosis Forecasts (PPF) for (a) SO_2 and (b) SO_4, Probability of Detection (POD) for (c) SO_2 and (d) SO_4, and False Alarm Ratio (FAR) for (e) SO_2 and (f) SO_4.

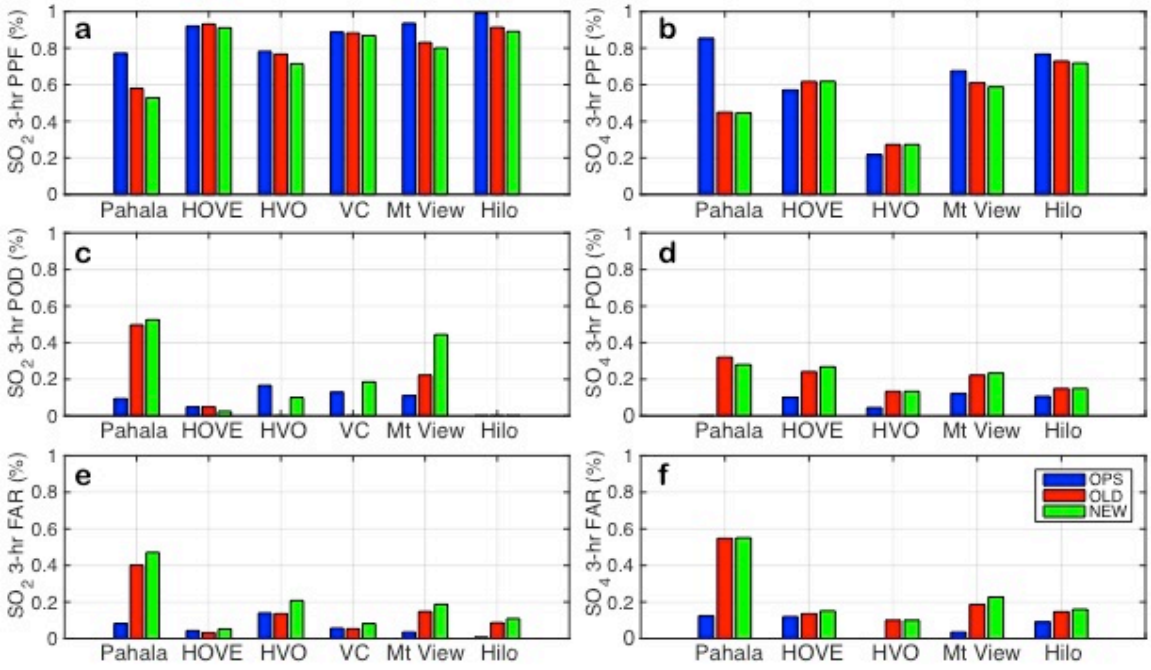

Figure 29: Similar to Figure 28 but for 3-hr forecast window.

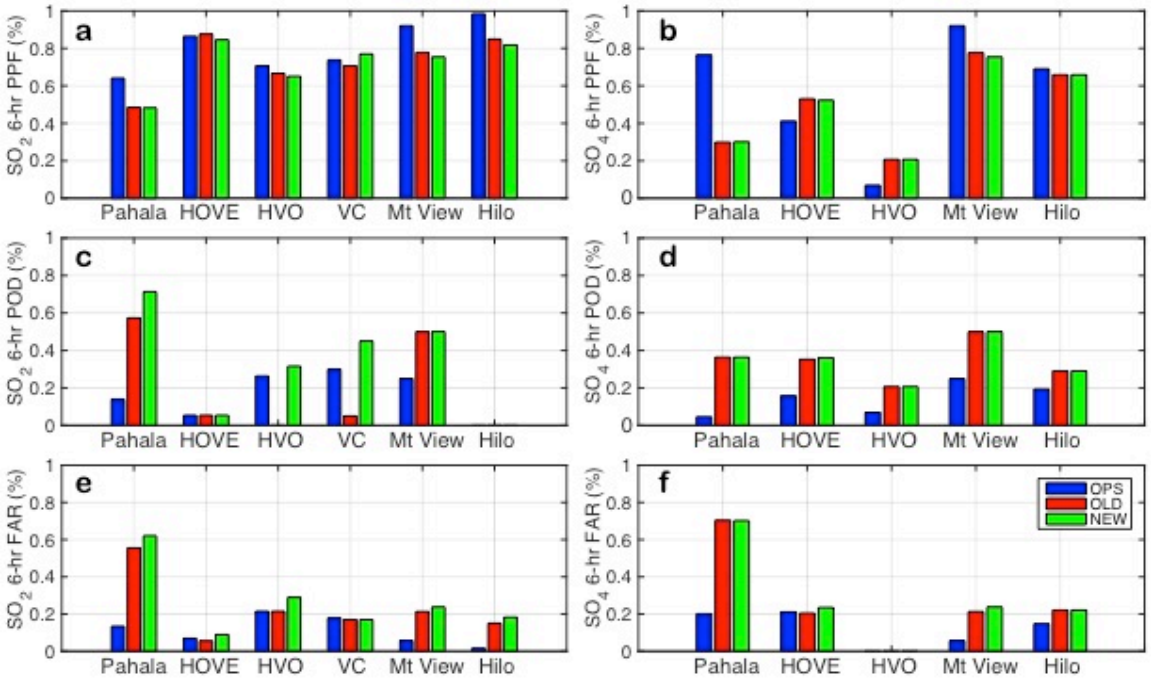

Figure 30: Same as figure 28 but for 6-hr forecast window.

Results from the month-long evaluation displayed improved POD for periods when SO_2 and SO_4 concentrations exceeded AQI level 2 using the more complex

chemistry schemes (OLD and NEW). As longer forecast-windows were used, POD increased for all model simulations, however FAR also increased in tandem resulting in lower PPF. Comparison between OLD and NEW performance showed that at most sites there was little difference between any of the three evaluation parameters regardless of forecast window length. The differences between OLD and NEW were most apparent in SO_2 POD at HVO and VC for all forecast windows, Mt View for the 1-hr and 3-hr forecast windows, and Pāhala for the 6-hr forecast window. Forecast bias calculated from the contingency table as

$$bias = \frac{H + F}{H + M} \tag{4.8}$$

showed NEW had a significantly higher bias than OLD at these sites. Since both models were initialized in the same manner the less restrictive conversion rates in NEW led to these differences. However, given the proximity of VC and HVO to the emission source and the lack of any POD for SO_2 using OLD, the scale of the model was questioned. The size of the plume that impacted these sensors would be on the order of hundreds of meters, making it smaller than the model grid. Since the plume would be averaged over the model grid, plume concentrations would be represented with lower values. Thus, exceedances just over the AQI threshold concentration would be difficult to capture (Figure 31). Scaling of forecasts for these stations would be able to account for this in the future.

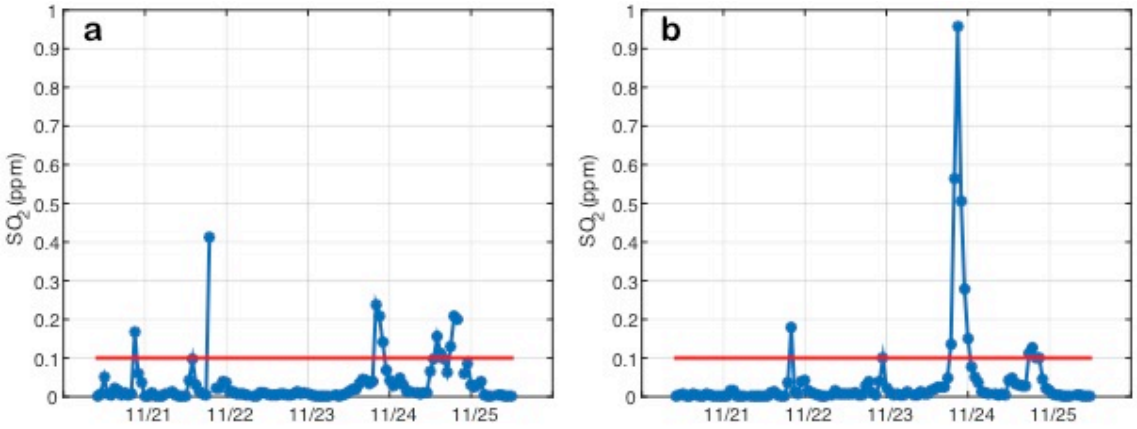

Figure 31: SO2 concentrations (ppm) during kona wind event from 20 November 2015 to 26 November 2015 observed at (a) HVO and (b) VC. Red line represents AQI level 2 threshold = 0.1 ppm.

4.5 Summary

A new sulfur chemistry scheme designed and tested in the UH Vog Model showed promising results for increased probability of detection for poor air quality events. This scheme extended the detail of the existing sulfur chemistry scheme developed by Rolph et al. [1992; 1993] while eliminating seasonal and latitudinal variations that were unnecessary in the tropical central Pacific Ocean. Gridpoint-by-gridpoint conversion rates were calculated for gas conversion of SO_2 to sulfate aerosols (SO_4) to capture the diurnal cycle of this process. This improvement led to higher probability of detection for periods of poor air quality.

Before implementing the new scheme in the model a quick evaluation against observations collected during a field experiment in the summer of 2015 was performed. Observed quantities of total columnar SO_2 and AOD within the volcanic plume were converted to fluxes of SO_2 and SO_4, respectively. The SO_2 flux was used as model input to produce a sulfate aerosol flux. While SO_2 flux rates were low the new scheme produced good agreement with observations of SO_4 flux, but when SO_2

emissions increased the scheme over-predicted sulfate aerosol fluxes. Further analysis of the gas phase reaction suggested that OH concentrations were depleted rapidly through reactions with high concentrations of SO_2 and the formation rate could not keep pace with depletion, limiting the conversion rate.

Qualitative comparison of model forecasts with ground-based observations of SO_2 and $PM_{2.5}$ during the field experiment suggested improved forecasts of SO_2 and SO_4 with the new scheme. The new scheme (NEW) was able to capture short-term increases in pollutants on the same order of magnitude as observations, whereas the operational scheme (OPS) tended to overestimate these features and the older chemistry scheme of Rolph et al. [1992; 1993] (OLD) depicted few of these features further downwind.

A month-long evaluation of all model chemistry options was performed for November 2015. Model forecasts of SO_2 and SO_4 were compared against observations of SO_2 and $PM_{2.5}$ at multiple sites around the island of Hawai‘i over 1-hr, 3-hr and 6-hr forecast windows. Model skill was assessed through use of a 2 x 2 contingency table and derived parameters such as Perfect Prognosis Forecast (PPF), False Alarm Ratio (FAR), and Probability of Detection (POD). Although the overall PPF of the more complex schemes decreased at most sites, improvements in POD were seen for both SO_2 and SO_4 forecasts. When the time windows increased, PPF decreased because of increases in FAR and POD. The increases in FAR and POD were greater for NEW and OLD than OPS, indicating a more complex chemistry option improves forecasts, however SO_2 POD at HVO and VC were greater with NEW than OLD. A larger positive forecast bias in NEW due to the less restrictive

conversion scheme was responsible for this behavior. This resulted a 10% greater SO_2 POD at Pāhala for NEW over OLD.

When incorporated into the UH Vog Model, the newly developed sulfur chemistry routine produced forecasts of SO_2 and SO_4 with improved probability of detection for periods when the AQI index exceeded level 2. This was a key challenge for the operational Vog Model that needed to be addressed so that forecasts could be used to issue air quality alerts and statements through official government channels. Slightly higher SO_2 POD at stations close to the emission source resulted from a larger positive bias in the NEW scheme over the OLD scheme. The greater POD with NEW at these stations led to NEW outperforming OLD overall.

CHAPTER 5. CONCLUSIONS

The University of Hawai‘i at Mānoa Vog Model predicts near-ground concentrations of SO_2 and sulfate aerosols (SO_4) that are used to monitor air quality so individuals with health concerns can limit their exposure to vog. Despite in-cloud conversion of SO_2 to SO_4 being more efficient than gas phase conversion in clear air, conditions around the summit Kīlauea volcano favor gas phase conversion. The summit area is predominantly cloud-free much of the day and SO_2 is emitted from Kīlauea volcano near the ground. As the volcanic plume propagates downwind it tends to flow along the topography staying near the ground. Observations and model results near the vent suggest gas phase conversion is dominant during clear-daytime conditions. In the absence of other reactions or processes during clear conditions, this process could remain dominant overnight as well, however no observations were collected to verify this. Due to these environmental factors and observations, it is likely that gas phase conversion of SO_2 to sulfate aerosol is the main process responsible for sulfate aerosols that make-up a majority of the $PM_{2.5}$ aerosols measured around the island. A more complex representation of this process within the model should produce improved forecasts of SO_2 and SO_4 for sites around the island of Hawai‘i.

A field experiment was carried out in the summer of 2015 to collect observations of SO_2 and sulfate aerosols in order to estimate the conversion rate of SO_2 to sulfate aerosols within the volcanic plume originating from Halema‘uma‘u Crater. Simultaneous observations were collected at two sites downwind of the

volcano and converted to fluxes. Estimating conversion rates from fluxes between these sites was made difficult due to:

1) long plume trajectories resulting in advection times greater than observation periods,
2) cloud cover,
3) plume dispersion, and
4) complex wind fields downwind of the volcano.

Detailed observations near the vent during ideal conditions (9 July 2015) provided the best estimates for conversion rates in clear air. Observations suggested that SO_2 conversion via OH reactions were responsible for sulfate formation in clear air, but at a lower rate than expected from theory. As SO_2 fluxes increased, sulfate formation appears capped, which one would expect given a limited supply of reactant (OH) orders of magnitude below that of SO_2 concentrations. A simple chemistry scheme that could represent this reaction rate with no limitations was created based on kinematic theory and observations. Additionally, observations from all days suggest that a background concentration of sulfate aerosol was present near the vent, which was orders of magnitude lower than past estimates.

5.1 New Chemistry scheme

Model evaluations for each of the sulfur chemistry scheme options were performed using data from November 2015. 54 59-hr model cycles were used in the analysis. Model forecasts of SO_2 and SO_4 were compared with observations of SO_2 and $PM_{2.5}$ for 1-hr, 3-hr, and 6-hr forecast windows. Model performance was assessed via Perfect Prognosis Forecast (PPF), False Alarm Ratio (FAR), and

Probability of Detection (POD) for each predictand at multiple sites on the island of Hawai‘i.

Model POD improved the 1-hr time window SO_2 forecasts when using the more complex chemistry schemes over the constant conversion rate prescribed in the operational model. The more complex chemistry schemes had POD and FAR that were of similar magnitude at both Pāhala and Ocean View.

Improvements in the SO_4 forecasts were similar for the more complex chemistry options at all sites and showed great improvement over the operational scheme. A major difficulty in this comparison was that not all observed $PM_{2.5}$ is sulfate aerosol originating from the volcano and no method has been identified for determining ‘background $PM_{2.5}$ concentrations‘. This issue warrants future consideration. Improving on the operational model was difficult because of the model was originally tuned to observations, i.e., a vertically distributed source term and SO_4 adjustment factor.

Based on the findings of Mather et al. [2012] the operational model initialized with an SO_4 source term equal to one percent of SO_2 source term. Data collected during the 2015 field experiment suggested this term was two orders of magnitude lower and was adjusted for with the model configurations testing the more complex chemistry options. The forecast skill of the operational model at sites further downwind (HOVE and Hilo) could have benefited from larger SO_4 source term in addition to the constant conversion rate of SO_2 to SO_4. With a high POD in the operational model though comes a FAR of similar magnitude.

SO_2 FAR was much higher for the new schemes than for the operational model. The large FAR at Pāhala in particular could be attributed to the way the model was calculating output over a deep layer such that forecasts of vog in the lower boundary layer were not reflective of the surface layer observations made at 2 m AGL. Surface observations showed a clear diurnal evolution driven by upslope/downslope flow (See figure A5 in Appendix A). Boundary layer winds were influenced more by the trade winds, thus direct transport from the volcano was apparent in the model resulting in higher forecast concentrations of SO_2 and lower forecast concentrations of SO_4. Direct observations of the plume during the 2015 field experiment and by UH and USGS personnel suggested the plume was transported by the trade winds away from the summit of Kīlauea but followed the terrain as it propagated and dispersed downwind. This suggested that emissions take an indirect route to Pāhala that may not be well represented in the model.

As longer forecast windows were used, both POD and FAR increased much faster using the more complex chemistry schemes than with the operational scheme. Using a 6-hr forecast window and the new sulfur scheme obtained SO_2 POD $\geq 50\%$ at three sites while two additional sites had the best POD among the schemes. SO_4 POD improved as well with small differences between the complex chemistry schemes.

The results of this evaluation suggest the new sulfur chemistry scheme had improved SO_2 forecasts for sites around the island of Hawai‘i. The longer time windows improved the POD for the model and were seen as more appropriate for

issuing air quality alerts, watches, and warnings. SO_4 forecasts saw improvements in POD but to a lesser degree than SO_2.

5.2 Future Work

The addition of a more complex sulfur chemistry scheme into the UH Vog Model has improved the forecast skill for SO_2 and SO_4 across the island of Hawai‘i. However, room for improvement still exists for plume initialization and representation of local circulations.

5.2.1 Plume-rise Initialization

Currently the operational model initializes with static vertical plumes meant to represent the plume during trade wind conditions. Thus emissions are released from 50 m up to 700 m AGL and extending from the source point to the southwest. This configuration does not account for changes in wind direction, turbulence, or atmospheric stability and results in forecasts that are not representative of non-trade wind conditions.

There is limited plume height information from Halema‘uma‘u Crater, however available data suggests the plume height is well correlated to wind speed (Figure 32). A correlation with atmospheric stability is also expected but due to the visual impairment posed by clouds all observations were collected during fair weather, typically in the early morning, limiting any meaningful correlation between plume height and stability. A more accurate and continuous estimate of plume height would be possible using one or more ceilometers permanently installed at HVO and set in scanning mode. Using this data a plume-rise algorithm already developed, based on the work of Freitas et al. [2010], could be refined and

implemented in the model. This would likely improve forecasts in Hawai'i Volcanoes National Park at HVO and Kīlauea Visitor's Center but could also improve forecasts downwind as the plume continues to disperse.

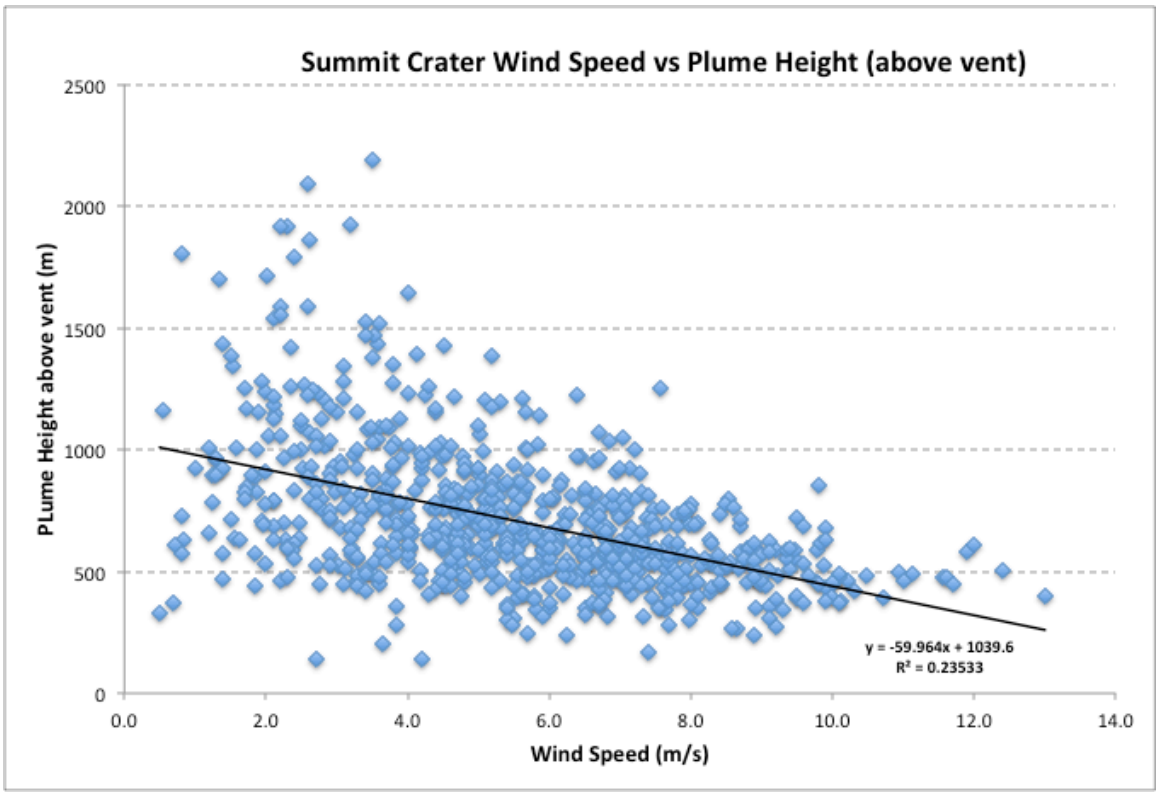

Figure 32: Scatterplot of observed wind speed (m s-1) at Hawai'i Volcano Observatory vs. estimated plume height (m AGL) at Halema'uma'u Crater. Plume height estimates are done through visual observations using a clinometer.

5.2.2 Data Assimilation

The high SO_2 FAR and low SO_4 POD at Pāhala suggest that local wind circulations may not be well represented in the WRF model used to initialize the UH Vog Model. Data assimilation could be used to remedy this to some degree. The current operational workflow has an approximately 12-hr lag. This would allow 12 hours worth of observations from 9-13 meteorological stations reporting wind data

on the windward and southern Kona coasts to be used to update the wind fields forcing the model. The benefit of assimilating this data may be lost shortly after the station data stop being assimilated depending on the time of day, but the benefit of the data could extend for several more hours in which case a significant fraction of the forecast window could be improved. This could also benefit forecasts at Ocean View and Mt View due to the location of the station data to be assimilated.

5.2.3 Extend Evaluation

A one-month evaluation provided enough data to evaluate the model adequately at Pāhala and Ocean View, however, fewer observations are available at other sites. Also, no analysis was possible at Kona which experiences poor air quality regularly. An extended analysis seems appropriate to evaluate the model at sites impacted during kona wind events and at the Kona monitoring site as well. Somewhere between 6 months and 1 year would provide enough data to evaluate the model at all sites. A longer evaluation would also provide more robust measures of model bias that could be used to correct forecasts at certain sites to bring them more in line with observations.

5.3 Ensemble Model

The improvements made to the UH Vog Model by including a more complex chemistry scheme will be used as the base configuration for an ensemble prediction system. An example of one potential ensemble configuration is presented in Pattantyus and Businger [2015]. Such a system has the benefit of describing a range of possible conditions and the likelihood that they are realized. Pollutant prediction uncertainty information may be especially critical for economic decisions,

regulatory applications, and human health issues [Draxler, 2003]. The additional information provided by this type of system would provide a higher degree of confidence to Hawai‘i Department of Health officials when considering what type of air quality alerts to issue and for which regions or communities.

The ensemble developed by Pattantyus and Businger [2015] was a simple meteorological ensemble. The assumption behind the meteorological ensemble is that errors in the downwind plume position are primarily a function of the accumulation of initial errors in the particle trajectories [Draxler, 2003]. The ensemble had 27 members, each with a slightly offset grid. The ensemble uses only one set of models – WRF and UH Vog Model, and thus lacks a range of models that can complement each other.

The output of the model was combined to create probability of exceedance (PE) plots that are representations of the probability of exceeding specific concentration level at the n^{th}-percentile values. In a PE plot, only one concentration threshold is considered with multiple probability levels. The output can be displayed as a concentration-probability (CP) plot where concentration contours are plotted at a specific probability level. A CP plot portrays a range of thresholds at a single probability level. The model mean or median values can be used to make compare with observations.

A more comprehensive ensemble is currently in development to include greater member variability. Various mesoscale model output that is readily available can be used to force the Vog Model, creating a new type of meteorological ensemble. Changes to turbulence and physics parameterizations can be included as

well to help account for diffusion and mixing. Variability in emission sources can also be accounted for in an ensemble since the standard deviation of emission estimates is calculated. Even the differing chemistry schemes can be included within the ensemble. All these options will provide a wide range of model variance and ultimately produce higher levels of confidence for forecasts to reduce FAR and improve risk management.

5.4 Further study of sulfur chemistry

Further field experiments to improve understanding of gas and aqueous chemistry are required to improve forecasts of SO_2 and sulfate aerosol both in Hawai‘i and globally, the influence of aerosols on cloud microphysics, and cloud radiative effects. The pristine environment of Hawai‘i, and around Kīlauea volcano more specifically, make it an ideal candidate for further research on this topic. There are no major pollution sources in the region of the volcano and any sources that do exist pale in comparison to the amount produced by the volcano [Hawai‘i Department of Health, 2013].

A field experiment is being planned by University of Hawai‘i at Mānoa and National Center for Atmospheric Research (NCAR) scientists to find a closure scheme for sulfur dioxide emitted by Kīlauea volcano. In order to accomplish this a number of in-situ measurements are needed both within the plume and in clear air to be facilitated by aircraft operated by NCAR. It is hypothesized that the ratio of (SO_2 + SO_4) to CO_2 is a good measure of the evolution and dilution of the plume. In this way, one can measure the rate of oxidation of SO_2 to sulfate aerosols via SO_4. The oxidation rate would be dependent on reactant concentrations such as water,

ozone, and hydrogen peroxide. Tracking these quantities would allow estimation of multiple conversion rates that result in total aerosol concentrations. By tracking the aerosol and SO_2 concentrations one can track the total sulfur budget and find closure for the local sulfur budget.

Other areas of research include determining the cloud microphysical effects and cloud radiative effects of volcanic (sulfate) aerosols. The impacts of volcanic aerosols on clouds have been shown previously [Yuan et al., 2011a; 2011b], however, details of the processes responsible are still poor quantified. These studies and others have focused on impacts far downstream, but given the persistent emissions from Kīlauea combined with the topography and steady island-scale wind and cloud patterns could influence clouds locally. Some early questions to consider include: how do clouds evolve under the same meteorological conditions with and without the presence of sulfate aerosols? How do sulfate aerosols affect cloud liquid water path? How to sulfate aerosols affect cloud lifetime? The reflectance of clouds may be changed due to aerosol loading. Is this the result of changes to cloud liquid water path, cloud drop number, or cloud lifetime? The answers to these questions have implications for both local and global weather and climate. Was the eruption of Kīlauea partially responsible for the Kaʻū drought in 2009? Is sulfate pollution from China altering cloud fields across the North Pacific?

Direct observations of volcanic aerosols and clouds can help address many of these questions. Differences in cloud droplet size distributions can be examined in the presence and absence of sulfate aerosols to determine the impact of aerosols on clouds. Combining this information with existing cloud-aerosol theory and cloud

microphysics theory will drive the understanding of these basic processes forward and improve short-term forecasting of weather. Extrapolating these processes to a global scale will improve our understanding of aerosol impacts on climate and improve climate predictions.

APPENDIX

The Hawai‘i Department of Health (HDOH) maintains three air-quality monitoring sites downwind of Kīlauea volcano that regularly experience poor air quality as a result of vog – Pāhala, Ocean View, and Kailua-Kona. Three months of observations from February to April 2012 were analyzed to determine what time of day and under what wind conditions these communities were impacted by high concentrations of vog to assess the impact sulfur chemistry was having on pollution episodes. Pollution episodes were defined as any one-hour period when observations exceed the lowest threshold of the air quality index (AQI) for either SO_2 or $PM_{2.5}$. Analysis showed that as emissions advect away from the volcano in trade wind flow they were also transported within island/mountain circulations.

Pāhala

The most proximal site to the volcano is expected to experience the worst air quality. Pāhala is approximately 30 km downwind of Halema‘uma‘u crater during trade wind flow. However, Pāhala is significantly lower (250 m) than Halema‘uma‘u (1029 m) and lies in the terrain shadow of Kīlauea, which blocks trade wind flow making it more susceptible to island/mountain circulations. Pāhala does experience a high frequency of poor air quality as defined by SO_2 concentrations exceeding 0.1 part per million (ppm) (Figure A1) or $PM_{2.5}$ concentrations exceeding 15 $\mu g/m^3$ (Figure A2). The nature of these periods of poor air quality will be characterized here.

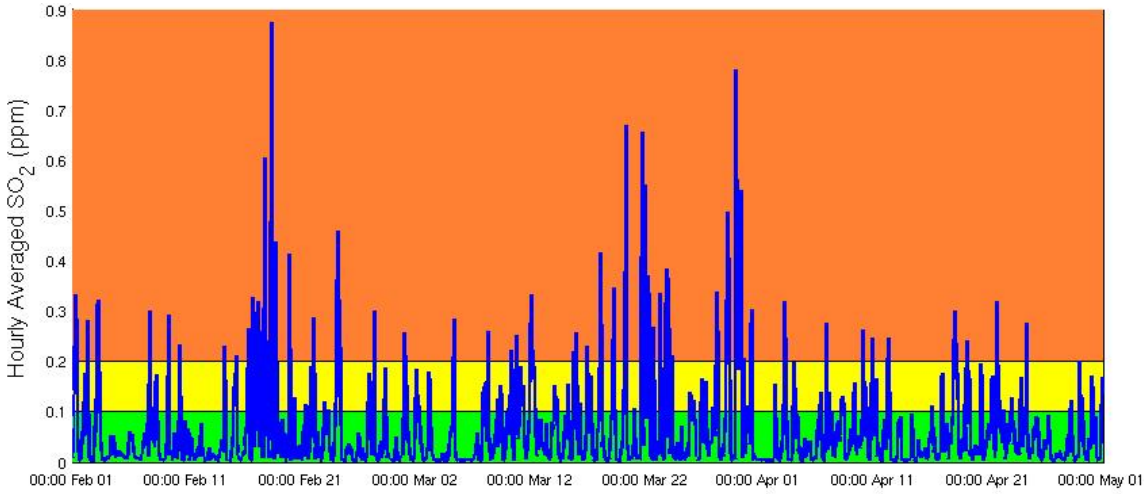

Figure A1: Time Series of hourly SO_2 measurements from Pāhala for the period Feb-Apr 2012. Background colors correspond to Hawai'i State Department of Health's short-term sulfur dioxide advisory levels and color scales. http://www.hiso2index.info/assets/FinalSO2Exposurelevels.pdf

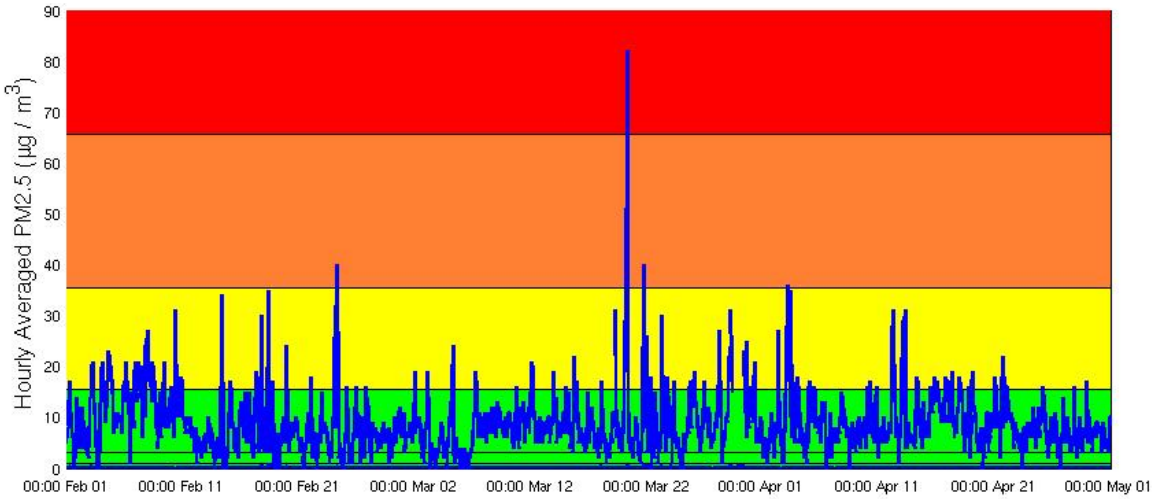

Figure A2 Time Series of hourly $PM_{2.5}$ measurements from Pāhala for the period Feb-Apr 2012. Background colors correspond to EPA short-term $PM_{2.5}$ advisory levels and color scales. http://www.epa.gov/airquality/particlepollution/2012/decfsstandards.pdf

Of the 336 cases in which hourly averaged SO_2 concentrations exceed the 0.1 ppm threshold, a majority are observed overnight and in the early morning (Figure A3). Only 12 observations occur between the hours of 11 and 18 HST, with no instances occurring between 13 and 16 HST. Elevated concentrations of $PM_{2.5}$ (> 15

μg/m^3) are not always found simultaneously with elevated SO_2 concentrations (Figure A3). A histogram of these cases indicates a strong diurnal signal (Figure A4). From sunset to midnight, there is a steady increase in the number of hours SO_2 concentrations exceed the 0.1 ppm threshold. From midnight to sunrise (6-7 HST), the frequency of occurrence is steady before peaking just after sunrise (7-9 HST). After 10 HST, a rapid decrease in occurrence is seen.

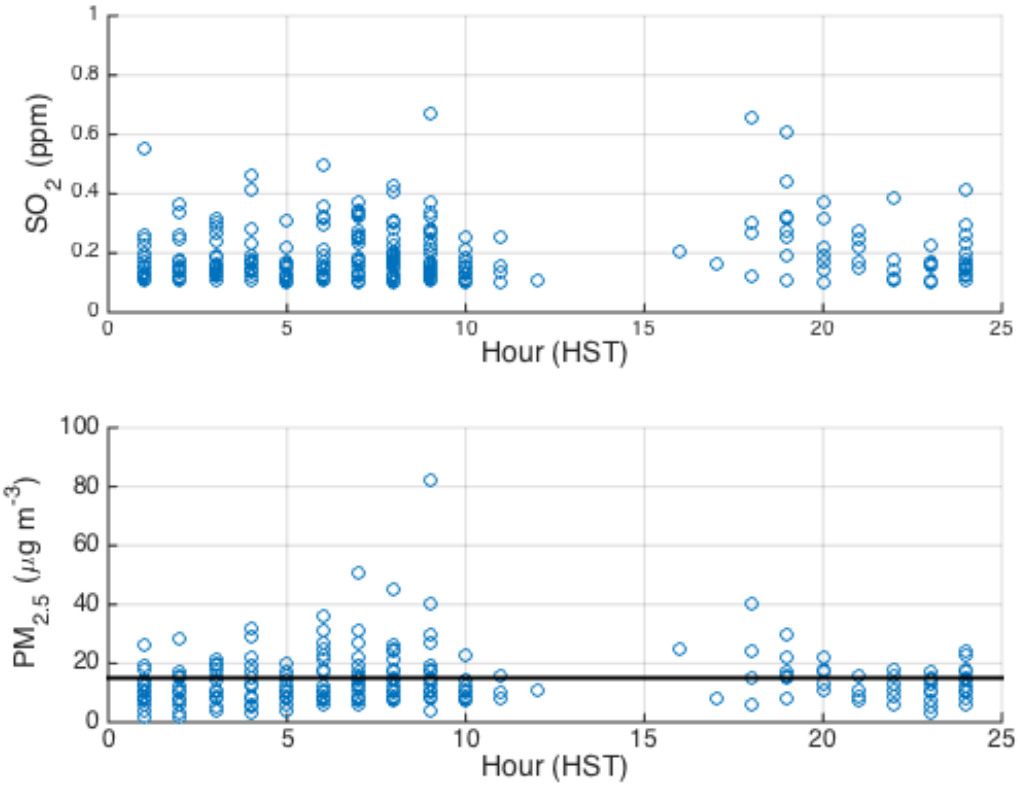

Figure A3: Scatterplot of SO_2 concentrations that exceed 0.1 ppm vs. time of day (top) and corresponding $PM_{2.5}$ concentrations (bottom). Solid line on the bottom indicates threshold for $PM_{2.5}$ concentrations exceeding first $PM_{2.5}$ AQI threshold of 15 μg/m^3.

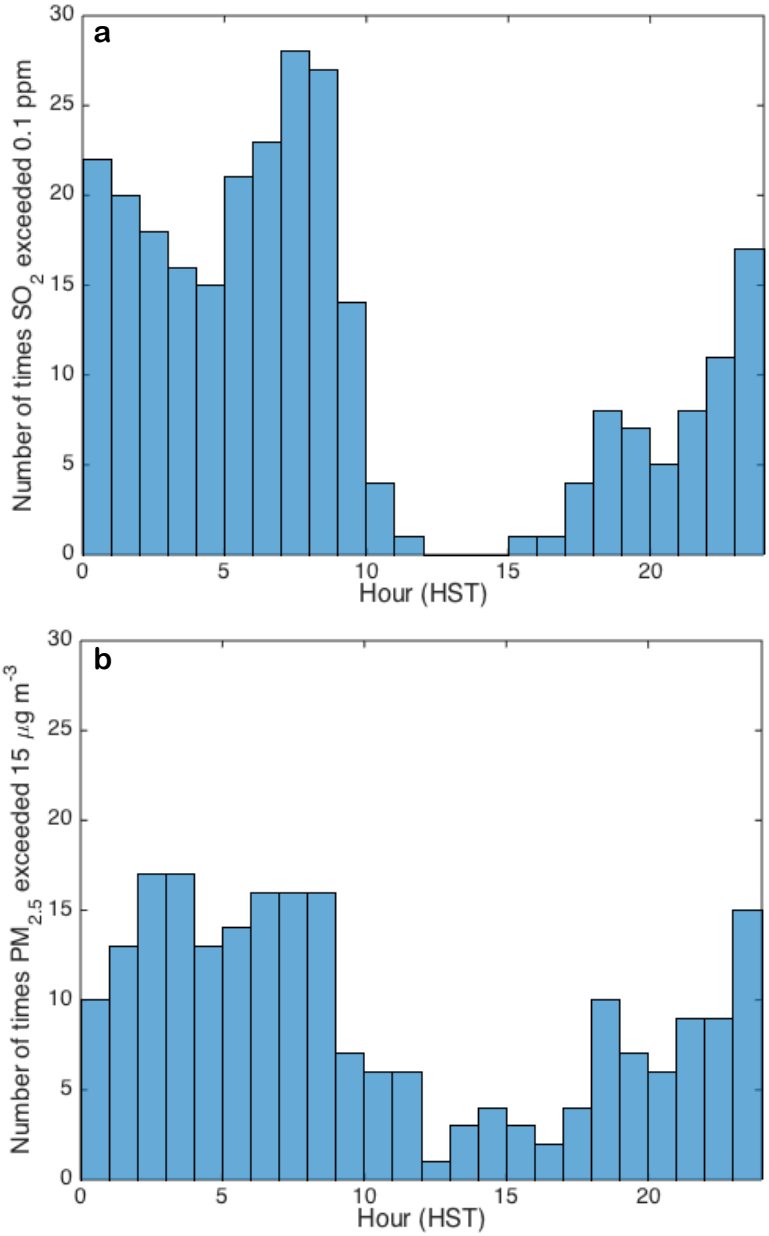

Figure A4: Hour during which SO_2 (a) and $PM_{2.5}$ (b) exceedances were observed Feb-Apr 2012.

A similar analysis of the data for $PM_{2.5}$ also reveals a strong diurnal pattern (Figure A4). Again an after noon minimum is followed by a steady increase to a peak after midnight. Frequencies remain steady until 9 HST and then decrease to a minimum after local noon. Slightly fewer instances of $PM_{2.5}$ exceedance (324) are

seen than SO_2 exceedance (336), but with the same diurnal pattern. Thresholds for both pollutants are exceeded simultaneously approximately 33% of the time.

Winds during these nocturnal and morning events are mainly NW downslope flows (Figure A5). It is expected that on days with stronger winds sulfur dioxide will propagate from source to receptor more rapidly and have less time to convert to sulfate aerosols. Comparison of wind speeds and pollutant concentrations show no discernible correlations to support this.

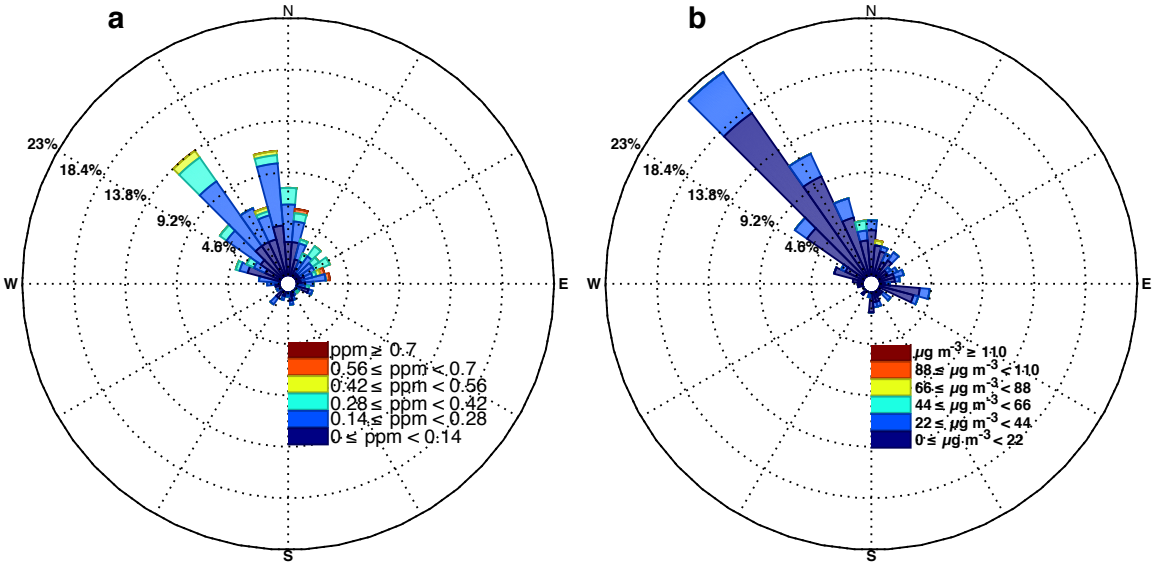

Figure A5: Wind rose plots for (a) SO_2 and (b) $PM_{2.5}$ exceedance events at Pāhala Feb-Apr 2012.

This brief analysis reveals that Pāhala most commonly experiences poor air quality overnight and in the mornings. The prevailing wind pattern at Pāhala appears to be responsible for this strong diurnal signal. Since the dome of Kīlauea blocks incoming trade-wind flow, the area of Pāhala experiences island and mountain circulations. During the day, SE onshore winds blow near the coast and SE upslope flow form on the slopes of Mauna Loa (4170 m). Pollutant levels are low during the day, especially SO_2, since emissions from Halemaʻumaʻu typically get

caught in the NE trade wind flow. At night persistent NW downslope flow comes down Mauna Loa through Pāhala spreading emissions from Halemaʻumaʻu down the lower slopes of Mauna Loa to the coast.

Ocean View

Ocean View is further downwind of Pāhala and Kīlauea volcano at the point where NE trade winds wrap around the southern extent of Mauna Loa. Ocean View experiences poor air quality more frequently from elevated levels of $PM_{2.5}$ (44% of Feb-Apr 2012) than SO_2 (5%) (Figures A6 and A7).

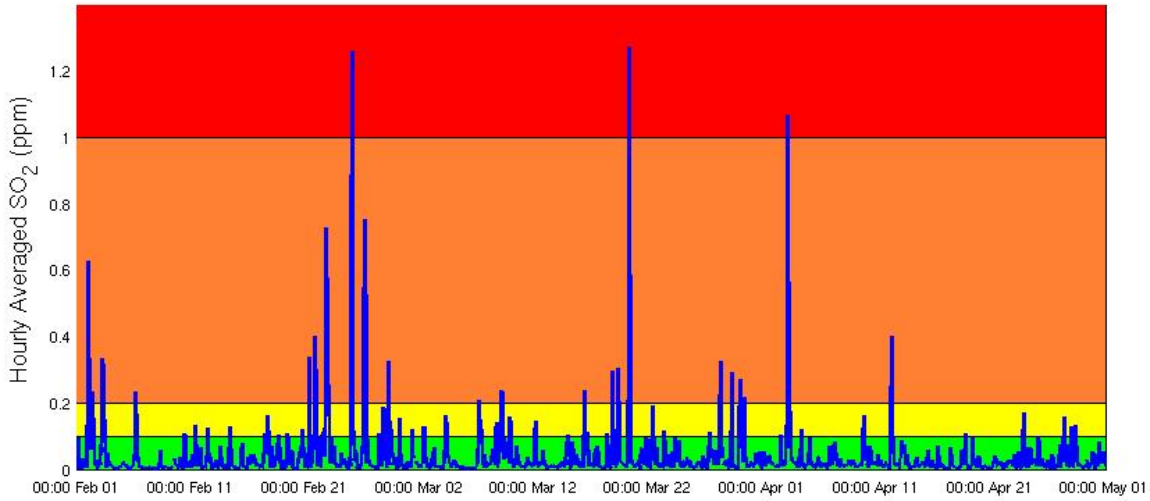

Figure A6: Same as in figure A1 but for Ocean View.

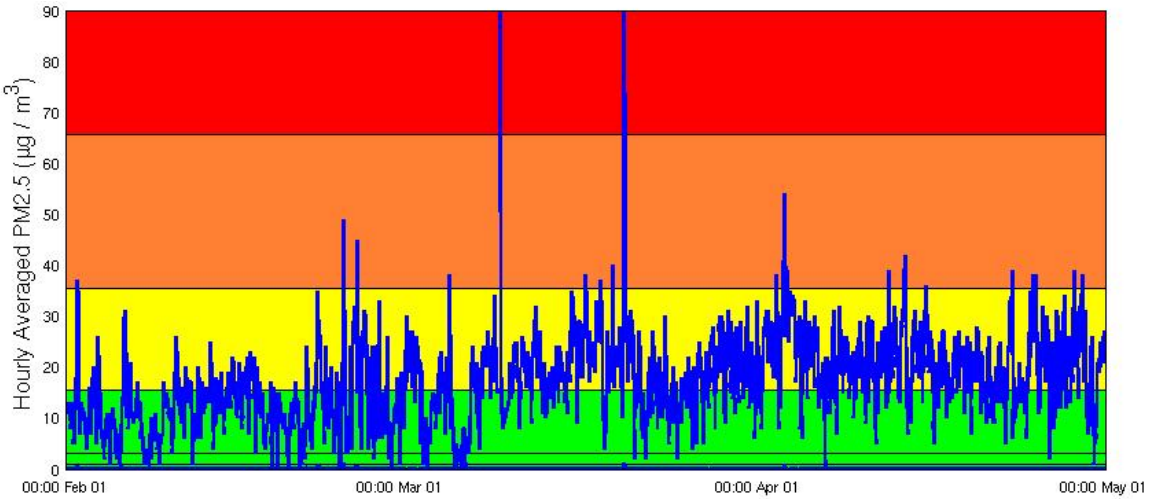

Figure A7: Same as in figure A2 but for Ocean View.

Sulfur dioxide exceedances display a diurnal pattern similar to Pāhala. (Figures A8 and A9). Few observations of exceedances are recorded in the afternoon. An increasing number of exceedances are recorded overnight until a peak just after sunrise and a sharp drop-off after noon. Instances of $PM_{2.5}$ exceedances are more evenly distributed throughout the course of the day at Ocean View (Figure A9) but a minimum amount of exceedances before sunrise is apparent. When SO_2 exceeds the 0.1 ppm threshold, $PM_{2.5}$ also exceeds the 15 $\mu g/m^3$ threshold 80% of the time.

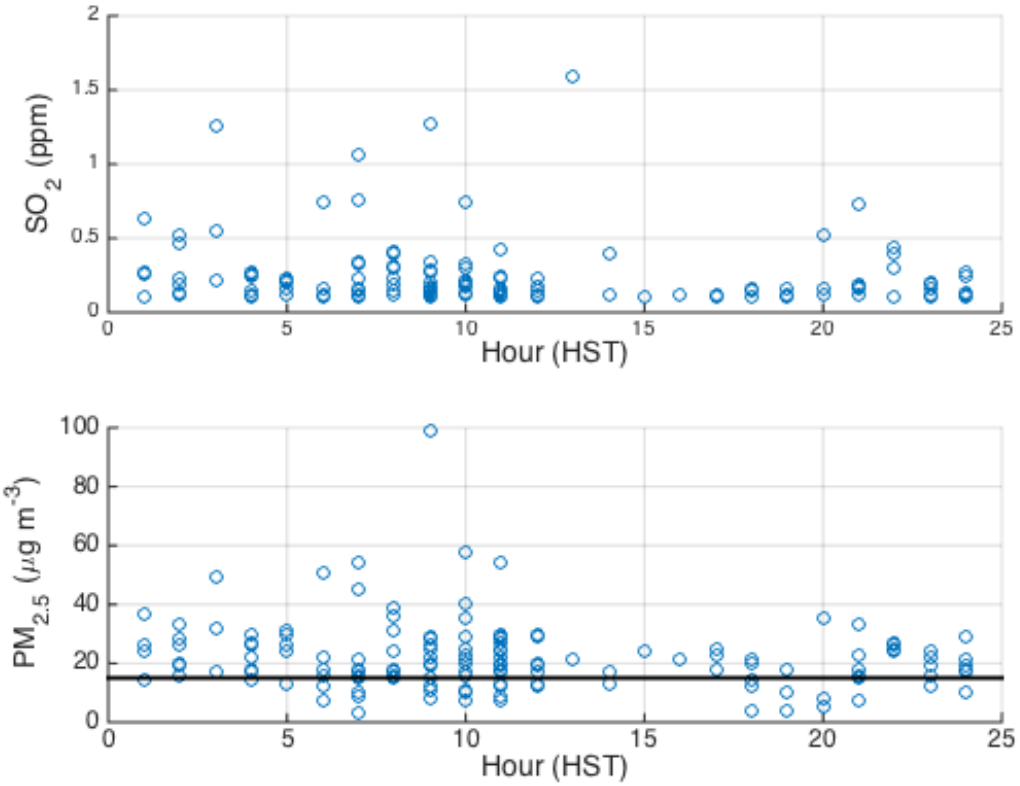

Figure A8: Scatterplot of SO_2 concentrations that exceed 0.1 ppm vs. time of day (top) and corresponding $PM_{2.5}$ concentrations (bottom) at Ocean View. Solid line on the bottom indicates threshold for $PM_{2.5}$ concentrations exceeding first AQI threshold of 15 µg/m³.

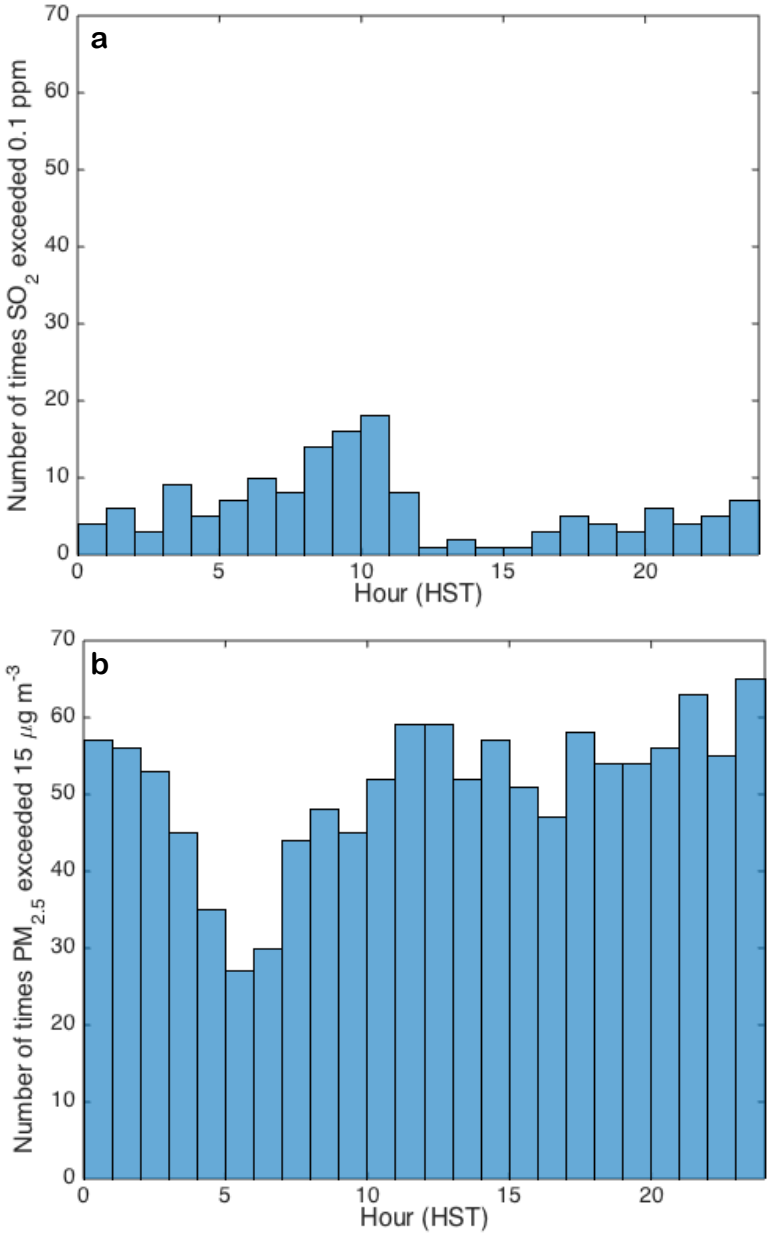

Figure A9: As in figure A4 but for Ocean View.

Winds mainly range from the north to east at Ocean View when the SO_2 0.1 ppm threshold is exceeded (Figure A10). These cases make up only a small percentage of the total number of days when $PM_{2.5}$ are exceeded and thus, winds during $PM_{2.5}$ exceedances show a markedly different wind relation. Wind directions are mainly out of the north during periods of elevated $PM_{2.5}$. By partitioning this

into daytime and nighttime periods it can be seen that at night the wind direction is predominately out of the north, while during the day the wind is mainly out of the west-southwest (Figure A11).

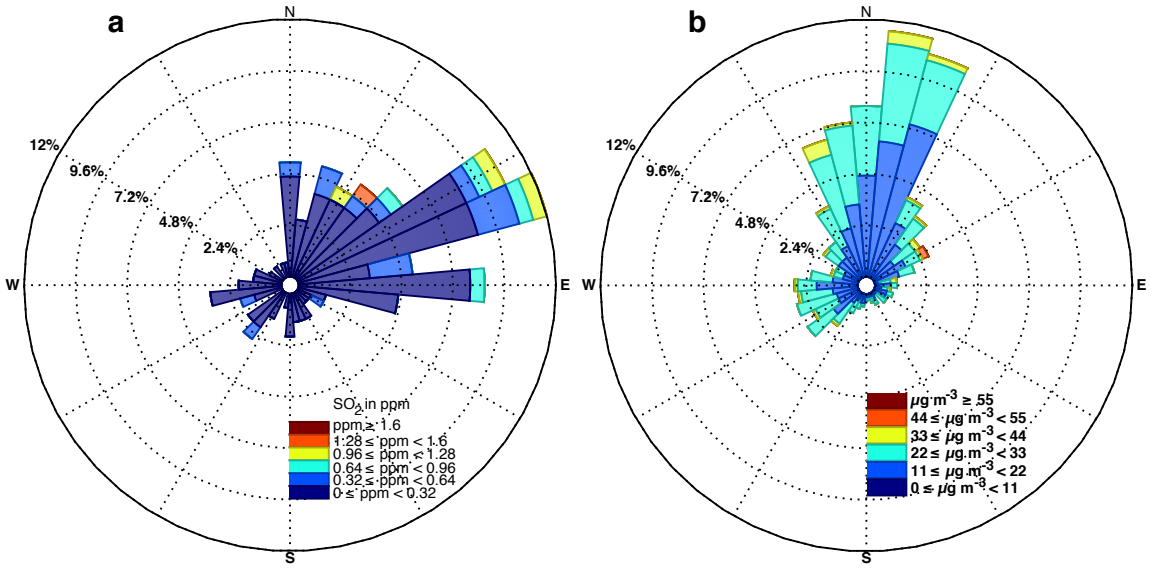

Figure A10: Wind rose plots for (a) SO_2 and (b) $PM_{2.5}$ exceedance events at Ocean View Feb-Apr 2012.

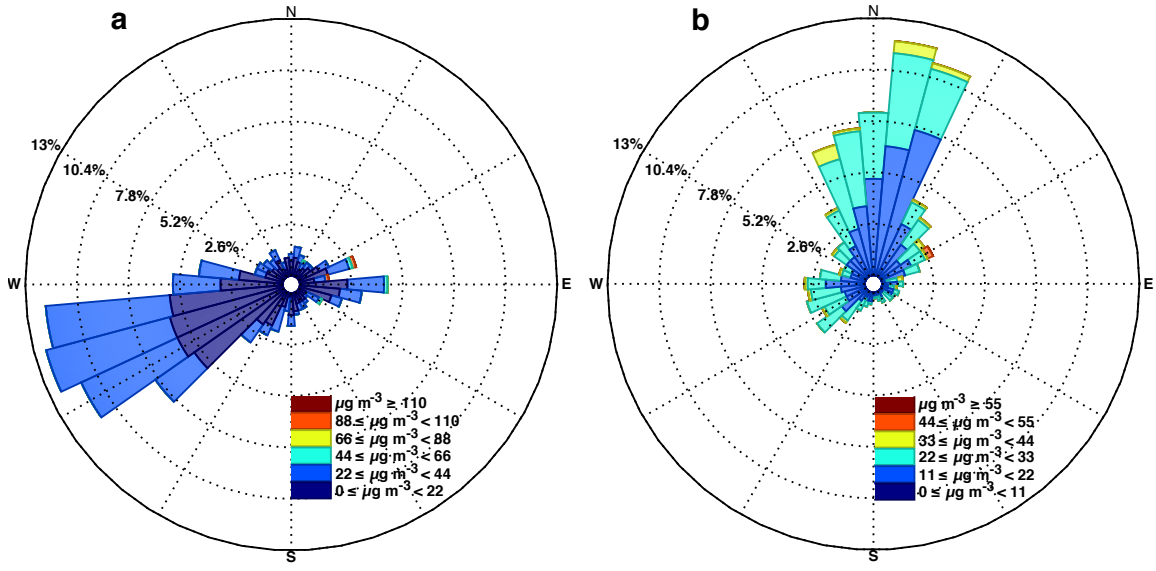

Figure A11: Wind rose plots for $PM_{2.5}$ exceedance events at Ocean View during the day (a) and night (b) Feb-Apr 2012.

Elevated levels of pollutants are more common at Ocean View than Pāhala. Much of this pollution is in the form of $PM_{2.5,}$ as one would expect given its distance downwind from the source and the conversion of SO_2 to sulfate aerosol. Ocean View is at an elevation slightly below Halemaʻumaʻu. Periods of high SO_2 concentrations are mainly seen at night as in Pāhala, however, unlike Pāhala $PM_{2.5}$ episodes are not less frequent during the day at Ocean View. Wind directions during SO_2 pollution events suggest that the volcanic plume is being wrapped around the southern flank of Mauna Loa (NE to E) or carried downslope by nocturnal drainage flows (N). Two thirds (566) of $PM_{2.5}$ events occur overnight with a northerly wind, suggestive of downslope flows, while during the day the dominant direction for $PM_{2.5}$ events (380) is WSW. This would suggest either an upslope flow or local vortex caused by trade wind flow being forced around the southern flank of Mauna Loa and back toward an area of relatively low pressure behind the blocking terrain.

Kailua-Kona

Kailua-Kona is located on the leeward coast of Hawaiʻi but can be considered downwind of Kīlauea due to the lee side vortex that transports northeast trade winds around the island and back onto the coast. Due to its proximity far downstream from the volcano, Kailua-Kona experiences few instances where SO_2 concentrations exceed the 0.1 ppm threshold (Figure A12), however a diurnal signal is still evident in observations. High concentrations of $PM_{2.5}$ are also found here with evidence of both high frequency (diurnal) and low frequency (synoptic) variations (Figure A13).

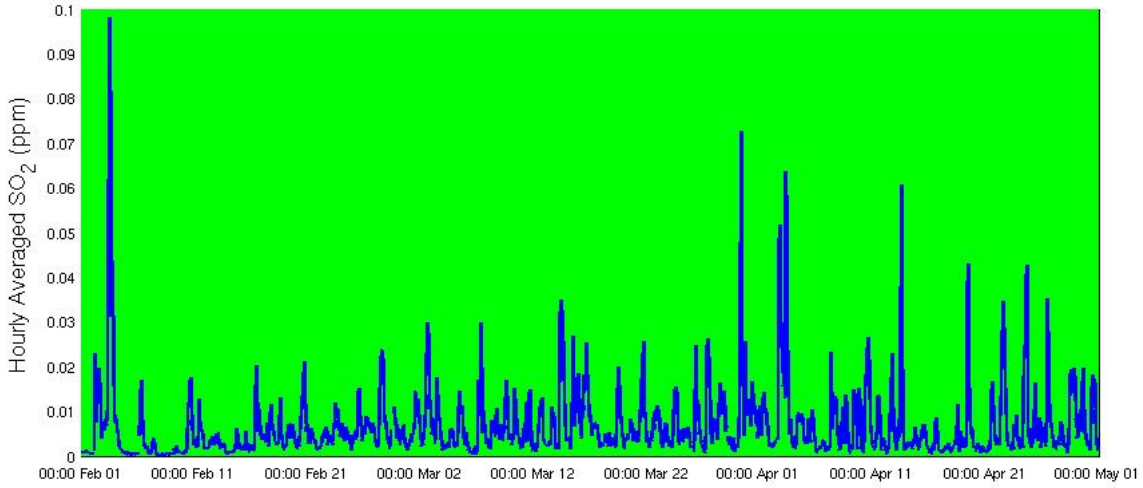

Figure A12: As in Figure A1 but for Kailua-Kona.

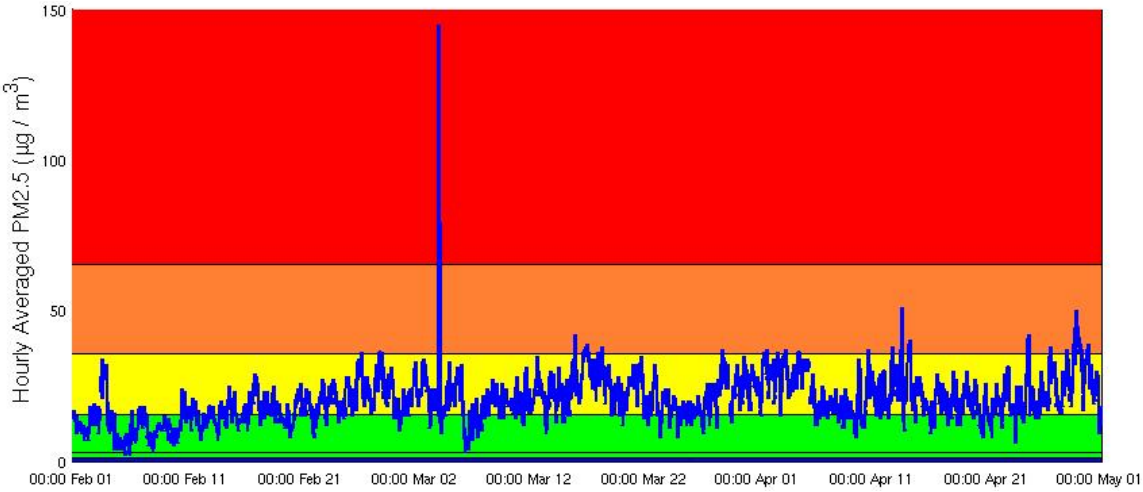

Figure A13: As in Figure A2 but for Kailua-Kona.

In order to characterize the $S0_2$ pattern around Kailua-Kona a lower SO_2 threshold of 0.01 ppm is used. Unlike Pāhala and Ocean View, spikes in SO_2 at Kailua-Kona are experienced mainly during the day (Figures A14 and A15). This is due to the interaction between the lee-side vortex and island/mountain circulation. As a result, there is a peak in the afternoon and a minimum pre-sunrise. Figure A14 indicates that during the majority of these SO_2 events, the $PM_{2.5}$ threshold is also exceeded. When considering $PM_{2.5}$ events a similar pattern as seen

in Ocean View appears with no clear diurnal signal but a maximum number of events occurring near midnight (Figures A16 and A17).

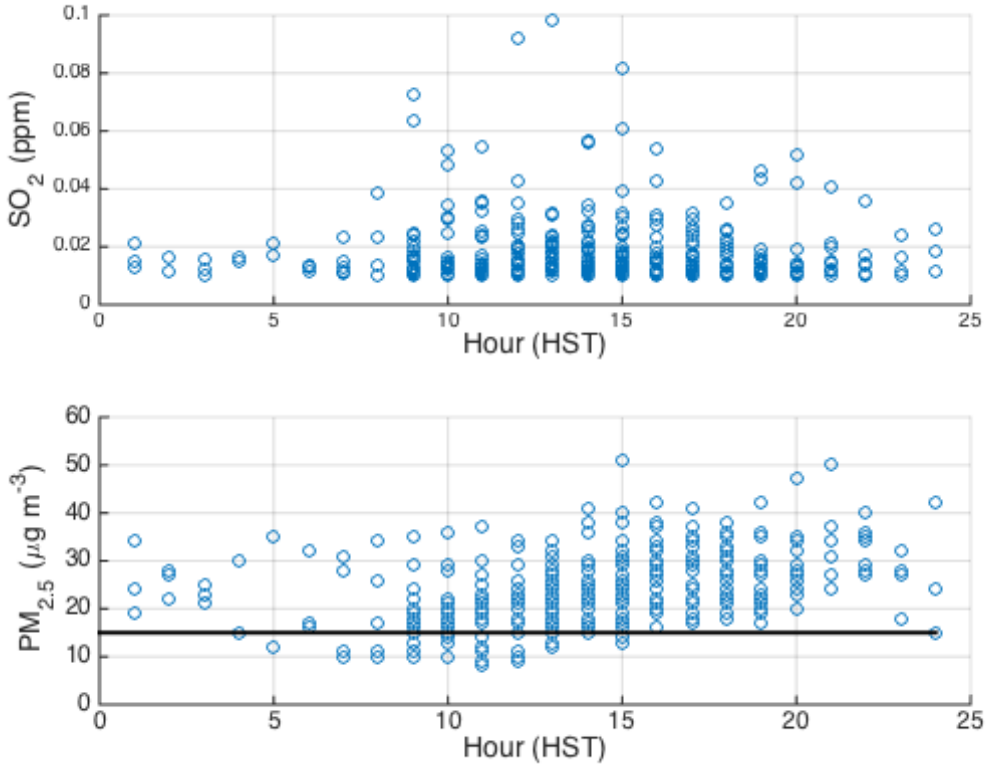

Figure A14: Scatterplot of SO_2 concentrations that exceed 0.01ppm vs. time of day (top) and corresponding $PM_{2.5}$concentrations (bottom) at Kailua-Kona. Solid line on the bottom indicates threshold for $PM_{2.5}$ concentrations exceeding first AQI threshold of 15 µg/m³.

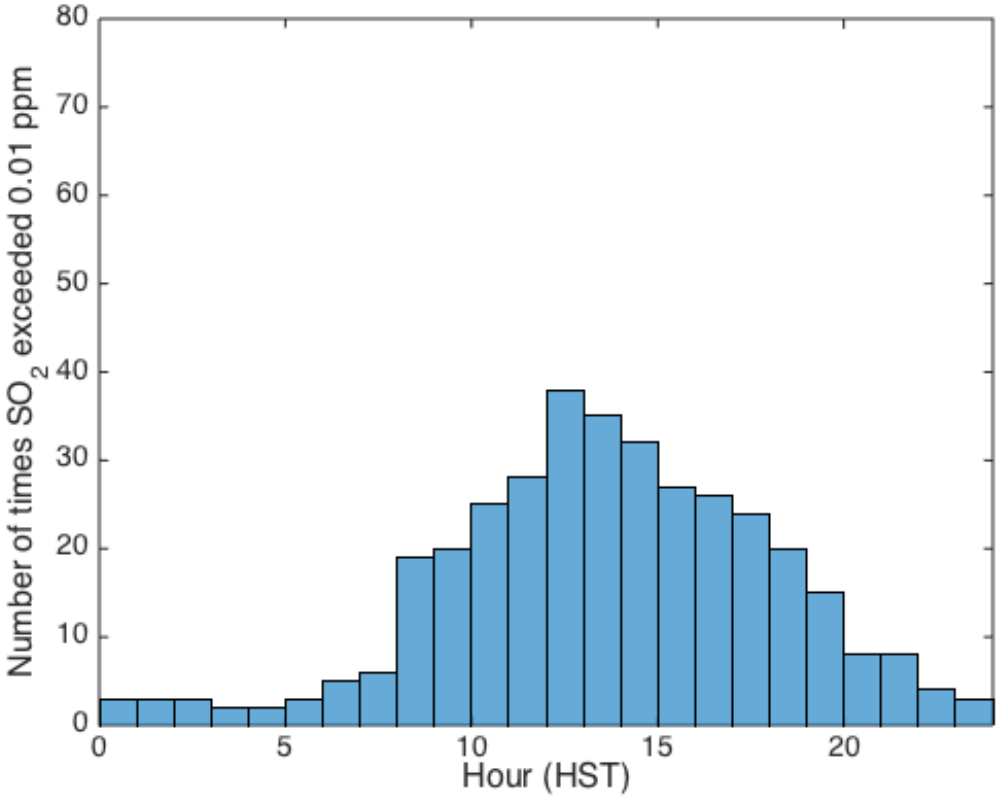

Figure A15: Hour during which SO_2 exceedance events were observed at Kailua-Kona Feb-Apr 2012.

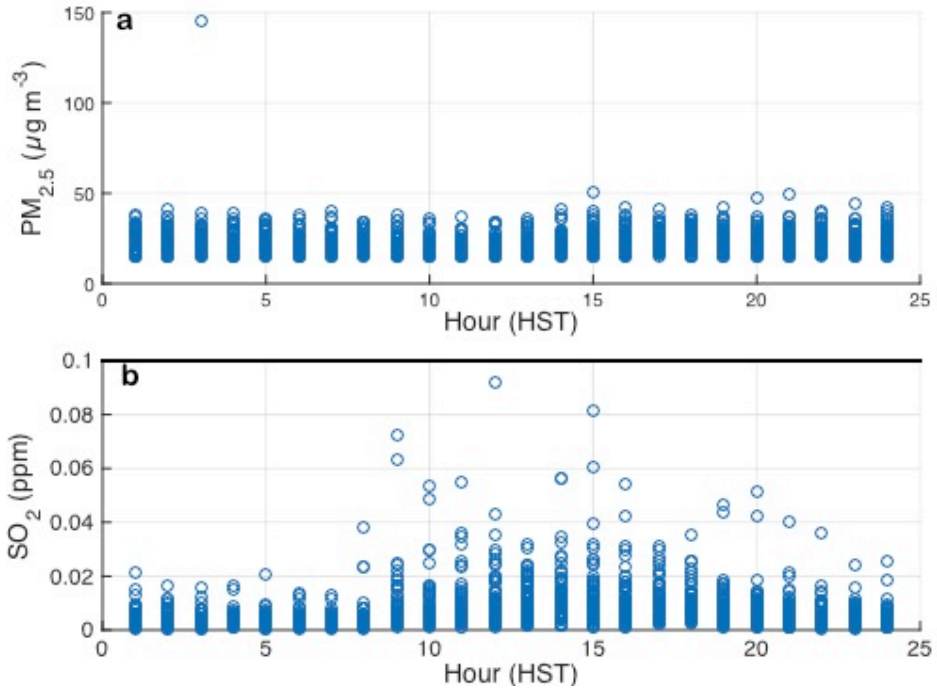

Figure A16: Scatterplot of $PM_{2.5}$ concentrations that exceed 15 µg/m³ vs. time of day (a) and corresponding SO_2 concentrations (b) at Kailua-Kona.

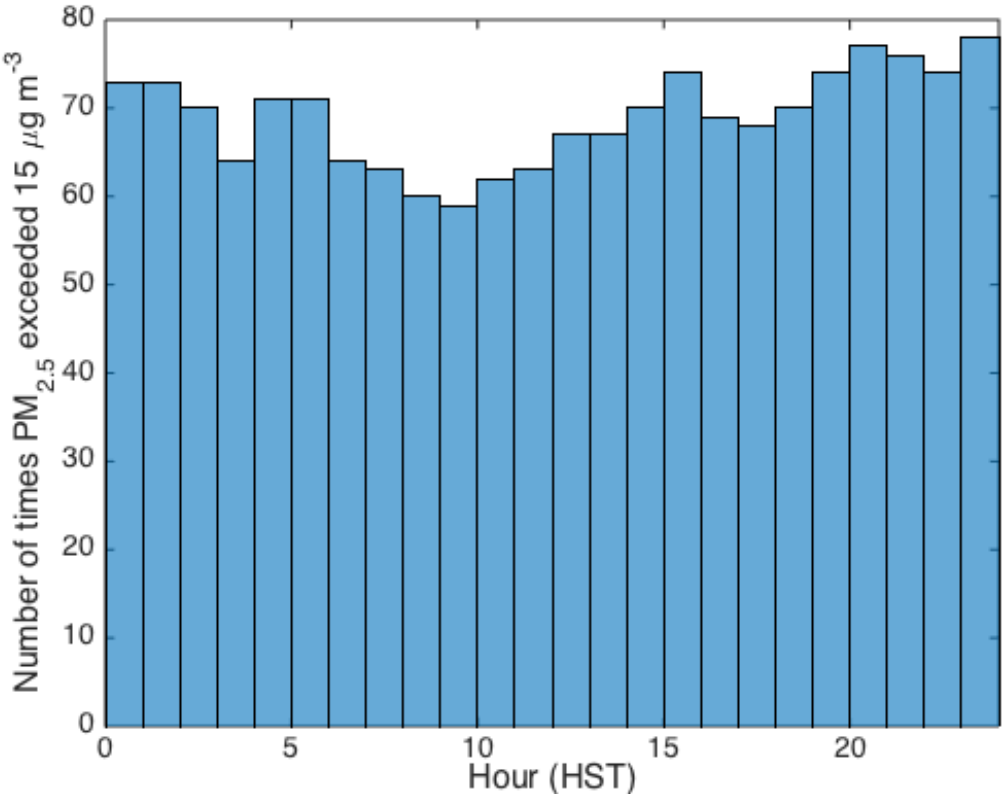

Figure A17: Hour during which $PM_{2.5}$ exceedances were observed at Kailua-Kona Feb-Apr 2012.

Inspection of wind directions during SO_2 exceedance events reveals evidence of an island/mountain circulation (Figure A18). Winds are predominantly onshore/offshore. This feature is just as strong in $PM_{2.5}$ data.

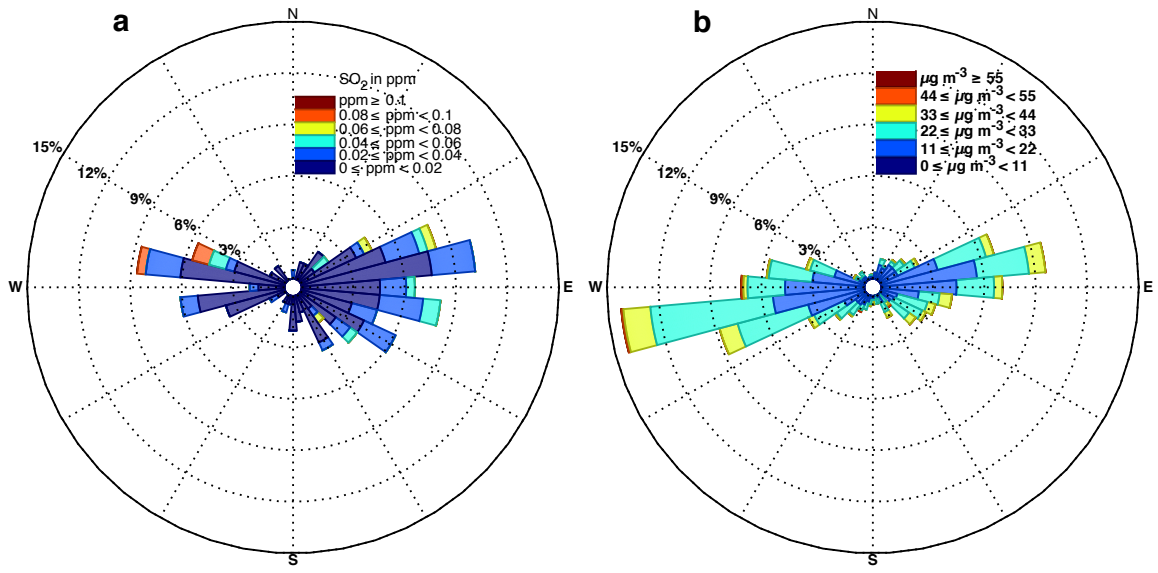

Figure A18: Wind Rose plots for (a) SO_2 and (b) $PM_{2.5}$ exceedance events at Kailua-Kona Feb-Apr 2012.

The impact of the diurnal island/mountain circulation on the air quality of Kailua-Kona is clear from this analysis. By the time volcanic emissions have propagated to the lee side of the island much of the SO_2 has been converted to sulfate aerosols ($PM_{2.5}$). All pollution episodes are the result of $PM_{2.5}$ and are carried onshore during the day and offshore at night by the island/mountain circulation.

In summary, this brief analysis indicates that local-scale island/mountain circulations primarily control the flow of pollutants downwind of Kīlauea volcano. These diurnally driven circulations transport volcanic emissions into communities during certain times of the day. Additionally, due to the impact of photolytic precursors involved in chemical conversion on sulfur dioxide to sulfate aerosols, high concentrations of SO_2 are found predominately at night at Pāhala and Ocean View.

REFERENCES

Alduchov, O. A. and R. E. Eskridge, 1996, Improved Magnus' form approximation of saturation vapor pressure. *J. Appl. Meteor.,* 35, 601-609.

Altshuller, A. P., 1982, Atmospheric concentrations and distributions of chemical substances. In the Acidic Deposition Phenomenon and it's Effects, US Environmental Protection Agency, Washington, DC

Atkinson, R., D. L. Baulch, R. A. Cox, R. F. Hampson Jr., J. A. Kerr, and J. Troe, 1989, Evaluated kinetic and photochemical data for atmospheric chemistry: Supplement III, *J. Phys. Chem. Ref. Data***, 18(2),** 881-1,097.

Barth, M. C., D. A. Hegg, P. V. Hobbs, J. G. Walega, G. L. Kok, B. G. Heikes, and A. L. Lazrus, 1989, Measurements of atmospheric gas-phase and aqueous-phase hydrogen peroxide concentrations in winter on the east coast of the United States, *Tellus*, **41B**, 61-69.

Baulch, D. L., R. A. Cox, R. F. Hampson, Jr., J. A. Kerr, J. Troe, and R. T. Watson, 1980, Evaluated Kinetic and Photochemical Data for Atmospheric Chemistry, *J. Phys. Chem. Ref. Data*, **9**, 295-471.

Beirle, S., C. Horman, M. Penning de Vries, S. Dorner, C. Kern, and T. Wagner, 2013, Estimating the volcanic emission rate and atmospheric lifetime of SO2 from space: A case study for Kilauea volcano, Hawai'i, *Atmos. Chem. Phys. Discuss.*, **13**, 28,695-28,727.

Boersma, K. F. and J. P. de Vroom, 2006, Validation of MODIS aerosol observations over the Netherlands with GLOBE student measurements, *J. Geophys. Res.*, **111**, D20311, doi:10.1029/2006JD007172

Brooks, D. R., and F. M. Mims III, 2001, Development of an inexpensive handheld LED-based Sun photometer for the GLOBE Program, *J. Geophys. Res.*, **106**, 4733–4740.

Businger, S., R. Huff, A. Pattantyus, R. Draxler, K. Horton, A. J. Sutton, and T. Elias, 2015, Observing and Forecasting Vog Dispersion from Kīlauea Volcano, Hawai'i , *Bull. Amer. Meteor. Soc.*, 96, 1667-1686, doi:http://dx.doi.org/10.1175/BAMS-D-14-00150.1

Caffrey, P., W. Hoppel, G. Frick, L. Pasternack, J. Fitzgerald, D. Hegg, S. Gao, R. Leaitch, N. Shantz, T. Albrechcinski, and J. Ambrusko, 2001, In-cloud oxidation of SO_2 by O_3 and H_2O_2: Cloud chamber measurements and modeling of particle growth, *J. Geophys. Res.*, **106**, D21, 27,587-27,601.

Calvert, C. A., B. G. Heikes, W. R. Stockwell, V. A. Mohnen, and J. A. Kerr, 1983, Some considerations of the important chemical processes in acid deposition, In: *Chemistry of Multiphase Atmospheric Systems*, K. Jaeschke (ed.), pp. 615-647.

Cantrell, W., G. Shaw, C. Leck, L. Granat, and H. Cachier (2000), Relationships between cloud condensation nuclei spectra and aerosol particles on a south-north transect of the Indian Ocean, *J. Geophys. Res.*, **105**, D12, 15,313-15,320.

Charles, L. A., S. Chaw, V. Vladutescu, Y. Wu, F. Moshary, B. Gross, S. D. Gedzelman, and S. Ahmed, 17 January 2007, Application of CCNY lidar and ceilometers to the study of aerosol transport and $PM_{2.5}$ monitoring, paper presented at Third Symposium on LIDAR Atmospheric Applications, American Meteorological Society, San Antonio, TX.

Charlson, R. J., S. E. Schwartz, J. M. Hales, R. D. Cess, J. A. Coakley, J. E. Hansen, and D. J. Hoffman, 1992, Climate forcing by anthropogenic aerosols, *Science*, **255**, 422-430.

Daum, P. H., R. J. Kelly, S. E. Schwartz, L/ Newman, 1984, Measurements of the chemical composition of stratiform clouds, *Atmos. Environ.,* **18**, 2,671-2,684.

Doukas, M. P., 2002, A new method from GPS-based wind speed determinations during airbourne volcanic plume measurements. U.S. Geol. Surv. Open-File Rep. 02-395.

Draxler, R. R., 2003, Evaluation of an Ensemble Dispersion Calculation, *J. App. Meteor.*, **42**, 308-317.

Draxler, R. R., and G. D. Hess, 1997: Description of the HYSPLIT_4 modeling system. NOAA Tech. Memo. ERL ARL-224, NOAA Air Resources Laboratory, Silver Spring, MD, 24 pp.

Draxler, R. R., and G. D. Hess, 1998: An overview of the HYSPLIT_4 modeling system of trajectories, dispersion, and deposition, *Aust. Meteor. Mag.*, **47**, 295-308.

Eatough, D. J., J. J. Christensen, N. L. Eatough, M. W. Hill, T. D. Major, N. F. Mangelson, M. E. Post, J. F. Ryder, L. D. Hansen, R. G. Meisenheimer, and J. W. Fischer, 1982, Sulfur chemistry in a copper smelter plume, *Atmos. Environ.*, **16**, 1,001-1,015.

Eatough, D. J., R. J. Arthur, N. L. Eatough, M. W. Hill, N. F. Mangelson, B. E. Richter, and L. D. Hansen, 1984, Rapid conversion of SO_2(g) to sulfate in a fog bank, *Environ. Sci. Technol.*, **18**, 855-859.

Eatough, D. J., F. M. Caka, and R. J. Farber (1994), The conversion of SO_2 to sulfate in the atmosphere, *Isreal J. of Chemistry,* **34**, 301-314.

Elias, T. and A. J. Sutton, 2007, Sulfur dioxide emission rates from Kīlauea Volcano, Hawai'i, an update: 2002-2006, U.S. Geol. Surv. Open-File Rep. 2007-1114.

Elias, T. and A. J. Sutton, 2012, Sulfur dioxide emission rates from Kīlauea Volcano, Hawai'i, 2007-2010, U.S. Geol. Surv. Open-File Rep. 2012-1107.

Environmental Integrity Project, 26 July 2007, Dirty Kilowatts: America's most polluting power plants, Environmental Integrity Project, Washington D.C.

ESPERE, 2006, ESPERE Climate Encyclopedia. Accessed 23 March 2016. [Available online at http://klimat.czn.uj.edu.pl/enid/Service/Encyclopaedia_4sl.html.]

Finlayson-Pitts, B. J. and J. N. Pitts, 1986, Atmospheric Chemistry: Fundamentals and Experimental techniques, Wiley, New York.

Forberich, O., T. Pfeiffer, M. Spiekermann, J. Walter, F. J. Comes, R. Grigonis, K. C. Clemitshaw, and R. A. Burgess, 1999, Measurement of the diurnal variation of the OH radical concentration and analysis of the data by modeling, *J. Atmos. Chem.*, **33**, 155-181.

Forrest, J., R. W. Garber, and L. Newman, 1981, Conversion rates in power plant plumes based on filter pack data: the coal-fired Cumberland Plant, *Atmos. Environ.*, **15**, 2,273-2,282.

Freitas, S. R., K. M. Longo, J. Trentmann, and D. Latham, 2010, Technical note: Sensitivity of 1-D smoke plume rise models to inclusion of environmental wind drag, *Atmos. Chem. Phys.*, **10**, 585-594, doi:www.atmos-chem-phys.net/10/585/2010/.

Gerlach, T. M., 2003, Elevation effects in volcano applications of the COSPEC. In: Oppenheimer, C., D. M. Pyle, and J. Barclay (eds.), *Volcanic Degassing*, Geological Society, London, Special Publications, **213**, 169-175.

Hand, J. L. and W. C. Malm, 2006, Review of the IMPROVE equation for estimating ambient light extinction coefficients, downloaded from http://vista.cira.colostate.edu/IMPROVE/.

Hand, J. L., B. A. Schichtel, W. C. Malm, and M. L. Pitchford, 2012, Particulate sulfate ion concentration and SO_2 emission trends in the United States from the early 1990s through 2010, *Atmos. Chem. Phys.,* **12**, 10,353-10,365, doi:10.5194/acp-12-10353-2012.

Hand, T. M., C. Y. Chan, A. A. Mehrabzadeh, W. H. Pan, and R. J. O'Brien, 1991, Diurnal cycle of tropospheric OH, *Nature*, **322**, 617-620.

Hawai'i Department of Health, 2013, Documentation for natural events excluded data Kona air monitoring station, AQS ID 15-001-1012 2011-2012 $PM_{2.5}$ exceedances, State of Hawai'i Department of Health Clean Air Branch, Honolulu, Hawai'i.

Hegg, D. A., 1989, the relative importance of major aqueous sulfate formation reactions in the atmosphere, *Atmos. Res.*, **22**, 323-333.

Hobbs, P. V., J. P. Tuell, D. A. Hegg, L. F. Radke, and M. W. Eltgroth, 1982, Particles and gases in the emissions from the 1980-1981 volcanic emissions of Mt. St. Helens, *J. Geophys. Res.*, **87**, 11062-11086.

Hoffman, M. R. and J. G. Calvert, 1985, Chemical transformation modules for Eulerian acid deposition models: Vol. II. The aqueous-phase chemistry, Acid Deposition Modeling Project, National Center for Atmospheric Research.

Holben, B. N., D. Tanre, A. Smirnov, T. F. Eck, I. Slutsker, N. Abuhassan, W. W. Newcomb, J. Schafer, B. Chatenet, F. Lavenue, Y. J. Kaufman, J. VandeCastle, A. Setzer, B. Markham, D. Clark, R. Frouin, R. Halthore, A. Karnieli, N. T. O'Neill, C. Pietras, R. T. Pinker, K. Voss, and G. Zibordi, 2001, An emerging ground-based aerosol climatology: Aerosol Optical Depth from AERONET, *J. Geophys. Res.,* **106(D11)**, 12,067-12,097.

Hollingshead, A., S. Businger, R. Draxler, J. Porter, and D. Stevens, 2003, Dispersion modeling of the Kilauea plume. *Bound.-Layer Meteor*., **108**, 121-144.

Horton, K.A., G. Williams-Jones, H. Garbeil, T. Elias, A.J. Sutton, P. Mouginis-Mark, J.N. Porter, and S. Clegg, 2006, Real-time measurement of volcanic SO2 emissions: Validation of a new UV correlation spectrometer (FLYSPEC). *Bull. Volcanol.*, **68**: 323 – 327.

Hua, W., Z. M. Chen, C. Y. Jie, Y. Kondo, A. Hofzumahaus, N. Takegawa, C. C. Chang, K. D. Lu, Y. Miyazaki, K. Kita, H. L. Wang, Y. H. Zhang, and M. Hu, 2008, Atmospheric hydrogen peroxide and organic hydroperoxides during PRIDE-PRD'06, China: their concentrations, formation mechanism and contribution to secondary aerosols, *Atmos. Chem. Phys.*, **8**, 6755-6773.

Huang, A. A., R. J. Farber, R. L. Mahoney, D. J. Eatough, L. D. Hansen, and D. W. Allard, Chemistry of invisible power plant plumes in Southern California—The

airborne persepective,75th Annual Meeting of the Air Pollution Control Association, paper 82-24.5.

Huang, D. and Z. Chen, 2010, Reinvestigation of the Henry's law constant for hydrogen peroxide with temperature and acidity variation, *J. Environ. Sci.*, **22(4)**, 570-574.

Jones, A., D. L. Roberts, M. J. Woodage, and C. E. Johnson, 2001, Indirect sulphate aerosol forcing in a climate model with an interactive sulphur cycle, *J. Geophys. Res.*, **106**, 20,293-20,310.

Keene, W. C., R. Sander, A. A. P. Pszenny, R. Vogt, P. J. Crutzen, and J. N. Galloway, 1998, Aerosol pH in the marine boundary layer: a review and model evaluation, *J. Aerosol Sci.*, **29**, 339-356.

Kiehl, J. T. and B. P. Briegleb, 1993, The relative roles of sulfate aerosols and greenhouse gases in climate forcing, *Science*, **260**, 311-314.

Kroll, J. H., E. S. Cross, J. F. Hunter, S. Pai, L. M. M. Wallace, P. L. Croteau, J. T. Jayne, D. R. Worsnop, C. L. Heald, J. G. Murphy, and S. L. Frankel, 2015, Atmospheric Evolution of sulfur emissions from Kīlauea: Real-time measurements of oxidation, dilution, and neutralization within a volcanic plume, *Environ. Sci. Technol.*, **49**, 4129-4137, doi:10.1021/es506119x

Longo, B. M., 2013, Adverse Health Effects Associated with Increased Activity at Kilauea Volcano: A Repeated Population-Based Survey, ISRN Public Health, doi:10.1155/2013/475962.

Maass, F., H. Elias, and K. J. Wannowius, 1999, Kinetics of the oxidation of hydrogen sulfite by hydrogen peroxide in aqueous solution: Ionic strength effects and temperature dependence, *Atmos. Environ.*, **33**, 4,413-4,419.

Martin, L. R. and D. E. Damschen, 1981, Aqueous oxidation of sulfur-dioxide by hydrogen-peroxide at low pH, *Atmos. Environ.*, **15**, 1615-1621.

Martin, L. R. and M. W. Hill, 1987, The effect of ionic strength on the manganese catalyzed oxidation of sulfur(IV), *Atmos. Environ.*, **21**, 2267-2270.

Mather, T. A., M. L. I. Witt, D. M. Pyle, B. M. Quayle, A. Aiuppa, E. Bagnato, R. S. Martin, K. W. W. Sims, M. Edmonds, A. J. Sutton, and E. Elyinskaya, 2012, Halogens and trace metal emissions from the ongoing 2008 summit eruption of Kilauea volcano, Hawai'i, *Geochim. Cosmochim. Acta.*, **83**, 292-323

Mauldin, R. L., F. L. Eisele, C. A. Cantrell, E. Kosciuch, B. A. Ridley, and B. Lefer, 2001, Measurements of OH aboard the NASA P-3 during PEM-Tropics B, *J. Geophys. Res.*, **106**, 32,657-32,666.

McGonigle, A. J. S., P. Delmelle, C. Oppenheimer, V. I. Tsanev, T. Delfosse, G. Williams-Jones, K. Horton, and T. A. Mather, 2004, SO_2 depletion in tropospheric volcanic plumes, *Geophys. Res. Lett.*, **31**, L13201, doi:10.1029/2004GL019990.

Miller, J. M. and A. M. Yoshinaga, 1981, The pH of Hawaiian precipitation a preliminary report, *Geophys. Res. Lett.*, **8**, 779-782.

Münkel, C., N. Eresmaa, J. Räsänen, and A. Karppinen, 2007, Retrieval of mixing height and dust concentration with lidar ceilometer. *Boundary Layer Meteorol.*, **124**, 117-128.

Nadau, P. A., 2006, A Multi-parameter investigation of volcanic plume behavior and resultant environmental impact at a persistently degassing volcano, Masaya, Nicaragua, M. S. thesis, Dep. of Earth Sciences, Simon Fraser Univ., Burnaby, British Columbia, Canada.

Newman, L., 1981, Atmospheric oxidation of sulphur dioxide: a review as viewed from power plant and smelter plume studies, *Atmos. Environ.* , **15**, 2,231-2,239.

Oppenheimer, C., P. Francis, and J. Stix, 1998, Depletion rates of sulfur dioxide in tropospheric volcanic plumes, *Geophy. Res. Lett.,* **25(14)**, 2,671-2,674.

Pattantyus, A., and S. Businger, 2014, On the interaction of Tropical Cyclone Flossie and emissions from Hawai'i's Kīlauea volcano, *Geophys. Res. Lett.*, **41**, 4,082–4,089, doi:10.1002/2014GL060033.

Pattantyus, A. K. and S. Businger, 2015. Ensemble Forecasting of Volcanic Emissions in Hawai'i. *Annals of Geophysics, [S.l.]*, **57**, ISSN 2037-416X. Available at: http://www.annalsofgeophysics.eu/index.php/annals/article/view/6607. doi:10.4401/ag-6607.

Pearson, A. and S. J. Weiss, 1979, Some trends in forecast skill at the National Severe Storms Forecast Center, *Bull. Amer. Meteor. Soc.*, **60**, 319-330.

Perry, K. D., T. A. Cahill, R. C. Schnell, and J. M. Harris, 1999, Long-range transport of anthropogenic aerosols to the National Oceanic and Atmospheric Administration baseline station at Mauna Loa Observatory, Hawai'i, *J. Geophys. Res.*, **104**, 18521- 18533.

Platt, U., 1994, Differential Optical Absorption Spectroscopy (DOAS). In: Sigrist, M.W. (Editor), Air Monitoring by Spectroscopic Techniques, Chemical Analysis Series, 127. Wiley, New York: 27-84.

Porter, J. N., K. A. Horton, P. J. Mouginis-Mark, B. Lienert, S. K. Sharma, and E. Lau, 2002, Sun photometer and lidar measurements of the plume from the Hawai'i Kīlauea Volcano Pu'u O'o vent: Aerosol flux and SO2 lifetime, *Geophys. Res. Lett.*, **29**, 16, 10.1029/2002GL014744.

Raes, F., A. Saltelli, and R. Van Dingenen, 1992, Modeling formation and growth of H_2SO_4-H_2O aerosols: Uncertainty analysis and experimental evaluation, *J. Aerosol Sci.*, **23**, 759-771.

Read, W. G., L. Froidevaux and J. W. Waters, 1993, Microwave Limb Sounder measurement of stratospheric SO_2 from the Mt. Pinatubo eruption, *Geophys. Res. Lett.*, **20**, 1299-1302.

Rodriquez, L. A., I. M. Watson, V. Hards, G. Ryan, M. Edmonds, C. Oppenheimer, and G. J. S. Bluth, 2005, SO_2 conversion rates at Soufriere Hills volcano, Montserrat, B. W. I., paper presented at 17th Caribbean Geological Conference, San Juan, Puerto Rico.

Rolph, G. D., R. R. Draxler, and R. G. de Pena, 1992, Modeling sulfur concentrations and depositions in the United States during ANATEX, *Atmos. Environ.*, **26**, 73-93.

Rolph, G. D., R. R. Draxler, and R. G. de Pena, 1993, The use of model-derived and observed precipitation in long-term sulfur concentration and deposition modeling, *Atmos. Environ.*, **27A**, 13, 2,017-2,037.

Sander, S. P., J. Abbatt, J. R. Barker, J. B. Burkholder, R. R. Friedl, D. M. Golden, R. E. Huie, C. E. Kolb, M. J. Kurylo, G. K. Moortgat, V. L. Orkin and P. H. Wine, 2011, Chemical Kinetics and Photochemical Data for Use in Atmospheric Studies, Evaluation No. 17, JPL Publication 10-6, Jet Propulsion Laboratory, Pasadena, 2011 http://jpldataeval.jpl.nasa.gov.

Seinfeld, J. H. and S. N. Pandis, 1998, *Atmospheric chemistry and physics: From air pollution to climate change*, John Wiley and Sons. Inc., New York.

Shaw, G. E., 1980, Transport of Asian Desert Aerosol to the Hawaiian Islands, *J. App. Meteotol.*, **19**, 1254-1259.

Siegel, B. Z., M. Nachbar-Hapai, and S. M. Siegel, 1990, The contribution of sulfate to rainfall pH around Kilauea Volcano, Hawai'i, *Water Air Soil Poll.*, **52**, 227-235.

Simpson, R. M. C., 2010, Mechanisms of sulfate production in the remote equatorial Pacific marine boundary layer, Master's Thesis, University of Hawai'i at Mānoa, Honolulu, Hawai'i.

Stoiber, R. E., L. L. Malinconico, and S. N. Williams, 1983, Use of the correlation spectrometer at volcanoes. In: Tazieff, H. and Sabroux, J.C. (Editors), Forecasting Volcanic Events. Elsevier, New York: 424-444.

Stull, R. B., 1988, An Introduction into Boundary Layer Meteorology. Kluwer Academic Publishers, Dordrecht, Netherlands, 670.

Twomey, S., 1977, Influence of pollution on the short-wave albedo of clouds, *J. Atmos. Sci.*, **34**, 1,149-1,152.

Van Valin, C. C., J. D. Ray, J. F. Boatman, and R. L. Gunter, 1987, Hydrogen peroxide in air during winter over the south-central United States, *Geophys. Res. Lett.*, **14**, 1146-1149.

Vogt, R., P. J. Crutzen and R. Sander, 1996, A mechanism for halogen release from sea-salt aerosol in the remote marine boundary layer, *Nature*, **383**, 327-330.

Warneck, P., 1999, The relative importance of various pathways for the oxidation of sulfur dioxide and nitrogen dioxide in sunlit continental clouds, *Phys. Chem. Chem. Phys.,* **1**, 5,471-5,483.

Williams-Jones, G., K. A. Horton, T. Elias, H. Garbeil, P. J. Mouginis-Mark, A. J. Sutton, and A. J. L. Harris, 2006, Accurately measuring volcanic plume velocity with multiple UV spectrometers, *Bull. Volcanol.*, **68**, 328-332.

Williams-Jones, G., J. Stix and C. Hickson, 2008, *The COSPEC Cookbook: Making SO_2 Measurements at Active Volcanoes*. IAVCEI, Methods in Volcanology, 1.

Yuan, T., L. A. Remer, and H. Yu, 2011a, Microphysical, macrophysical, and radiative signatures of volcanic aerosols in trade wind cumulus observed by the A-Train, *Atmos. Chem. Phys.*, **11**, 7119-7132, doi:10.5194/acp-11-7119-2011.

Yuan, T., L. A. Remer, K. E. Pickering, and H. Yu, 2011b, Observatinal evidence of aerosol enhancement of lightning activity and convective invigoration, *Geophys. Res. Lett.*, **38**, L04701, doi:10.1029/2010/GL046052.